#### Nonlinear Elasticity in Concrete Structures: Toward In-Situ Methods for Integrity Assessment

#### Dissertation

with the aim of achieving a doctoral degree
at the Faculty of Mathematics, Informatics and Natural Sciences

Department of Earth System Sciences

at University of Hamburg submitted

submitted by

Marco Antonio Dominguez Bureos Hamburg, 2025

Department of Earth Sciences	
Department of Earth Sciences	
Chair of the Subject Doctoral Committee	
Earth System Sciences:	Prof. Dr. Hermann Held
Dean of Faculty MIN:	Prof. DrIng. Norbert Ritter
Date of oral defense	11.09.2025

#### **Eidesstattliche Versicherung** | **Declaration on Oath**

I hereby declare and affirm that this doctoral dissertation is my own work and that I have not used any aids and sources other than those indicated.

If electronic resources based on generative artificial intelligence (gAI) were used in the course of writing this dissertation, I confirm that my own work was the main and value-adding contribution and that complete documentation of all resources used is available in accordance with good scientific practice. I am responsible for any erroneous or distorted content, incorrect references, violations of data protection and copyright law or plagiarism that may have been generated by the gAI.

Hamburg, 19.05.2025

Ort,den | City,date

Unterschrift | Signature\*

Sunte

This work is dedicat	ed to my family: you	ur support throug	ghout this process wa
This work is dedicat	invalu	able.	gnout this process wa

### Acknowledgements

This thesis would not have been possible without the guidance and support of several people. Firstly, I want to extend my heartfelt thanks to my advisors, Prof. Dr. Céline Hadzioannou, Dr. Christoph Sens-Schönfelder, and Dr. rer. nat. Ernst Niederleithinger, for sharing their time and knowledge with me; those are the most valuable treasures one can offer.

I am especially grateful to Aida, Sven, Manuel, Sergio and Anjali for contributing not only to my PhD but also to my personal growth.

Last but not least, my sincere thanks to the entire seismology working group of the UHH, the SPIN ITN community, and those who made this ITN possible.

#### **Abstract**

Decades of research on small-scale concrete specimens—such as cores and beams—have demonstrated that concrete, a highly heterogeneous material, exhibits elastic nonlinear effects, namely the stress- and time-dependence of its elastic properties. These nonlinear effects are highly sensitive to the presence of heterogeneities, even at the milli- or nanoscale. Prior studies have proposed leveraging these nonlinear elastic effects as a nondestructive testing method for detecting small-scale damage in concrete structures. However, formalizing such techniques for real-world applications requires transferring knowledge from controlled laboratory conditions to field settings. This research extends the study of nonlinear elastic effects to a full-scale concrete structure under field conditions. Specifically, it investigates the presence of classical and nonclassical nonlinear elastic behaviours—the acoustoelastic effect and Slow Dynamics, respectively—and their relationship with the relative integrity level of a concrete test bridge. Through an experiment conducted to measure vibrations across multiple frequency bands, this work demonstrates that soft microstructures—associated with varying levels of structural integrity—can be identified using nondestructive, wavefield-based measurement techniques. These findings contribute to the investigations for the development of in-situ methods for early-stage damage detection in existing and new concrete infrastructure.

## Contents

Li	st of I	Figures		i
Li	st of T	Гables		viii
Li	st of A	Abbrevi	ations	ix
1	Intr	oductio	on	1
	1.1	Evide	nce of Nonlinear Elasticity in Concrete	3
		1.1.1	Classical nonlinear elasticity in concrete	3
		1.1.2	Nonclassical nonlinear elasticity in concrete	$\epsilon$
2	Stre	ss- and	time-dependent variations of elastic properties for integrity as	<b>;-</b>
	sess	ment in	a reinforced concrete test bridge	9
	2.1	Introd	luction	10
	2.2	Exper	iment	12
		2.2.1	Stress Protocol	13
		2.2.2	Preprocessing and temperature corrections	14
	2.3	Theor	retical framework and Methods	15
		2.3.1	Linear Elasticity	15
		2.3.2	Classical Nonlinear Elasticity	15
		2.3.3	Nonclassical Nonlinear Elasticity	16
		2.3.4	The Coda Wave Interferometry	17
	2.4	Result	ts	18
		2.4.1	Observations on Linear elasticity	18
		2.4.2	Observations on Classical Nonlinear elasticity	18
		2.4.3	Observations on Nonclassical Nonlinear elasticity	19
	2.5	Discus	ssion	21
		2.5.1	P-wave velocity	21
		2.5.2	Acoustoelastic effect	21
		2.5.3	Velocity drops	22
		2.5.4	Cross-plots	24
	2.6	Concl	usion	26
3	Stre	ss-depe	ndent Slow Dynamics in concrete structure under field conditions	s 28
	3.1	Introd	luction	29
	3.2	Time-	dependent dv/v observations	30
		3.2.1	dv/v Measurements - The components	30
		3.2.2	Models for Slow Dynamics in complex solids	32
		3.2.3	The analytical model	35
	3.3	Data I	Inversion	37

Contents

		3.3.1	Prior information in data space	37
		3.3.2	Prior information in model space	37
		3.3.3	Solving the inverse problem	38
	3.4	Result		39
		3.4.1	The relationship between the analytical model parameters and	
			the observed data	39
		3.4.2	The analysis of $\alpha$ , the linear effect	42
		3.4.3	The analysis of $\beta$ , the velocity drops	44
		3.4.4	Time-dependent elastic and energy dissipation changes	45
	3.5	Discus	ssion	47
		3.5.1	Possible physical mechanisms for slow dynamics in concrete .	47
		3.5.2	Relationship between $\alpha$ and $\beta$ with structural effects	48
	3.6	Concl	usions	49
		_		
4			ns of Nonlinear Elasticity in a Concrete Structure using Standing	
	Wav			53
	4.1		uction	54
	4.2		Frequencies of the bridge	55
	4.3	•	sis of stress-dependent dv/v changes of standing waves	56
		4.3.1	Calculation of ACF	56
		4.3.2	Stress-dependent dv/v calculation	58
		4.3.3	The stress-dependent elastic behaviour of standing waves	60
		4.3.4	Discussion on the velocity changes of the fundamental vibration	. 1
	4.4	A 1	mode	61
	4.4		sis of stress-dependent coda wave decay	64
		4.4.1	The Coda Q model and estimation for a concrete structure	64
	4.5	4.4.2	Discussion on the Coda Q analysis	65
	4.5	Conci	usions	67
5	Con	clusion	s and outlook	70
	5.1	Concl	usions	70
	5.2		bk	71
Αŗ	pend	ices		
Α	Add	itional l	Material	75
	A.1		es of the experiment	75
	A.2		pilistic inversion processes	78
	A.3		Q as a function of frequency	82
D.	eferen			83
ĸe	ueren	ces		_ X 1

## List of Figures

2.1	Upper panel: the BLEIB reference structure. Mid panel: a schematic representation of the BLEIB structure, the prestressing system, and the geometry of the sensor arrays; the linear array of six-component sensors (black boxes) adjacent to the linear array of one-component geophones (blue inverted cones) used during the experiment are also shown. Lower panel: a zoom in view on the spans of the bridge where the four pairs of ultrasound transducers are embedded (dark green, light green, dark brown, and light brown); the straight line represents the source-receiver straight ray path; the blue arrow shows the place where the weight-drop source was activated to induce softening on the concrete	12
2.2	a): The variations of stress followed during the experiment with respect to time; the recording time slots on the Northside (light green line segments) and Southside (light brown line segments); the inverted triangles denote the activation instances of the impulsive source on the Northside while the diamonds represent those on the Southside. b) An inset to the stress protocol that shows one Ultrasound Pulse every five seconds was recorded during the experiment. c) The features of the recorded Ultrasound Pulses. d) Inset to the time window used to estimate the Ultrasound Pulse Velocity (TPW) and the portion of the pulse used to estimate concrete's nonlinear classical effects (P-S wave), and e) the nonclassical nonlinear effects (Early coda wave)	14
2.3	Observations of linear elasticity. The estimated ultrasound pulse velocity at every location on the bridge	18
2.4	Observation of classical nonlinear elasticity. From a) to d) plots of the relative velocity changes as a function of the applied compressive forces for the four locations (D and C in the x-axis stand for Decompressive and Compressive stages); dots indicate velocity changes during decompression, and the solid black line the linear model that fits the estimations; similarly, crosses and the dashed black line represent velocity changes and the corresponding linear model during compression. e) Plots the slope of each linear model; dots indicate the slopes of measurements while decompressing, and crosses indicate the slopes of measurements while compressing. The slope is referred to as the Acoustoelastic Effect.	19

List of Figures iii

2.5	Observations on nonclassical nonlinear elasticity. a) The relative velocity changes as a function of the time in the four locations (the effect of the vertical impulsive sources) and the cross-correlation coefficient (CCC) obtained with the stretching method; the vertical dashed lines show the reference measurements for the stretching. b) Inset to show the baseline phase (triangles) and the effect of the three impulsive sources (the three blue curves). The red line shows the linear effect that shifts and deforms the three relaxation processes through time. c) The superimposed relaxation processes after the matching curve analysis. The vertical blue line marks the second $15 \pm 5$ seconds to estimate the relative velocity drop. d) The slope of the linear effects observed at every compressive level on the four locations of the bridge. e) The relative velocity drop at $15 \pm 5$ seconds, measured at each level of compressive force on the four locations of the bridge.	20
2.6	The cooperative description of the bridge. a) The Linear, Classical Nonlinear, and Nonclassical Nonlinear elastic behaviours on the 3-D plot. b) The P-wave velocity, d) the acoustoelastic effect, and g) the Minimum and Maximum velocity drops measured at the four locations on the bridge. c) The cross-plot P-wave velocity vs Acouestoelastic effect. e) The cross-plot P-wave velocity vs Velocity drops. f) The cross-plot Velocity drops vs Acoustoelastic effect.	26
2.7	The conceptual model of the bridge: a) The stress-dependent relative velocity changes: 1) Preexisting tensile microstructures, in red, 2) 3)soften the bridge as the compressive force decreases and strengthen it as the compressive force increases. b) The time-dependent relative velocity changes: 1) In yellow, preexisting transient microstructures in a steady state produce no relative velocity changes. 2) transient microstructures are excited by the action of the vertical impulsive sources, and the bridge softens, and 3) the recovery process when the transient microstructures tend to return to 1) on logarithmic time scales	27
3.1	Datasets recorded at the four locations of the bridge at eight different compressive force levels. a) Plots of the eight datasets recorded on the south-left side. This side is categorised as concrete with a relatively high integrity level due to the high ultrasound pulse velocity values. b) Plots of the eight datasets recorded on the south-right side (a side with a relatively high integrity level). c) Plots of the eight datasets recorded on the north-left side. This side is categorised as concrete with a relatively low integrity level due to the low ultrasound pulse velocity values. d) Plots of the eight datasets recorded on the north-right side (a side with a relatively low integrity level)	31
3.2	Representation of the components present on each of the time-dependent dv/v datasets. a) the dv/v dataset recorded at a compressive force level of 280kN, with the times when the VISs were activated (VIS 1, VIS 2, and VIS 3) b) the elements that compose the dataset. The linear component, the three relaxation processes, and the remaining effects of the first and second VISs	32

List of Figures iv

3.3	An example of the data inversion process. a) Results of the data inversion for the dataset recorded at 280 kN in the south-right side. b) The histogram of the accepted proposals for the linear effect, c) the amplitude of the three relaxation processes, c) the 1st impact's remaining effect that acts on the second relaxation process, and d) the 2nd impact's remaining effect that acts on the third relaxation process	40
3.4	The acceptance rate estimated on the data inversion processes for north-left, north-right, south-left, and south-right datasets	41
3.5	The performance of the analytical model on reproducing consecutive slow dynamics effects at different compressive force levels, $dv/v(t,\sigma)$ , on concrete of different integrity levels. a) The observed dvv/v on the south-left side plotted in light brown, and the model is in a continuous dark blue line. b) The observed dvv/v on the south-right side plotted in dark brown, and the model is in a continuous dark blue line. c) The observed dvv/v on the north-left side plotted in light green, and the model is in a continuous dark blue line. d) The observed dvv/v on the north-right side is plotted in dark green, and the model is in a continuous dark blue line	42
3.6	The force rate and the estimated model parameters result from the data inversion process. a) The estimated compressive force rate (static changes) during the experiment. b) The linear effects, $\alpha$ values. c) The maximum amplitude of transients (velocity drop), $\beta$ values. d) the 1st impact's remaining effect, $\gamma$ values, acting on the second relaxation process. e) the 2nd impact's remaining effect, $\delta$ values, acting on the third relaxation process	43
3.7	Dv/v and Normalised Energy (N.E.) content datasets for concrete with the a) highest and b) lowest integrity levels.	46
3.8	Comparison of the three consecutive relaxation processes recorded with dv/v and normalised energy content on concrete of different integrity levels at a compressive force of 280 kN	47
3.9	The time-window-dependent behavior of the creep-like effect recorded after the change in the compressive force levels. A) I. Short time window, II. The sensitivity of the waves dominantly on the beam's compression volume, and III. The compressive-creep-like effect observed with the dv/v estimations for the North-Left and Right sides. B) I. A widened time window, II. The sensitivity of the waves mostly on the beam's compression volume and slightly on the beams' tension volume, and III. The creep-like effect observed with the dv/v estimations for the North-Left and Right sides. C) I. The early coda time window, II. The sensitivity of the waves all around the vicinity of the ultrasound transducers, and III. The creep-like effect observed with the dv/v estimations for the North-Left and Right sides	49

List of Figures v

3.10	Schematic representation of deflection changes on the bridge during the experiment and their effect on the Slow dynamic processes. Deflections tend to change the tension and compression volumes on the horizontal beam (see the red line neutral axis along the beam as a reference), causing different creep-like behaviour at every compressive force change, where the three slow dynamics processes are superimposed. This figure shows different deflection scenarios for the north and south spans and their possible effect on the second phase of creep related to the linear effect: I) at the beginning of the experiment, II) when the structure is undergoing decompression, III) at the lowest compressive force level and IV) when the structure is undergoing compression	50
4.1	Eigenfrequency analysis of the bridge with data recorded during the day (upper panel) and night (lower panel) with four translational sensors distributed along the bridge. Both analyses show the fundamental frequency of the bridge at 3.76 Hz, and three higher harmonics. Results were obtained in the frame of the GIOTTO project [Submitted by Dhabu et al., 2024].	55
4.2	The data employed to calculate the autocorrelation functions. a) plots the raw data recorded at the Geophone 1 (G01) when the structure was compressed at the initial compressive force level for this experiment (400 kN), which is the reference state. b) plots the raw data recorded with the same sensor when the structure was compressed at the second compressive force level for this experiment (370 kN), which is the first deformed state. The vertical colour bands represent the one-minute time windows used to calculate the autocorrelation function for the c) reference state, and the d) first deformed state	57
4.3	Cross-correlation functions and epsilon values as a function of the time window length. a) plots the cross-correlation values obtained after the stretching process of the reference and deformed autocorrelation functions, and b) the $\epsilon$ values that maximise the cross-correlation between the reference and deformed states, as a function of the time window langeth.	EO
4.4	length	58 59
4.5	The relative velocity changes at a central frequency of 3.76 Hz as a function of stress (the compressive force level), obtained with the Geophone 01. The dots indicate dv/v values estimated while the structure was decompressed, and crosses indicate dv/v values while the structure was compressed. The continuous line represents the linear model that fits the dv/v measurements at decompression, and the dashed line is the linear model that fits the dv/v measurements at compression	60

List of Figures vi

4.6	Stress-dependent relative velocity changes estimated at a central frequency of 3.76 Hz at all twelve geophones placed along the bridge. The Z-axis represents the relative velocity changes (dv/v), the X-axis represents the compressive force level (400 kN as a Reference state, and the subsequent seven deformed states at Decompression and Compression), and the Y-axis represents the geophone number (from G 01 to G 12 corresponding to the twelve inverted blue cones placed on the surface of the bridge). Dots correspond to dv/v estimations during decompression, and crosses correspond to estimations during compression. Vertical red bars indicate the error on the dv/v measurements	61
4.7	The acoustoelastic effect during decompression and compression of the fundamental standing wave of the bridge at a central frequency of 3.76 Hz, measured at all twelve geophones placed along the bridge. The vertical axis shows the slope of the linear relationship, dv/v, and stress level, also referred to as the acoustoelastic effect (AEE). Values for decompression are plotted with dots, and values for compression with crosses. The lower part of the figure shows the bridge and sensor locations (the twelve inverted blue cones placed on the surface of the bridge), illustrating the spatial distribution of the estimated AEE	62
4.8	Variation of PSD with respect to frequency measured with the vertical component of the IMU50 sensor	64
4.9	Procedure to estimate the quality factor Q using the six vertical impulsive sources (VISs) recorded at the geophone 01 when the structure was compressed with 400 kN. a) plots the raw data and the six VISs highlighted in green. Panels from b) to g) plot the VISs filtered around the central frequency $f$ of 3.76 Hz, and their corresponding approximation for $Q$ according to equation 4.8, which is the slope of the linear regression (in red) using the absolute value of the signal amplitude $A$ for a constant $f$ .	66
4.10	The frequency-dependency of coda Q estimated at station G 01 at a compressive force level of 400 kN. On the vertical axis, the estimated Q values are shown for nine different central frequencies indicated on the horizontal axis. Each central frequency plots the set of four values, which correspond to the six VISs, removing the outliers (maximum and minimum Q values)	67
4.11	Stress-dependent quality factor (Q) estimated at a central frequency of 3.76 Hz at all twelve geophones placed along the bridge. The Z-axis represents the Q (the dimensionless inversely proportional quantity to attenuation), the X-axis represents the compressive force level (400 kN as a Reference state, and the subsequent seven deformed states at Decompression and Compression), and the Y-axis represents the geophone number (from G 01 to G 12 corresponding to the twelve inverted blue cones placed on the surface of the bridge). Dots correspond to Q estimations during decompression, and crosses correspond to estimations during compression	68

List of Figures vii

4.12	The average quality factor (Q) estimated at a central frequency of 3.76 Hz at all twelve geophones placed along the bridge. a) Quality factors estimated at the beginning of the experiment at a compressive force level of 400 kN (the highest level), and b) at a compressive force level of	
	280 kN (the lowest level)	69
A.1	The BLEIB structure	75
A.2	The placement of the seismic equipment	76
A.3	The equipment used in the experiment	76
A.4	The prestressing system of the BLEIB structure (by Nicklas Epple)	77
A.5	The triggering of the Vertical Impulsive Source on the North span bridge	
	(by BAM)	77
A.6	Histograms of the data inversion process for the North left side (from	
	400 kN Decompression to 310 kN Compression)	78
A.7	Histograms of the data inversion process for the North left side (from	
	280 kN Decompression to 400 kN Compression)	79
A.8	Histograms of the data inversion process for the South left side (from	
	400 kN Decompression to 310 kN Compression)	80
A.9	Histograms of the data inversion process for the South left side (from	
	280 kN Decompression to 400 kN Compression)	81
A 10	Coda O analysis at Geophone 01	82

## List of Tables

1.1	Wavefield-based standard methods, capabilities, limitations and national and international norms.	2
3.1	Initial proposals and step lengths used in the MCMC Metropolis-Hastings	39

#### List of Abbreviations

CWI . . . . . . . Coda Wave interferometry.

LE . . . . . . Linear Elasticity.

CNE . . . . . . . Classical Nonlinear Elasticity.

NNE . . . . . . . Nonclassical Nonlinear Elasticity.

AEE . . . . . . Acoustoelastic Effect.

VIS . . . . . . . Vertical Impulsive Source.

SD . . . . . Slow Dynamics.

 $dv/v \ \ \ldots \ \ \ldots \ \$  Relative velocity changes.

NE . . . . . . . Normalised Energy content.

**DEP** . . . . . . Dynamic Elastic Property

To emphasise the importance of concrete in the increasing demand for infrastructure, it is opportune to mention that there are no precise numbers on how many concrete-made civil facilities there are worldwide due to the vast range of structures and variations in reports across countries. The easy production, relatively low cost, and mechanical performance of concrete justify the increase in cement demand, which also means an increment in the ambiguous number of concrete-made constructions. Assessing the durability and degradation of new, ageing and deteriorating concrete infrastructure is crucial from different perspectives. From an environmental perspective, concrete production results in CO2 emissions and requires energy consumption and water withdrawals. Those factors highlight the need to increase the sustainability of concrete, an idea widely accepted (Miller et al., 2018). From a social perspective, it is essential to assess the longevity and integrity of buildings so that they can withstand the impact of natural disasters such as earthquakes and reduce the astonishing number of human causalities from building collapses (Wyss et al., 2023).

To assure the safety, durability, and integrity of such concrete constructions, a set of techniques based on measuring different material properties has been and is still being developed. The target of those methodologies is to provide more accurate insights about the physical state of construction materials with a low—or null-destructiveness level, and consequently, these set of methods are referred to as Nondestructive Testing Techniques (NDT).

NDT practitioners are particularly interested in Dynamic Elastic Properties (DEP) of materials since these properties evaluate relevant features like compressive, tensile, and flexural strength. Broadly speaking, DEPs are estimated by inducing mechanical or electromagnetic waves of diverse frequency bands with significantly low-stress amplitude to the material and analysing how this induced wavefield is deformed after propagating.

There is a continuum of wavefield-based methods that serve to analyse concretewave interaction to harvest information about structures in the form of DEP for measuring specific factors such as residual strength, durability, and reliability of structural materials, as well as assemblies and systems in existing structures. Still, it is opportune to mention that despite being developed methodologically following scientific rigour,

N.D.T.	Parameter	Application	Limitation	Code
Schmidt Rebound Hammer test	Surface hardness Compressive strength Uniformity of concrete	To estimate strength and assess uniformity of concrete to assure quality.  To estimate early edge strength rate of strength gain for construction scheduling.	Surface condition affect results significantly. Measures limited depth (20-30 mm). Not suitable for concrete strength beyond 60 MPa and lightweight concrete with density less than 1440 kg/m3. Difficulty to assess internal flaws.	ASTM C805/C805M; BS EN 13791:2019; BS 1881-202: 1986; ASTM D5873-14
Ultrasonic Pulse Velocity (UPV)	Uniformity and density Compressive strength Depth of surface-breaking cracks	Evaluate quality and uniformity. Detect internal flaws. To predict concrete strength. Detection of damage in concrete and to monitor structural health.	Surface condition affect results significantly. Moisture condition affect greatly. For accuracy access to both sides of structures is often required. Difficult to detect fine cracks. Material heterogeneity can cause fluctuations in consistent reading. They are less effective detecting defects beyond 50 cm in concrete.	ASTM C597-97; BS 1881-203: 1986; BS 4408-5:1974; BS EN 12504-4: 2021; ISO/DIS 8047
Ground Penetrating Radar (GPR)	Thickness measurement. Void and crack detection. Depth and position of rebar.	Determine rebar formation and corrosion mapping within concrete structures. Describing the thickness of concrete slabs and walls to ensure design specification. Detect concrete deterioration and delamination.	Resolution trade-off at dense materials making difficult to detect internals.  In heavily reinforced concrete closely spaced bar (less than 7cm) create signal clutter highly.  Surface condition (uneven or coating) can affect results.  Moisture content in concrete can affect accuracy of GPR.	ASTM D6087-08; ASTM D6432-11; BS EN 302 066 V2.2.1
Acoustic Emission	Nature and Level of damage. Damage mechanism. Location of damage.	To detect and locate damage. Corrosion monitoring in RC. To control quality of concrete. Continuously to monitor structures.	It requires good surface access to place sensor (rough surface hinder success). Environmental interference reduce reliability of test by up to 20-30%.  AE testing is more effective at detecting active defects that are growing.  Limited to detection range from sensor.	ASTM E2983-14:2019; ASTM E3100-17; ISO 16836:2019
Impact-echo test	Thickness. Internal defects. Characteristic of defect. Mechanical properties.	To assess delamination and voids. To measure thickness and depth. To detect and assessing the depth and extent of cracks. To assess mechanical properties of concrete.	Effective for limited depth (1 m) in concrete. Surface condition can lead to poor signal. Material heterogeneity within the concrete structure can scatter waves. Environmental noise and operational vibration can interface IE signals.	ASTM C1383-23; ACI 228.2R
Vibration-based methods	Natural frequencies. Mode shapes. Damping ratio. Modal strain energy.	To detect damage and dynamic property for structural health monitoring. To assess the seismic performance of structure.	Environmental sensitivity (traffic, wind and machinery) affected significantly.  Not more effective in detecting localised damage. Requires accurate baseline measurements of the structures vibration characteristics.  Temperature affects slightly results.	ASTM C215-19; BS 1881-209:1990

**Table 1.1:** Wavefield-based standard methods, capabilities, limitations and national and international norms.

just a few methods are regularly evaluated, expanded, and improved, which are called *standardised techniques*. Standards serve as comprehensive guidelines for identifying flaws in materials and objects without causing damage, indicating recommended equipment, test numbers, and evaluation and computation procedures. Wavefield-based standard methods, capabilities, and corresponding international standard codes are listed in Table 1.1, based on (Tefera and Tarekegn, 2025).

Standardised wavefield-based methods demonstrate, on average, a good performance in estimating compressive strength, detecting internal flaws and rebar details in reinforced concrete, and assessing the dynamic response of buildings at the structural level, referring specifically to the vibration-based methods. This performance is based on DEP values representative of the instant when the evaluation is carried out (instantaneous DEP). On that note, two main observations are pointed out.

1. The way instantaneous DEP are measured considers no deformations in buildings: Traditionally, concrete's DEP have been quantified under the assumption that the deformations caused to the concrete specimen due to any external perturbation are small enough to be ignored (deformations do not cause any significant change to the physical properties of concrete, i.e. the elastic moduli). However, this assumption is arguable, given that constructions experience the effects of external solicitation at different magnitudes (ranging from operational activities to an earthquake occurrence) lasting for different time lapses. This dynamic nature of the surrounding environment of concrete structures challenges the traditional approaches to quantifying DEP. Overestimating or underestimating instantaneous DEP measurements by large-deformation effects is a possibility. A plausible way to address this challenge is using a different physical/mathematical framework that considers the deformations the structures are subjected to by modifying how stress relates to strain for concrete.

2. The current standards excel in damage identification but seem to be blind to assessing the susceptibility of a healthy concrete member to cracking. Material failure is not instantaneous but rather results from the process of stress transfer through internal deformation. This transfer progressively localises deformation on developing fractures and fault structures, concentrating the stress on asperities until shear stress finally exceeds material strength (Cartwright-Taylor et al., 2022). Depending on the stage of this process, stress transfer can be observed through changes in stiffness, macroscopic deformation, or acoustic emissions (Asnar et al., 2025). In heterogeneous materials like rocks, concrete, or cracked materials, this process is governed by some notable nonlinear stress- and time-dependent mechanical properties. The instantaneous DEP tend to change considerably, and the nature of this evolutive process is intimately related to micro/nano-scale processes in the material.

The two statements posed before, that is, questions about the effect of external perturbations on concrete's DEP and the analysis of physical processes prior to material failure using wavefields, seem different, but they are interwoven in their backbones. Seeking clues or signs of previous stages of concrete failure through systematic analysis of stress-and time-dependent elastic properties promotes early-stage-damage identification in concrete while accounting for the effect of deformations in the concrete member.

#### 1.1 Evidence of Nonlinear Elasticity in Concrete

Aside from the usefulness of instantaneous elastic constants estimated with the above-mentioned methods, a distinctive elastic behaviour in complex materials like rocks, cracked bodies, and concrete was observed decades ago under controlled experiments. This elastic behaviour, notably sensitive to the overall heterogeneity level of the material, refers to the evolutive feature of DEP and is dominantly triggered when the solid is perturbed at relatively low strain levels, i.e.  $10^{-7} < \epsilon < 10^{-3}$  (Guyer and Johnson, 2009). It promotes a material's description, not only in terms of its instantaneous elastic moduli but also higher-order constants or phenomenological variables that react to interactions at micro/nano structural scales, this, by modifying the material's stress-strain relationship.

This exceptional elastic behaviour of complex solids is constituted by a classical and a nonclassical component to certain degrees. The scientific community refers to it as the Nonlinear elasticity of solids, and there is ongoing work to leverage it in the context of damage assessment of construction materials.

#### 1.1.1 Classical nonlinear elasticity in concrete

The classical component of nonlinear elasticity refers to the evolution of elastic wave speeds as the stress state of the material changes (Pao and Gamer, 1985). Early experiments on the effect of changes in the rigidity of solids as a function of pressure were inspired by the idea of analysing the impact of hydrostatic pressure on the elastic behaviour of rocks using dynamic methods (Birch and Bancroft, 1938). As the theoretical framework that describes such effects was formulated (F D Murnaghan, 1937), this phenomenon became salient for diverse engineering materials like concrete; the reason

was the seeming influence of pores and compressible microstructures, which results in an overall structural looseness improved by changes in the confining forces and observes nonlinear elastic relationship.

The analysis of concrete started with investigating the feasibility of vibrating a concrete cylinder under longitudinal stress (compressive forces) with simply supported (hinged-ends) mode vibration (Obert, 1939). Later, using a similar approach, Linger, 1963 (Linger, 1963) reported that the modulus of elasticity of concrete tends to increase as the stress increases for static and dynamic experiments, provided the inelastic creep can be eliminated. That suggests concrete behaves like an elastoplastic material rather than a perfectly elastic one.

The standard UPV method (table 1.1) was used as an alternative to estimate concrete's DEP and investigate the influence of micro-imperfections in the stress-dependent behaviour of high-performance concrete (Raju, 1970) and concrete samples of mixes at different proportions (Suaris and Fernando, 1987) subjected to uniaxial static and repeated loads to study crack initiation and growth rate. Based on Murnaghan's work (F D Murnaghan, 1937) on nonlinear elasticity in isotropic solids, Hughes and Kelly (D S Hughes and J L Kelly, 1953) derived analytical expressions relating stress and wave velocities for isotropic media under hydrostatic pressure; such derivations were condensed in the so-called Acoustoelastic Theory. This classical signature of nonlinear elastic behaviour was observed in concrete cylinders under uniaxial compression using both P—and S-waves (compressive and shear waves) at ultrasound frequencies. Findings showed differences in velocity waves while loading and unloading, suggesting the presence of subtle hysteretic behaviour due to mechanical stress, as well as the sensitiveness of wave polarisation to the loading direction (Jean-François Chaix et al., 2008). Even though observed a century ago, this stress-dependent sensitivity of dynamic elastic constants was largely dismissed due to two main factors: I) the complex process of measuring them even in lab conditions, and II) the simplicity of linear elasticity theory that governs the instantaneous DEP. Contributions to this research line came by using different phases of mechanical waves to study this classical component of the nonlinear elastic behaviour in concrete. Investigations on the usefulness of the late part of the wave recordings (known as coda) to sense changes in field-condition concrete structures started with the demonstration of the presence of multiple scattered waves in the coda as a result of the dynamic response of concrete structures (concrete slab) and their sensitivity to thermal changes (Eric Larose et al., 2006).

By analysing the anisotropy of wave velocities depending on the material's compressive forces and directions, the acoustoelastic theory allows for determining high-order elastic constants in materials. Measurements of relative wave velocity changes in small concrete samples at different stress conditions were conducted using the scattered features of the late part of ultrasound recordings via the Coda Wave Interferometry (CWI) technique (Cedric Payan et al., 2008) proposing the first documented third-order elastic constants for concrete (Payan et al., 2009).

The capabilities of CWI in terms of resolution are analysed tracking the effect of weak stress changes on the acoustic diffuse coda; relative velocity changes in the order of  $2x10^{-5}$  on a concrete sample were estimated as a result of stress variations on the order of tens of kPa (50 kPa), suggesting that as the nonlinear parameter strongly depends on the micro-damage of the concrete, CWI would form an efficient and nondestructive way to probe the integrity of civil engineering structures (Eric and Stephen, 2009).

Studies on the stress-dependent elastic behaviour on concrete were complemented by the use of surface waves in the sonic regime and acoustic emission measurements to monitor microcracking activities in a concrete sample under stress-induced damage, finding that surface wave velocities are fewer times more sensitive to the level of stress and damage in concrete than ultrasonic body waves (Shokouhi et al., 2010). This approach has proven to be a practical alternative to performing measurements in concrete structures with only one-sided access.

Previous laboratory experiments on diffuse waves in concrete have advanced CWI, positioning it as a recognised method among nondestructive testing techniques for monitoring wave velocity changes in a strongly heterogeneous medium. For instance, damage induced by thermal shock was analysed together with mechanical cyclic loading (Schurr et al., 2011) and effects of uniaxial tensile forces through a thermally-compensated CWI contributed to deepening the insights on distinguishing reversible velocity variations due to elastic deformation from irreversible ones caused by microcracking (Yuxiang Zhang et al., 2012). Alternatives to the CWI based on the estimation of the magnitude square coherence, like the Coda Wave Comparison technique (CWC), are suggested to monitor stress changes in concrete cylinders; the entire waveform recorded at relatively low sampling frequencies can be used in the analysis (Hafiz and Schumacher, 2018).

Concrete samples of different ultimate strengths (high- and ultra-high-performance concrete) were subjected to uniaxial compressive loadings to measure velocity variations and their third-order elastic constants, showing that ultra-high-performance concrete undergoes more minor velocity variations (up to 20 times smaller) than high-performance concrete and smaller values of third-order elastic constants. These observations suggest an influence of bonding improvers on the nonlinear behaviour of concrete (Ankay and Zhang, 2019).

The wide variety of tested concrete samples and the reliability of CWI to sense weak changes in their microstructure, together with the memory effect of the material to the maximum experienced stress (known as the Kaiser effect (Lavrov, 2003)), lead to the incorporation of the acoustoelastic effect of different concrete types and loading ranges to a concrete database (Zhan et al., 2020).

Analysis of the time-window effects in coda wave interferometry was conducted to evaluate variations on the acoustoelastic constant, concluding that the acoustoelastic effect is most significant when the propagation and particle displacement are parallel to the stress direction and suggesting the Direct P-Wave Interferometry method (DPWI), where the chosen time window is dominated by the early part of the USP (P-wave) (Zhong et al., 2021).

Studies on concrete's response to tension and compression were complemented with the analysis of time-dependent effects like creep and shrinkage with the CWI, proposing a set of curves to calibrate in-situ measurements of relative velocity variations (Diewald et al., 2022).

In laboratory experiments, it was solidly demonstrated that the classical second-order, two-parameter-based linear elastic analysis (instantaneous DEP) of cement-based materials does not suffice to evaluate stress-strain behaviour in compression/tension. Higher-order formulations based on third-order parameters are, therefore, necessary to correctly evaluate concrete responses to applied stresses (Nogueira and Rens, 2019) and the sensitivity of those parameters to variations in the concrete's microstructure

(induced damage by mechanical and thermal stress) and bonding environments (through bonding improvers).

Steps towards measuring high-order parameters in larger concrete members were taken with the analysis of medium-size concrete beams. Scattered features of coda wave were used for damage identification in reinforced concrete beams with two main approaches. I) Coda-wave interferometry to measure dv/v during four-point bending tests: Variations of the CWI stretching technique are applied to calculate dv/v in three different ways of picking the reference measurement: Standard CWI, Step-wise/accumulate CWI, and Auto-reference CWI (Wang et al., 2020), differences on the analysed time-window, and the influence of the Poisson effect (Zhong et al., 2021), and the contribution of steel reinforcement strain (Clauß et al., 2022) to infer the structure's condition. II) Coda-wave interferometry to detect and locate cracks by the combination of the decorrelation parameter and sensitivity kernels (Eric Larose et al., 2015).

The complexity of field-condition concrete structures related to their geometry, structural composition, environmental effects, complications on stress measurement, and the non-controlled persistence of external solicitations represent challenges for accurately measuring high-order elastic constants and, therefore, harvesting information on their microstructural composition's state. Nonetheless, keen experiments on nonlinear effects in large concrete structures were carried out, where small velocity perturbations induced by changing stress states in a bridge under construction by the incremental launching method were estimated through coda wave interferometry (Stähler et al., 2011). The observed sensitivity of CWI in laboratory experiments was exploited on a real-size ballastless track (two concrete slabs superpositioned on top of a layer to mimic ground conditions) to investigate velocity changes due to fatigue damage. Classical stress-dependent effects were explained through the acoustoelasticity theory, and observations on thermal- and time-dependent (creep) elastic changes were obtained (Zhang et al., 2011). The CWI technique was combined with sensitivity kernels and measurements of acoustic emissions to monitor and map changes in the elastic properties of a 15-ton reinforced concrete beam subjected to a four-point bending load (Yuxiang Zhang et al., 2016). The feasibility of using diffusive waves at ultrasound frequencies in an on-site concrete structure to locate preexisting cracks was suggested with the analysis of an aeronautical wind tunnel in its routine operation, by mapping the density of microstructure changes in the bulk of the material (Yuxiang Zhang et al., 2018). Relative velocity variations as a function of stress and crack presence were investigated in more complex structures, like 1/3 scale mock-up of nuclear reactor concrete containment structure (Xue et al., 2022).

#### 1.1.2 Nonclassical nonlinear elasticity in concrete

The nonclassical component of the nonlinear elastic behavior in concrete is reflected on the anomalous time-dependence of DEP in phenomena like hysteretic damping, nonlinearity, discrete memory, and slow dynamics (SD) (Khandelwal and Chakrapani, 2021). Recording any of those phenomena demands sophisticated experimental setups. In essence, it first requires a system of continuous monitoring to record the material's response over time to the action of an external but coherent and controlled source of a given kinematic nature. The latter depends on which phenomenon is intended for analysis. Meeting those criteria in laboratory experiments is already highly complex, and

transferring those practices to field conditions for integrity assessment seems defiant. For sake of practicality, this research is focused on the analysis of SD.

SD is generally defined by two main elements: first, the sudden degradation of the materials' stiffness after the action of a moderate external perturbation (softening), and second, after this sudden degradation, the slow recovery or re-hardening process towards the material's initial stiffness, which occurs at logarithmic time scales (recovery process). As mentioned, this phenomenon is present in other materials like rocks (Ten Cate and Shankland, 1996), metal structures (Yoritomo and Weaver, 2020a), glass (Yoritomo and Weaver, 2020b), and also at large spatial scales like buildings (Astorga and Guéguen, 2020) and the earth structure (Gassenmeier et al., 2016).

There is no agreement on the physical mechanism responsible for this type of time-dependent phenomena. Still, research has invoked processes happening at the nanoscale, most specifically in the so-called bonding systems, as plausible causes, e.g., slip along grain boundaries and cracks (Brantut and Petit, 2022), the adsorption of fluid at the contacts between grains (Bittner and Popovics, 2021), the destruction and recreation of bonds in contact asperities (Sens-Schönfelder et al., 2019), contact sliding and aging (Asnar et al., 2025), and internal damage processes (Berjamin et al., 2017).

SD has been produced in concrete samples under laboratory conditions using different experimental procedures. Many of the differences rely on how mechanical stress is induced in the material, ranging from sophisticated methods such as Dynamic Acousto-Elastic Testing (Shokouhi, Rivière, Lake, et al., 2017; Bentahar et al., 2020), to practical variations of it, such as the Impact Dynamic-Acousto-Elastic Testing using Hammers (Jin et al., 2017) and Steel ball dropping (Larose et al., 2013) as a source of mechanical stress. Despite this difference, SD was observed to have significantly different effects in damaged and undamaged small concrete samples.

Experimental and theoretical work on nonclassical nonlinear elasticity in concrete is few but has increased in the last years. The high sensitivity of this phenomenon to the heterogeneity level of concrete enables investigation of the potential of this phenomenon to be translated into an NDT for concrete's integrity assessment at the material scale, and also to explore the possibility of complementing the current vibration-based method for integrity assessment at the structural scale by analysing the time-dependence of its parameters.

Developing nondestructive testing techniques and formalising them as standard techniques requires research from different perspectives. The exposed state-of-the-art of nonlinear elasticity in concrete evidences a dense experimental development under laboratory conditions, and this serves as a point of departure for the development of early-stage-damage assessment methods.

This research aims to transfer existing developments to the assessment of field-conditioned concrete structures, leveraging data processing methods and equipment originally developed in the field of seismology.

To this end, the present work is structured as follows: Chapter 1 presents an experiment conducted on a field-conditioned concrete test bridge known as the BLEIB structure. This structure, which is equipped with a prestressing system, is ideal for studying how stress- and time-dependent dynamic elastic properties (DEPs) behave, and how this behaviour relates to concrete heterogeneity (e.g., soft microstructures and micro-imperfections), using models and methods developed under laboratory conditions. This chapter details the stress- and time-dependent elastic behaviour recorded using ultrasound equipment and compares it with standard nondestructive tests (NDTs),

such as ultrasonic pulse velocity (UPV), in a cooperative interpretation. The results suggest a correlation between nonlinear elastic behaviour and the relative integrity level of the concrete structure, supporting the identification of varying heterogeneity levels along the bridge and offering a qualitative description of the plausible underlying microstructures responsible for such behaviour.

Chapter 2 connects the observed softening and recovery processes during the experiment with the models developed in the last decades to reproduce such behaviour. It provides a broad overview of these models and uses one of them to propose an analytical expression that captures the cumulative effect of Slow Dynamics in concrete with varying levels of integrity, subjected to different compressive force levels. This proposed expression enables a quantitative analysis of the stress-dependent Slow Dynamics effect and its behaviour across concretes of differing integrity, using a probabilistic data inversion process. A key outcome of this chapter is the validation of the observations presented in Chapter 1 through an analytical model. As a result, the chapter also provides practical guidelines for inducing nonlinear elastic effects in field-conditioned concrete structures.

Chapter four exposes the results obtained with the low-frequency data. Conventional seismic equipment, such as one-component vertical geophones, was used to estimate stress-dependent elastic behaviour. Two stress-dependent elastic phenomena were analysed here: I) Relative velocity changes on the vibration velocity of the fundamental standing wave of the bridge and II) Attenuation via coda wave decay. This chapter discusses the functionality and limitations of this equipment and the associated methodologies, and how they could be integrated into structural health monitoring techniques.

The final part of this investigation presents the key outcomes of the work, outlines its limitations, and suggests directions for future research in the form of conclusions and outlook.

The long-term goal of this work is to contribute to the expansion of the continuum of nondestructive testing techniques by developing integrity assessment methods that are highly sensitive to micro-imperfections. These techniques, based on the analysis of mechanical wavefields, aim to promote early-stage damage assessment.

Marco Dominguez-Bureos, Christoph Sens-Schönfelder, Ernst Niederleithinger, Celine Hadziioannou

This chapter is in revision at The Journal of Nondestructive Evaluation.

2

## Stress- and time-dependent variations of elastic properties for integrity assessment in a reinforced concrete test bridge

This chapter presents an experiment conducted on an outdoor-conditioned concrete structure to measure stress- and time-dependent elastic properties, referred to as classical and nonclassical nonlinear elasticity, respectively. This section reports the results obtained using ultrasound equipment, with relative velocity changes serving as a proxy for elastic properties. The elastic properties are quantified and compared with Ultrasound Pulse Velocity (UPV), a conventional nondestructive testing technique, and interpreted in relation to the concrete's heterogeneity levels. This chapter demonstrates the usefulness and functionality of nonlinear elasticity in identifying soft microstructures and observing their dynamics in real-world concrete structures.

#### **Contents**

2.1	Introduction		
2.2	Experiment		
	2.2.1	Stress Protocol	13
	2.2.2	Preprocessing and temperature corrections	14
2.3	Theoretical framework and Methods		15
	2.3.1	Linear Elasticity	15
	2.3.2	Classical Nonlinear Elasticity	15
	2.3.3	Nonclassical Nonlinear Elasticity	16
	2.3.4	The Coda Wave Interferometry	17
2.4	Results		18
	2.4.1	Observations on Linear elasticity	18
	2.4.2	Observations on Classical Nonlinear elasticity	18
	2.4.3	Observations on Nonclassical Nonlinear elasticity	19
2.5	Discussion		

2.6	Conclusion				
	2.5.4	Cross-plots	24		
	2.5.3	Velocity drops	22		
	2.5.2	Acoustoelastic effect	21		
	2.5.1	P-wave velocity	21		

The existing civil engineering nondestructive testing techniques (NDT) based on mechanical wavefields excel in identifying focalised anomalies using different wave modes, i.e. bulk waves (Gholizadeh, 2016) (compressional and shear) and guided waves (Moll et al., 2020) (surface and Lamb waves). These techniques, rooted in Linear Elasticity (LE) paradigms, relate dynamic elastic moduli or wave velocities to the structural integrity in bounded volumes. Their functionality, therefore, relies on the challenging task of tailoring the wave mode features to the unknown size of imperfections. In this context, identifying small-scale imperfections is an elaborate but crucial task to prevent large-scale cracking or failure; this requires developing NDT techniques sensitive to heterogeneities smaller than the wave mode features.

An approach to address this problem is to analyse concrete structures from the perspective of Nonlinear Elasticity. In recent decades, lab-conditioned experiments demonstrated that, at the material scale, the evolution of (static or dynamic) elastic properties of composite solids like concrete performs according to the dynamics of their constitutive microstructural elements (Guyer and Johnson, 1999). When the material is perturbed within its elastic regime (strains from  $10^{-4}$  to  $10^{-7}$ ), (Guyer and Johnson, 2009), it triggers a systematic elastic evolution that exhibits a classic response when analysed as a function of stress, and a nonclassic response as a function of time. This elastic evolution promotes a material description in terms of its instantaneous elastic moduli, higher-order constants, and phenomenological variables that react to interactions of structures at micro/nano scales. Nonlinear elastic phenomena enable the possibility of identifying small-scale imperfections in concrete using mechanical wavefields.

The classical response refers to the evolution of elastic wave speeds as the stress state of the material changes (Pao and Gamer, 1985), a phenomenon conventionally referred to as the acoustoelastic effect (AEE). Numerical models address this phenomenon by formulating stress as a nonlinear function of strain (Niu et al., 2024), earning the distinction of Classical Nonlinear Elasticity (CNE) commonly observed in complex solids. This nonlinear theoretical framework served to estimate concrete's dynamic elastic properties at different mechanical load levels to investigate the influence of micro imperfections in high-performance concrete (Raju, 1970) and in concrete samples of mixes at different proportions (Suaris and Fernando, 1987). The sensitivity of wave polarisation to the direction of stress loading was observed to be significant for the acoustoelastic effect (Jean-François Chaix et al., 2008; Lillamand et al., 2010). Different wave modes, like surface waves, were combined with acoustic emissions measurements to analyse the contribution of stress and damage on measured velocities (Shokouhi et al., 2010). Methodologies of limited spatial sensitivity, as the well established ultrasonic pulse velocity method (UPV) is (Singh et al., 2019), demonstrated to be suitable for measuring CNE effects and their relationship with small-scale damage.

Wave interferometry (WI) emerged in seismology (Lobkis and Weaver, 2003; Sens-Schönfelder and Wegler, 2006; Hadziioannou et al., 2009; Hadziioannou et al., 2011) as an alternative tool to estimate relative velocity changes (dv/v) with a widened spatial sensitivity; an option to circumvent the spatial sensitivity restrictions of UPV. WI leverages the scattering feature of the Earth's structure imprinted in the late wave train of seismic recordings, usually called the coda wave. Coda Wave Interferometry (CWI) demonstrated to be an outstanding, sensitive technology for quantifying minor stress variations (of the order of tens of kPa) in concrete (Larose and Hall, 2009), and combined with the acoustoelasticity theory, served to analyse: 1) The effects of compression and tension in concrete cores (Diewald et al., 2022), 2) the anisotropy to determine highorder elastic constants of concrete (Cedric Payan et al., 2008; Payan et al., 2009), 3) different damage mechanisms like thermal shock and cyclic loading (Schurr et al., 2011) to separate thermal from mechanical effects (Yuxiang Zhang et al., 2012), 4) the impact of bonding improvers in mixes of high- and ultra-high-performance concrete (Ankay and Zhang, 2019), and 5) the contribution of different portions of the ultrasound waveform in the estimation of dv/v, i.e., direct P-Wave interferometry (Zhong et al., 2021). It should be stated that the studies mentioned above were conducted under laboratory conditions where the acoustoelastic effect and, therefore, certain higher-order elastic constants estimated with CWI, demonstrated to be reactive quantitatively to the damage level of the sample. A small number of investigations were extended to large-scale specimens like concrete beams (Wang et al., 2020; Moradi-Marani et al., 2014; Clauß et al., 2022), and field-conditioned concrete structures (Stähler et al., 2011; Wang et al., 2021; Yuxiang Zhang et al., 2011; Yuxiang Zhang et al., 2016; Xue et al., 2022).

The Nonclassical response in the Nonlinear Elastic behaviour, known as Nonclassical Nonlinear Elasticity (NNE), of concrete refers to the anomalous time-dependent elastic effects like hysteretic damping, nonlinearity, discrete memory, and Slow Dynamics (SD) (Khandelwal and Chakrapani, 2021). Although the physical mechanism of SD remains enigmatic (Asnar et al., 2025), it has significantly different effects in damaged and undamaged small concrete samples from the perspective of different experimental procedures to estimate changes in elastic properties, e.g., Diffuse Acoustic Wave Spectroscopy (Eric Larose et al., 2013), Dynamic Acousto Elastic Testing (Shokouhi, Rivière, Lake, et al., 2017), and Modulus and Damping Nonlinearities Estimation approach (Bentahar et al., 2020). At the structural scale, SD has been observed by monitoring the earthquake-induced change in the natural frequency of buildings (Astorga et al., 2018).

To date, the reported theoretical and experimental work related to concrete is extensive in the context of CNE, and fewer but increasing in the context of NNE. However, many pioneering observations and models are obtained in laboratory setups on concrete cores or concrete beams, and their promising applicability in field-condition full-size concrete structures is still to be investigated. The present work extends the out-of-lab observations of the AEE and the softening and relaxation processes, elements of SD. We monitor the effect of vertical impulsive sources (transient effects) at different compressive forces (static changes) on ultrasound wave velocities recorded at four locations of a full-scale, field-conditioned reinforced concrete test bridge to investigate spatial variations in heterogeneity and their relationship with the bridge's integrity.

This study outlines the experimental protocol and the detailed data processing workflow followed by the theoretical foundations of the employed methodologies. We report the results of the three elastic regimes separately and the discussion in the form of a cooperative analysis of LE, CNE, and NNE. Our overall aim is to comple-

ment existing damage assessment methodologies, such as UPV, with microstructuralsensitive measurements to suggest a relative measure of concrete integrity and insights related to its heterogeneity level that best explain the recorded dynamics of concrete's elastic behaviour.

#### 2.2 Experiment

The experimental investigation was conducted in a 24-meter-long, inverse U-shape, reinforced concrete test beam (the BLEIB structure at the BAM test site for technical safety 50 km south of Berlin, Germany) equipped with a pretension system that compresses the structure with controlled forces in its longitudinal direction (Figure 2.1). The experimental investigation consisted of tracking a) instantaneous velocity estimated via UPV, b) dv/v with stress, and c) dv/v over time after the influence of impulsive sources, using WI (as a proxy for the concrete's dynamic elastic properties) in four places of the BLEIB structure. To achieve this, active and passive recordings of wave propagation at different frequency bands were obtained in the concrete bridge when subjected to compressive forces at different magnitudes for approximately six hours.

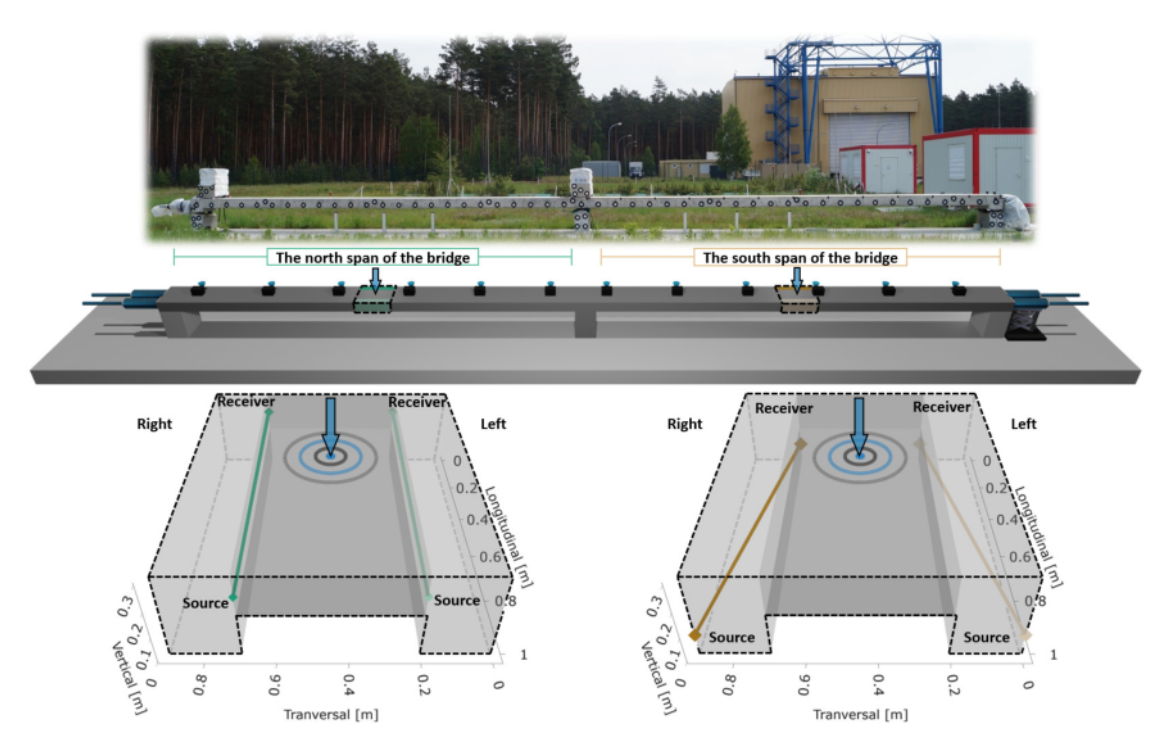


Figure 2.1: Upper panel: the BLEIB reference structure. Mid panel: a schematic representation of the BLEIB structure, the prestressing system, and the geometry of the sensor arrays; the linear array of six-component sensors (black boxes) adjacent to the linear array of one-component geophones (blue inverted cones) used during the experiment are also shown. Lower panel: a zoom in view on the spans of the bridge where the four pairs of ultrasound transducers are embedded (dark green, light green, dark brown, and light brown); the straight line represents the source-receiver straight ray path; the blue arrow shows the place where the weight-drop source was activated to induce softening on the concrete.

Four pairs of 60 kHz-central frequency embedded Ultrasound Transducers (UST) were used to monitor five-second material changes of the concrete (active recordings) at

four different locations on the test bridge, North-Left (NL), North-Right (NR), South-Left (SL), and South-Right (SR) as shown in Figure 2.1. This type of ultrasound transducers has been characterized and successfully applied in several experiments (Niederleithinger et al., 2018; Niederleithinger et al., 2015). Due to limitations of the ultrasonic acquisition system, it was not possible to record simultaneously on the four locations; therefore, we worked first on the North span (both left and right) and then moved to the South span. The results presented in this paper concern the database recorded with this equipment.

Passive recordings of low-frequency ambient vibrations were obtained during the experiment by setting up twelve recording spots on top of the bridge. Each recording spot consisted of a vertical-component geophone of 500 Hz sampling frequency colocated with a six-component sensor (three components to record acceleration and three more to record the angular velocity rate) of 400 Hz sampling frequency. The distance between recording spots was approximately 1.15 meters. One more recording spot on the bridge's foundation and one more in the natural subsoil, three meters away from the centre of the structure, were placed.

#### 2.2.1 Stress Protocol

The stress protocol is presented in Figure 2.2a, where changes in compressive force in kN are shown with time, and assuming a homogeneous compression in the cross-section area of the specimen, the conversion to MPa on the right-side vertical axis. It is worth noting that the compressive force is kept at 350 kN when no experiments are performed to avoid any long-term bending by gravity.

At the beginning of the experiment, the structure was compressed with a force of 400 kN (2.05 MPa). The ultrasound acquisition system was first activated on the North span, as shown in Figure 2.2a (green line segment between 09:45 and 10:06), to record one ultrasound pulse every five seconds, each lasting five milliseconds and sampled at 2 MHz (refer to figures 2.2b and 2.2c). First, one minute of baseline data composed of approximately 12 ultrasound pulses (hereafter referred to as the baseline phase) was recorded to capture variations in the elastic properties of concrete induced by the prestressing system; then, a vertical impulsive drop weight was triggered on top of the North span of the bridge in the middle of the USTs (Figure 2.1 blue arrows) to induce reversible damage and its subsequent auto-healing process (relaxation process) on the concrete as an experiment of NNE. This effect was recorded over five minutes; the impulsive source was activated in the same manner three times. After the oneminute baseline phase and the activation of the three impulsive sources and their relaxation processes (16 minutes approx), the ultrasound acquisition system was turned off on the North Span of the bridge and activated on the South Span to perform the same experimentation as on the North Side. Once this procedure was completed on both sides of the bridge, the compressive force was reduced to 370 kN (1.89 MPa) to carry out the same protocol.

This protocol was repeated 5 times in the decompression stage of the experiment (going from 400 kN to 280 kN at steps of 30 kN) and 3 times in the compression stage (going from 280 kN to 400 kN, skipping 370 kN). Eight compressive force levels were analysed in total, and at every level, two types of information were recorded: one minute of baseline phase just after changing the compressive state on the bridge and the effect of the set of three impulsive sources. A total of 2,030 ultrasound pulses were recorded on each side of the north, and 1,730 on each side of the south span of the bridge; the

difference is due to the continuous recording on the north span of the bridge during the lunch break (Figure 2.2 shadowed green area between 11:52 and 12:12 hrs.).

As stated, this experiment is designed to study changes in the elastic properties of concrete within the elastic regime. The external solicitations to the specimen constitute superimposed effects of transient sources (dynamic changes) at different compressive force levels (static changes) on the bridge. The stress distribution on a horizontal concrete beam is complex but generalised in tension, neutral, and compression zones (Clauß et al., 2022). Since we compress and decompress the structure, the tensile and compressive zone on the beam might also be subjected to changes. In this experiment, the minimum and maximum compressions are 1.43 and 2.05 MPa, respectively, which means 1.68% — 2.41% of reinforced concrete's compressive strength, based on the values reported in (Song and Hwang, 2004).

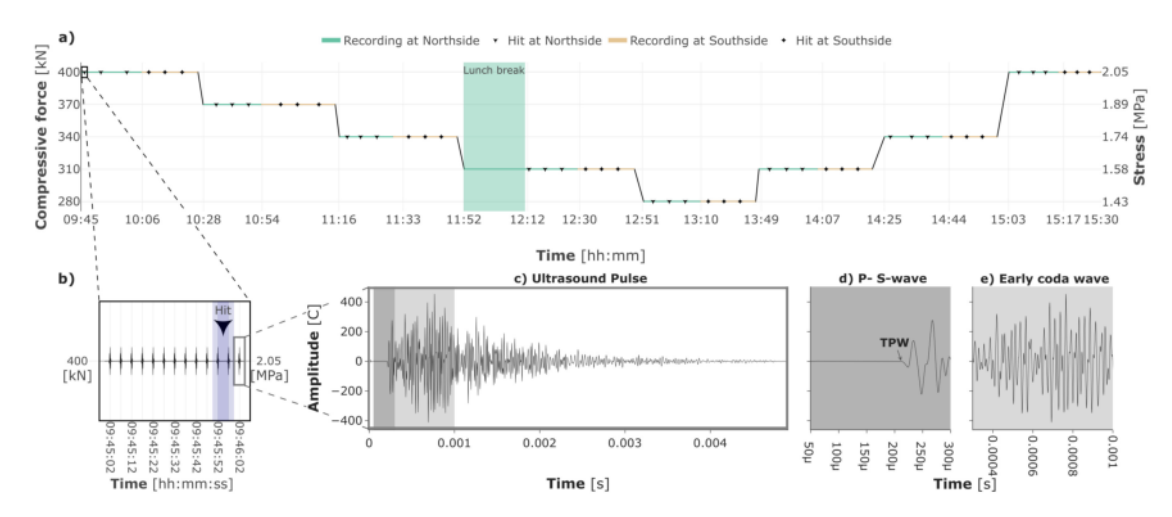


Figure 2.2: a): The variations of stress followed during the experiment with respect to time; the recording time slots on the Northside (light green line segments) and Southside (light brown line segments); the inverted triangles denote the activation instances of the impulsive source on the Northside while the diamonds represent those on the Southside. b) An inset to the stress protocol that shows one Ultrasound Pulse every five seconds was recorded during the experiment. c) The features of the recorded Ultrasound Pulses. d) Inset to the time window used to estimate the Ultrasound Pulse Velocity (TPW) and the portion of the pulse used to estimate concrete's nonlinear classical effects (P-S wave), and e) the nonclassical nonlinear effects (Early coda wave).

#### 2.2.2 Preprocessing and temperature corrections

Each ultrasound pulse was subjected to a pre-processing stage to remove the undesired effect while recording. This stage comprises the removal the pretrigger effect (200 samples), a linear trend, and the cross-talk effect, this last one by applying a 4% tapered cosine window (equivalent to smoothing the first and last 0.000196 seconds of the signal) to affect as little as possible the early part of the waveform. A second-order Butterworth band-pass filter (10-150 kHz.) was applied to each signal. Figure 2.2 (c) shows an example of the pre-processed ultrasound pulse used for further analysis.

The BLEIB structure acts as a reference structure in field conditions exposed entirely to the abovementioned factors. As a strategy to reduce the influence of thermal and chemical effects due to environmental factors, all the dv/v measurements were corrected by temperature effects; temperature recordings during this experiment, and models of

dv/v as a function of temperature at different seasons along one year obtained for the same structure (Liao and Barroso, 2022) were used to carry out this correction. All dv/v values shown in this paper are considered corrected by first-order temperature effects, enhancing the effects due to mechanical stress (compressive forces and vertical impulsive sources); nonetheless, the higher-order effects still have an imprint on our estimations.

#### 2.3 Theoretical framework and Methods

#### 2.3.1 Linear Elasticity

To investigate the linear elastic properties, we use the UPV method, which has been widely employed to evaluate the quality of concrete. As part of the standard non-destructive testing methodologies, this technique uses low-strain amplitude mechanical waves travelling through the material to investigate wave velocity (usually compressional waves), knowing the first arrival travel time of the first wavefront and the transmitter-receiver distance. Picking the first arrival travel times is often done manually; a lot of different automatic picking algorithms have been proposed, from simple threshold pickers to more sophisticated ones based on statistical criteria (Niederleithinger et al., 2015). In this work, we employed a manual approach, subsequently verified using the STA/LTA picker (Beyreuther et al., 2010). Further information about the methodological procedures can be found in (Naik et al., 2003) and (ASTM Test Designation C 597-02, Standard Test Method Pulse Velocity through Concrete, n.d.).

Analytically, it can be suggested that, in the linear elastic regime, high p-wave velocity values are related to stiffer materials through the following equation:

$$V_p = \sqrt{\frac{E(1-\mu)}{\rho(1+\mu)(1-2\mu)}},$$
(2.1)

Where E is the young modulus (or dynamic modulus of elasticity),  $\mu$  is the Poisson's ratio, and  $\rho$  is the density of the material. The value of the expression  $(1-\mu)/(1+\mu)(1-2\mu)$  varies within a fairly narrow range, for example, as  $\mu$  increases from 0.15 to 0.25 (67 % increase), the associated expression increases from 1.06 to 1.20 (12 % increase). Thus, the variations in E and P0 have a more significant effect on E1 than variations in E2.

In practice, this statement remains valid considering the observations made in lab experiments, where high P-wave velocities were obtained in concrete with high compressive strength (Ghaffari Moghaddam et al., 2022; Mata et al., 2023).

#### 2.3.2 Classical Nonlinear Elasticity

Acoustoelasticity is probed using relative velocity changes for varying external stress. These velocity changes are estimated using relative travel time changes of the first wave arrival or via WI, as employed in this study. The acoustoelasticity theory provides a mathematical framework to numerically describe such stress-dependent variations. In 1937, Murnaghan (Francis Dominic Murnaghan, 1937) described the underlying physics of the effect of applied mechanical stress upon the second-order elastic constants of a given material. Hughes and Kelly (Darrell S Hughes and John L Kelly, 1953) extended Murnaghan's work and derived analytical expressions of wave velocities and stress for

isotropic media under hydrostatic pressure. This set of analytical expressions allows evaluating Murnaghan's constants using anisotropic measurements of the first arrival travel times of elastic waves in a given medium. When performing linearisation of the set of analytical expressions in the first order, the system becomes

$$c_{ij}^{\sigma} = c_{ij}^{0} \left( 1 + A_{ij} \sigma_{11} \right) \tag{2.2}$$

where  $c_{ij}^{\sigma}$  is the velocity of wave propagating in direction i and polarized in the direction j in a medium under uni-axial stress  $\sigma_{11}$  in the direction 1,  $c_{ij}^{0}$  is the same wave velocity in the stress-free medium, and  $A_{ij}$  are the acoustoelastic constants which depend on the Lame's and Murnaghan's coefficients. The acoustoelastic theory provided by (Darrell S Hughes and John L Kelly, 1953) may be used for concrete materials when considered as a homogeneous isotropic medium.

Two considerations were made to improve the quality of the stress-dependent dv/v estimations in the present experiment.

- 1. Reference and deformed measurements: To reduce the time-dependent effects of the static changes, the ultrasound pulses recorded during the baseline phase at every compressive force were stacked. The reference measurement is the stacked ultrasound pulse at 400kN at the beginning of the experiment (Stacking the measurements recorded from 09:44:47 to 09:45:47 in Figure 2.2b), and the deformed states are the stacked ultrasound pulses at every subsequent compressive level.
- 2. Time window: The selected time window for this analysis is shown in Figure 2.2d (P-S-wave shaded in dark grey), this is due to the sensitivity of the particle motion to the direction of the applied force for the dv/v estimations (Zhong et al., 2021).

#### 2.3.3 Nonclassical Nonlinear Elasticity

To investigate the nonclassical nonlinear effects, we study the transient response of the specimen to an external excitation. In particular, we focus on the velocity drop and recovery process — the SD phenomenon — following the impact of a repeatable drop weight, which we monitor using CWI. The SD phenomenon has no unique definition, but it finds its formal description in lab experiments where three main phases constitute it: 1) conditioning, 2) Steady-state, and 3) Recovery process (refer to (Niu et al., 2024) for more information). The way an elastic material reacts instantaneously to the action of a transient strain field (statically, dynamically, or thermally induced) is referred to as softening (this is because the material tends to be weakened), and the long-term performance of the material is referred to as the relaxation process. This instantaneous reaction and long-term performance of a material's elastic properties have been shown to happen differently in bodies with the same material composition but subtle differences in their microstructure (porosity, water content, and microcracks).

Significant attempts have been made to mathematically model SD with foundations in physical processes (Snieder et al., 2017; Shokouhi, Rivière, Guyer, et al., 2017; Sens-Schönfelder et al., 2019) as a function of different sets of variables. Qualitatively, the standard features of this relaxation process can be isolated as:

1. The velocity decrease (softening effect of the material): This is the abrupt change in the elastic properties that documents the body's elastic degradation due to the transient strain field.

2. The logarithmic time-dependent evolution of the recovery process: As time progresses, the material tends to return to its elastic estate before the transient strain field's action as an auto-healing process; the time span of this effect is significant and seemingly quantified adequately as a logarithmic function of time.

In this experiment, the material's softening effect is induced by the action of a vertical impulsive source. The time-dependent evolution of the recovery process is measured over 5 minutes with dv/v estimations used as a proxy for the material's elastic properties. As the stress protocol states in Figure 2.2, at each static condition, the impulsive source was triggered three times on the north side in the central position between the ultrasound transducers (Figure 2.1) and three times on the south side in the same fashion.

The high sensitivity of WI to weak changes now plays an important role. The concrete's microstructure undergoes significant changes during the experiment as dynamic transient fields are superposed on different static states, leading to low similarity between waveforms. Two considerations were made to improve the quality of the time-dependent dv/v estimations in this experiment.

- 1. Reference measurement: The reference waveform was renewed at every compressive level to account for changes induced by variations of the static stress.
- 2. Time window: The selected time window for this analysis is shown in Figure 2.2 (Early coda wave shaded in light grey), this selection was used to increase the sensitivity of the velocity change measurements.

#### 2.3.4 The Coda Wave Interferometry

In this paper, the CWI stretching technique (Sens-Schönfelder and Wegler, 2006; Hadziioannou et al., 2009) is used to estimate dv/v. This technique has been used to monitor high-precision changes in elastic properties at scales ranging from rock (Asnar et al., 2025) and concrete samples to volcanoes (Makus et al., 2024) and the Earth's structure (Martina Gassenmeier et al., 2016). The stretching method is based on the assumption that a waveform, u, recorded when the medium was perturbed, is a stretched version of a waveform,  $u_0$ , recorded when the medium was at a reference state. Furthermore, the stretching is assumed linear with the relationship:

$$\tau = \epsilon t, \tag{2.3}$$

where  $\tau$  is the local travel time change and  $\epsilon$  is the stretch factor related to the homogeneous velocity perturbation as  $\epsilon = -\Delta V/V$ . In practice, the time axis is stretched as  $t' = t (1 + \epsilon)$ ; therefore, a decrease in velocity causes a lengthening of the time axis. After stretching u(t) the zero-lag cross-correlation is computed over the window  $[t_1, t_2]$ :

$$CC(\epsilon) = \frac{\int_{t_1}^{t_2} u_0(t)u(t')dt}{\sqrt{\int_{t_1}^{t_2} u_0(t)dt \int_{t_1}^{t_2} u_0(t')dt}}.$$
 (2.4)

To estimate the optimal stretch factor, many  $\epsilon$  values are tested and searched for the maximum zero-lag cross-correlation coefficient (Mikesell et al., 2015).

#### 2.4 Results

#### 2.4.1 Observations on Linear elasticity

As the ultrasound transducers are embedded in the bridge and the ray path of the p wave is assumed to be straight, the compressional wave samples the innermost structure of the bridge, avoiding the external layer, which is assumed to be the lower-quality concrete layer due to weathering action (e.g., freezing and thawing, sulfate attack, and corrosion of reinforcement and other embedded items). The estimated values of P-wave velocity in the four different locations are plotted in Figure 2.3. Each value represents the mean of the P-wave velocities estimated with the ultrasound pulses recorded in the baseline phase at the eight different compressive force levels. Noting the P-wave velocity difference between north and south spans is significant (6.85%), and placement uncertainty of the transducers (of the order of 1-2 cm) does not explain such difference.

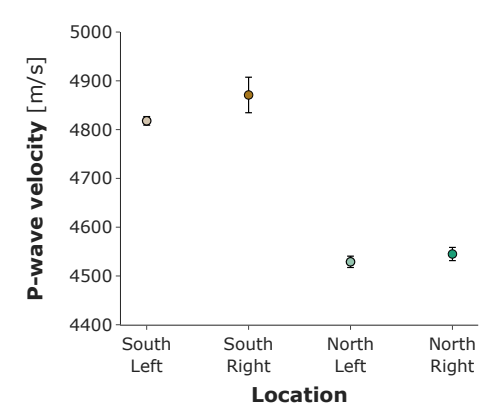


**Figure 2.3**: Observations of linear elasticity. The estimated ultrasound pulse velocity at every location on the bridge.

#### 2.4.2 Observations on Classical Nonlinear elasticity

The relative velocity changes dv/v are estimated as a function of the stress state. For this analysis, the reference state ( $u_0$  in the equation 2.4) is obtained by stacking all the ultrasound pulses recorded in the baseline phase when the structure was compressed with 400 kN (2.05 MPa) at the beginning of the experiment; the deformed states (u in the equation 2.4) are, therefore, the stacked ultrasound pulses of the baseline phase at every subsequent compressive force. This procedure improved the maximum cross-correlation coefficient obtained in the stretching process and suggested reducing the time-dependent effects due to the static change during this one-minute time span.

The selected time window is shown in Figure 2.2d, shaded in dark grey. This chosen time window covers the ultrasound pulse from 50 to 300 microseconds, mostly capturing the compressive wave and converted waves in the late part, and avoids the crosstalk effect at the beginning of each ultrasound pulse. This analysis uses the P-wave to preserve a parallel contribution of the direction of the applied stress on the bridge and the particle motion of the probing wavefield.

Figure 2.4 shows the results of the stress-dependent analysis in the four tested sites in the bridge. The left-side section of this figure shows dv/v [%] versus compressive force [MPa]. Dots show relative velocity changes while releasing the compression, and crosses are estimations while compressing the structure again. The variance estimation method of dv/v developed by (Weaver et al., 2011) as a function of the maximum cross-correlation coefficient, the time window size and the central frequency was used in this research. As mentioned before, the reference state is the first compressive force in the experiment, so no dv/v is observed at 2.05D MPa. The relationship between stress and the dynamic elastic properties (wave velocities or elastic moduli) is observed linearly, as in lab experiments. The weighted linear regression technique was used to estimate the parameters of such linear models in the decompressing and compressing stages.

The slope of this linear model is directly related to the so-called acoustoelastic effect. In Figure 2.4 (e), the slopes of the linear models are plotted for each site in the bridge; dots correspond to slopes obtained in the decompressing stage and crosses in the compressing stage.

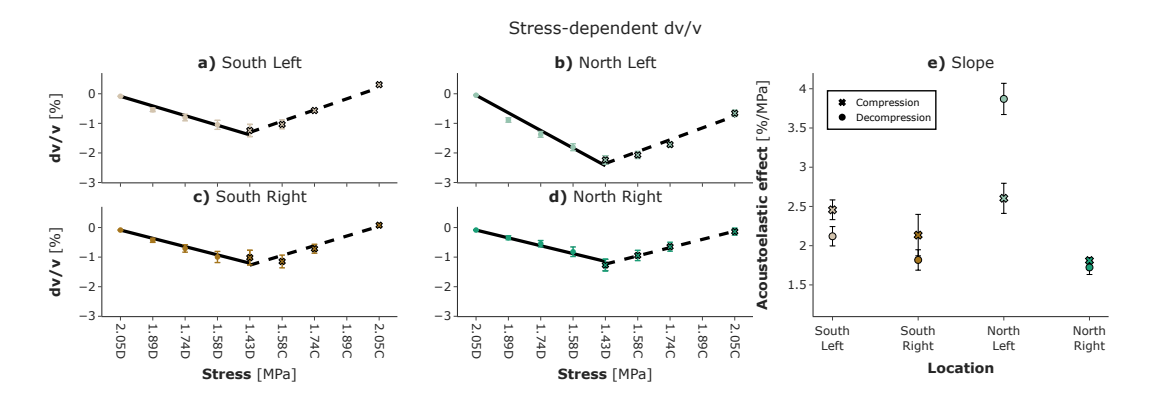


Figure 2.4: Observation of classical nonlinear elasticity. From a) to d) plots of the relative velocity changes as a function of the applied compressive forces for the four locations (D and C in the x-axis stand for Decompressive and Compressive stages); dots indicate velocity changes during decompression, and the solid black line the linear model that fits the estimations; similarly, crosses and the dashed black line represent velocity changes and the corresponding linear model during compression. e) Plots the slope of each linear model; dots indicate the slopes of measurements while decompressing, and crosses indicate the slopes of measurements while compressing. The slope is referred to as the Acoustoelastic Effect.

#### 2.4.3 Observations on Nonclassical Nonlinear elasticity

The results of NNE are consigned in Figure 2.5. In a), relative dv/v values are plotted for the four locations as a function of time. Starting at 09:45 hrs on the north side (left and right), over time, two effects are observed: 1) the baseline phase and 2) the effect of the three impulsive sources. After approximately 16 minutes, the results from the south span are shown in the same manner, both at a compressive force of 400 kN (2.05 D). In the lower section of Figure 2.5a, the cross-correlation coefficients obtained after the stretching method are shown; the vertical dashed line represents the ultrasound pulse used as a reference for each side at every different compressive force.

An inset of the results recorded on the NR side of the bridge at a compressive force of 310kN (1.58 C) is shown in Figure 2.5b. Here, the baseline phase and the

effect of the three impulsive sources are shown. As a consequence of each impulsive source, the two components of the SD process are identified: the velocity drop and logarithmic relaxation.

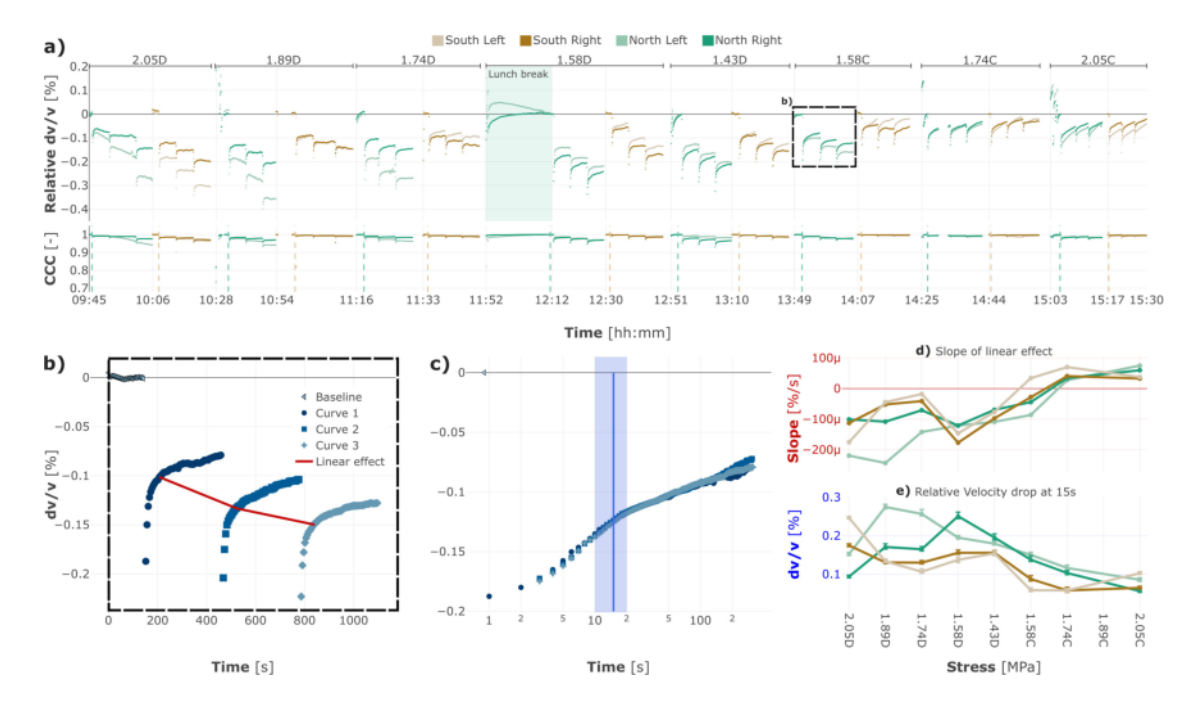


Figure 2.5: Observations on nonclassical nonlinear elasticity. a) The relative velocity changes as a function of the time in the four locations (the effect of the vertical impulsive sources) and the cross-correlation coefficient (CCC) obtained with the stretching method; the vertical dashed lines show the reference measurements for the stretching. b) Inset to show the baseline phase (triangles) and the effect of the three impulsive sources (the three blue curves). The red line shows the linear effect that shifts and deforms the three relaxation processes through time. c) The superimposed relaxation processes after the matching curve analysis. The vertical blue line marks the second  $15 \pm 5$  seconds to estimate the relative velocity drop. d) The slope of the linear effects observed at every compressive level on the four locations of the bridge. e) The relative velocity drop at  $15 \pm 5$  seconds, measured at each level of compressive force on the four locations of the bridge.

A third effect is present: a linear behaviour superimposed on the relaxation processes that shift the measurements vertically and reshapes the logarithmic curves in the late part of them, it is plotted in Figure 2.5b, red line. To quantify this effect, a curve matching analysis is performed. This analysis is based on the assumption that all relaxation processes in the experiment share similar source features such as energy, mechanism, applied direction, and location. Therefore, there is a point in time up to which the similarity between the three processes remains at its maximum. The curve matching analysis searches for this point in time as follows:

- 1) Resample the relaxation processes to obtain information every second, rather than every five seconds.
- 2) Gridsearch in the dv/v and time space to find the overlapping with the lowest error between the three of them, taking as a reference the position of the first relaxation curve (Figure 2.5c as an example). We obtain the dv/v and time coordinates of shifting the second and third relaxation curves.

3) Linear regression using the set of coordinates to obtain the slope of the linear behaviour. The slope of this linear regression is plotted in Figure 2.5d.

Two caveats are worth noting: During the experiment, 1) there was no triggering system to initiate the ultrasound measurements immediately after the action of the impulsive source, and 2) the latest recorded information of each relaxation process was five minutes after it started. Therefore, estimating the minimum and maximum relaxation timescales of such a logarithmic effect would result in inaccurate outcomes; however, the amplitude of this effect remains meaningful. The softening of concrete was estimated by measuring the relative velocity drop at 15  $\pm$ 5 seconds, plotted in Figure 2.5e, meaning the difference between the dv/v at the baseline phase and the dv/v at 15  $\pm$ 5 seconds after the action of the impulsive source.

## 2.5 Discussion

The primary purpose of this work is to investigate the feasibility of measuring I) instantaneous elastic properties, II) classical nonlinear properties, and III) nonclassical nonlinear properties of a field-conditioned test bridge. We condense a summary of the results in Figure 2.6.

## 2.5.1 P-wave velocity

As a starting point, the analysis centres on P-wave velocities estimated at the four locations on the bridge shown in Figure 2.6b. Relatively high P-wave velocities are measured in the South span: SL 4818 m/s, and SR 4871 m/s, and considering the standard deviation of those measurements, there is a difference of 7.82 m/s. In contrast, the North Span exhibited relatively low P-wave velocities: NL 4529 m/s and NR 4545 m/s; the standard deviation of these measurements suggests an irrelevant difference. The North span exhibited an average P-wave velocity decrement of 6.85% concerning the maximum value; this difference suggests lower values of dynamic elastic properties in the North Span (assuming a constant concrete density) and, therefore, less uniformity in the concrete. The sensitivity of these observations is limited to the zones through which the assumed straight ray path is travelling.

## 2.5.2 Acoustoelastic effect

The AEE evidences changes in the elastic properties as the stress conditions applied to the material evolve. Figure 2.6d shows the estimations in the four locations for decompressing (solid dots) and compressing (crosses). The possible candidates to explain these changes are the following: 1)changes in the geometry/shape of the structure, meaning that the transducer-receiver distance is shortened/elongated by the action and direction of the applied force. 2) Crack propagation, where new voids are created when the external solicitations exceed concrete's compressive/tensile strength, that is, deforming the structure beyond concrete's elastic regime. 3) The void volume in concrete changes as the structure is tensed/compressed, implying either increment/decrement in the porous space and/or opening and closing of preexisting microstructures that soften/strengthen the bridge as the compressive force changes (i.e. microcracks).

Assuming the measured AEEs are the consequence of shape changes in the structure (1), variations in the ray path length (related to variations in the transducer-receiver distance, and therefore to static deformation) of the order of 1.88 to 2.21 cm per applied MPa for the South side, and 1.72 to 3.87 cm per applied MPa for the North side are expected, meaning an anomalous inhomogeneous deformation occurring along the bridge that is less likely to occur.

Previous experiments on the same structure explored higher compressive forces than this experiment, so the crack initiation and propagation process (2) may have taken place beforehand, if at all.

The time window used to estimate relative velocity changes includes the full contribution of compressive waves whose particle motion is parallel to the direction of the applied force and, therefore, sensitive to material changes in this direction. This suggests the presence of microstructures (3) whose dynamic is activated as the compressive force changes (i.e. tensile cracks, or the tensile component of more complex microcracks, with the plane of crack perpendicular to the direction of the applied force) and the spatial variability of this behaviour along the bridge is related to different number densities of such soft microstructures at every location on the bridge.

The higher AEE values are measured on the NL side of the bridge for both increasing and decreasing stress (above 2.5 %/MPa), which suggests a high density of soft microstructures dominantly activated during decompression; nevertheless, the dynamic of such elements is still considerably higher during compression compared with the three other analysed places. This is in contrast to the NR side, which exhibits lower AEE values while decompressing and compressing, implying a low density of soft microstructures or soft microstructures poorly activated by stress changes due to interlocking or rough surface effects.

The SL and SR sides present average values concerning the North span. Slightly lower AEE values were obtained in the SR than in the SL during decompression and compression. Broadly speaking, the difference in AEE values during compression and decompression stages is the same for the SL and SR sides. This suggests a relatively low to moderate density of soft microstructures on the SR side and a moderate density on the SL side, similarly activated during decompression and compression.

A more precise interpretation related to the number density of microstructures will be provided through cross-plot analysis.

## 2.5.3 Velocity drops

The velocity drop (softening, elastic degradation) is part of the slow dynamics process, a nonclassical nonlinear elastic effect. Although the physical mechanism responsible for this phenomenon remains an open research question, it is thought to have causes at Mesoscopic/nanoscale elasticity (Ostrovsky and Johnson, 2001; Johnson and Sutin, 2005; Guyer and Johnson, 2009; Khandelwal and Chakrapani, 2021) in soft contacts (Asnar et al., 2025) and cracks (Bentahar et al., 2020). Nonetheless, it reveals the presence of undesired elements in the concrete's constitution that weaken it, directly affecting its performance. Figure 2.5e shows how the structure softens at different compressive forces at the four different sensor places due to the action of the same transient source. At the majority of the compressive forces, the south side softens less than the north side, except at 2.05D and 2.05C, when the structure experienced more significant loading

rates in the compressive force (from 1.79 MPa - rest state - to 2.05 MPa at the beginning of the experiment, and from 1.74 MPa to 2.05 MPa towards the end of the experiment). The following behaviour can be noted on the South side:

- The smaller the compression of the structure, the higher the velocity drops: At consistent loading rates in the compressive force, the SL and SR sides soften more and equally when the structure is at the lowest compressive force (1.43 MPa).
- Softening occurs at varying magnitudes under the same compressive forces in SL and SR sides: This observation, together with differences in the acoustoelastic effect while decompressing and compressing, suggests that the elastic properties of concrete evolve differently in compressive and extensional deformation as also observed in different composite materials (Jones, 1977) (differences in the stress-strain relationship of concrete during loading and unloading as empirically obtained in (Korolev et al., 2021)), resulting in different concrete's damage kinematics in compression and extension. This phenomenon is further addressed by physical models that include mathematical representation of microscopic defects like the opening and closing of microcracks (Niu et al., 2024) oriented in preferred directions with respect to the maximum experienced tension or compression (i.e. Damage Rehology model proposed by Lyakhovsky, Ben-Zion, and Agnon, 1997 (Lyakhovsky et al., 1997)) to model the temporal dependence of material's elastic properties.
- In general, there is no significant difference in the results obtained in SL and SR, so the structure softens rather homogeneously on the south span through the experiment.

The following behaviour can be noted on the North side:

- In general, the behaviour is complex.
- While decompressing, the structure softens in random magnitudes but significantly more, up to twice, compared to the south span, i.e. 1.89D, 1.74D, and 1.58D. High magnitudes of velocity drops are observed in damaged concrete samples (Bentahar et al., 2020).
- Similar softening is observed at the lowest compressive force on the NL and NR (1.43D).
- The structure follows a similar softening trend while compressing in the NL and NR.

Up to this point, qualitatively, we can conclude that the velocity drops and the subsequent relaxation processes seem to be affected not only by the integrity of the material or its damage level but also by the confining forces to which it is subjected, the direction of the deformation, and its loading/unloading rate in specimens in field conditions.

Figure 2.6g shows the maximum and minimum velocity drop magnitudes observed while decompressing (dots) and compressing (crosses) at the four locations when the loading rates on the bridge were consistent (from 1.89D to 1.74C). The difference between each maximum and minimum velocity drop pair is referred to as variability. Such variability is larger in the north span and, to some extent, remains similar in the south

span while decompressing than compressing. The softening magnitude variability between different compressed states seems to bring information about the material's integrity. To understand the physical nature of the temporal changes of wave velocity, we analyse the remanent decorrelation of dv/v estimations. Remanent decorrelation (1-CCC) (Tremblay et al., 2010), as observed in Figure 2.5a lower part, evolves similarly to the dv/v, that means, high decorrelation at the moment of the velocity drops that decreases over time during the relaxation process. Although remanent decorrelation (distortion) can be associated with the rate of conversion between different wave modes i.e. between the dilatational P- and shear S-waves (Lobkis and Weaver, 2003), and to changes in the bulk properties of the aggregates (which would require more energy than the induced by the vertical impulsive source.), the most plausible reason corresponds to a feeble change in the scattering properties of the concrete structure, for instance, a small rearrangement of the contacts between grains (Tremblay et al., 2010).

We used the scattered wavefield to analyse the temporal changes in elastic properties; this part of the wavetrain is assumed to be mainly conformed by shear waves travelling at random ray paths, allowing the measurements to be sensitive to changes occurring in the structure in multiple directions, i.e. 1. the compressive force parallel to the direction of propagation, and 2. the vertical impulsive source perpendicular to the direction of propagation. The softening process is then linked to the sudden creation of scatters randomly distributed and oriented (i.e. an increment in the void space by opening preexisting microcracks); those scatters, through time, slowly evolve back by the response of the constituents of the reinforced concrete in a type of self-mechanical rehardening (hardening by bacterial reactions and chemical hardening, e.g., crack sealing by means of cement hydration and continuous bulk hydration, operates at different time scales (John and Lothenbach, 2023; Ferrara et al., 2018)) that suggests a closing process of such void space as the transient perturbation vanishes, allowing a gradual concrete's strength improvement. The time the structure takes to recover might be related to the scatters density and the velocity at which such scatters get closed; given that the recovery is not happening instantaneously, such scatters require a transient process that delays the closing (i.e. frictional sliding along microcracks' lips, where shear deformation is the driving force, or crack closing by indentation creep (Choi et al., 2012)). Since the energy is still transmitted through the scatters, it suggests the crack faces are close enough or in contact at several places in the structure to allow wave propagation at this specific frequency band (crack width of less than 0.1 mm (Kaur et al., 2019)). Experiments on anisotropy of nonlinear elastic effects in field-condition concrete structures are needed to analyse microcracks/crack networks' orientation.

The high-density presence of such microstructures promotes changes in the ultimate material strength and, therefore, the crack propagation process at larger scales, affecting concrete's performance and lifespan. Identification of such elements seems advantageous since micro imperfections are the prelude to actual failure, opening the possibility of damage identification in an early stage. Traditional wavefield-based NDT methodologies that evaluate instantaneous elastic properties excel in damage assessment but are blind to detecting such prelude.

## 2.5.4 Cross-plots

• Figure 2.6c P-wave velocity - Acoustoelastic effect. The four locations of the bridge are distributed in three main groups in this plot: 1) high P-wave velocities and low

acoustoelastic effect. Qualitatively, this space refers to high uniformity in concrete that changes less under the action of compressive forces (less density of tensile microstructures), where SL and SR sides are grouped. 2) low P-wave velocities and high acoustoelastic effect, opposite to the first group, this space suggests less uniformity in concrete where the elastic properties change more when external solicitations are applied (high density of tensile microstructures), where the NL side is. 3) low p-wave velocities and low acoustoelastic effect imply low concrete uniformity that does not change considerably on the action of external forces. This cross-plot complements the discussion in 2.5.2, which suggests a low density of soft microstructures or poorly activated soft microstructures on the NR side due to interlocking or rough surface effects. A high density of heterogeneities with low mechanical strength characterises this site. The nature of such heterogeneities ranges from different types of aggregates to soft microstructures, showing low dynamic response to compression due to a low level of void space or complex interactions at void space interfaces.

- Figure 2.6e P-wave velocity Velocity drop. In this plot, two groups are distinguished: 1) the south span shows high P-wave velocities with low variability in the velocity drops, concluding on a high uniformity in concrete with low density of microstructures with transient response, and 2) the north span exhibits low P-wave velocities with high variability and higher magnitudes of velocity drops, explained by low concrete uniformity and high density of microstructures with transient response.
- Figure 2.6f Velocity drop Acoustoelastic effect. As the velocity drops indicate the presence of microstructures with transient responses, and the AEE is sensitive to microstructures with tensile components, the locations with high AEE and high variability and magnitude of velocity drops, such as the NL side, suggest to be the location with a high density of microstructural elements that soften more the bridge when external solicitations (static and dynamic) in different directions are applied.

Visual inspections conducted in the structure (Liao et al., 2021) identified the presence of flexural cracks on the mid-bottom part of both bridge spans. The quantitative differences observed in this experiment at the four locations on the bridge may be attributed to the effects of external cracks and the varying number densities of hidden microstructures with tensile and transient features, as well as different dynamic evolutions as shown in Figure 2.7.

The CWI sensitivity inherently adds drawbacks. The advantage of Wave Interferometry to identify small changes in the elastic properties of materials makes it susceptible to recording not only the effect of mechanical stress but also thermal (air temperature, sunlight, freezing and thawing) and chemical stresses (hydrolysis, condensation), that, inevitably, any outdoor placed concrete structure is subjected to. More studies are needed to investigate the implications of environmental effects in dv/v measurements to discern thermal or chemical factors from mechanical ones as damage sources in large-scale field-condition concrete structures.

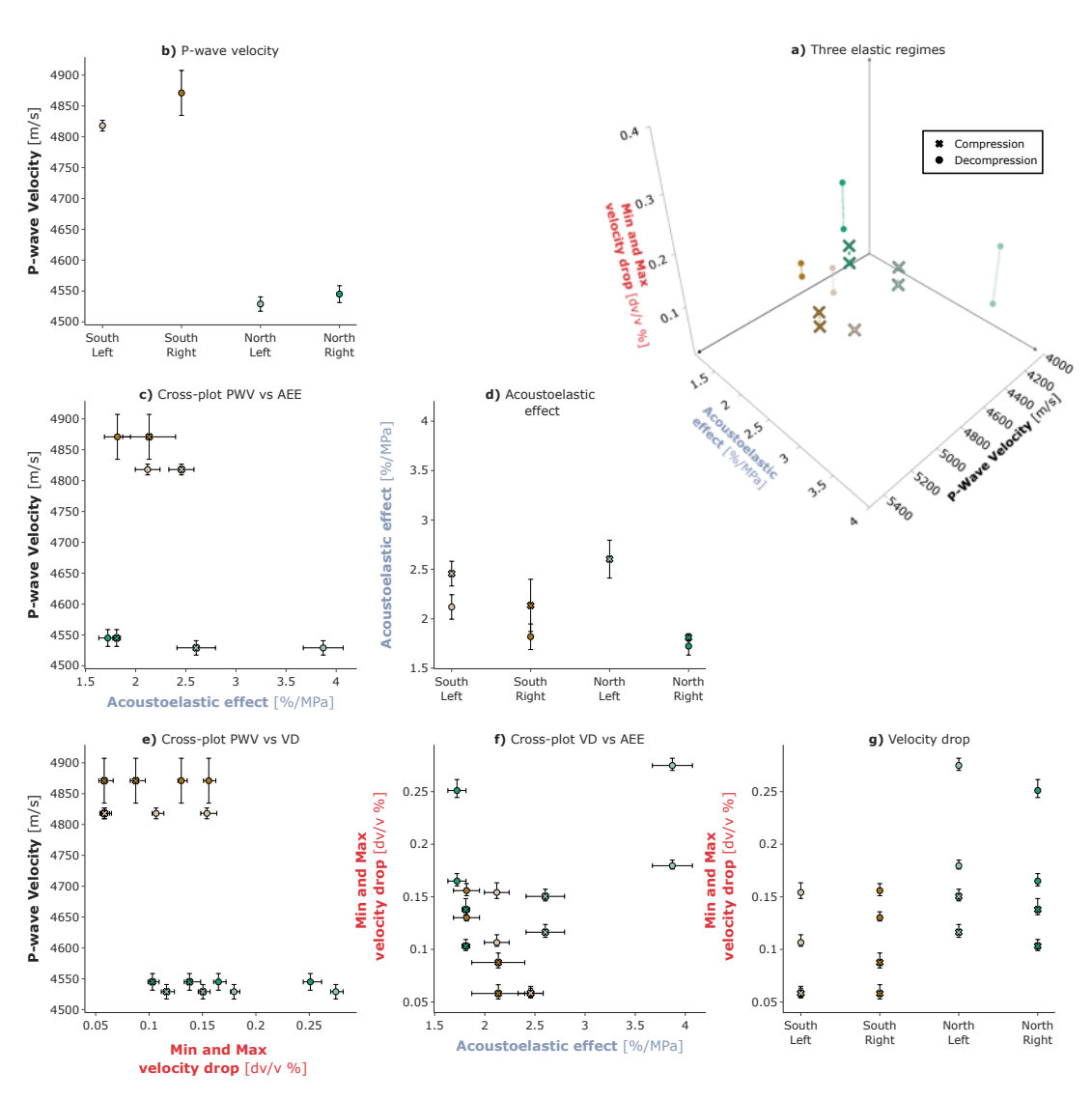


**Figure 2.6**: The cooperative description of the bridge. a) The Linear, Classical Nonlinear, and Nonclassical Nonlinear elastic behaviours on the 3-D plot. b) The P-wave velocity, d) the acoustoelastic effect, and g) the Minimum and Maximum velocity drops measured at the four locations on the bridge. c) The cross-plot P-wave velocity vs Acouestoelastic effect. e) The cross-plot P-wave velocity vs Velocity drops. f) The cross-plot Velocity drops vs Acoustoelastic effect.

## 2.6 Conclusion

In this work, we describe the strength of four locations in a field-conditioned concrete structure in terms of its instantaneous and nonlinear elastic properties, including classical and nonclassical ones. With a cooperative description of the three elastic regimes, we suggest how different number densities of soft microstructures with tensile and transient components influence the evolution of concrete's dynamic elastic properties. We propose relative integrity levels and densities of soft microstructures that exhibit different dynamic behaviours for the four locations of the bridge, highlighting the advantages of performing cooperative analysis over single elastic feature descriptions.

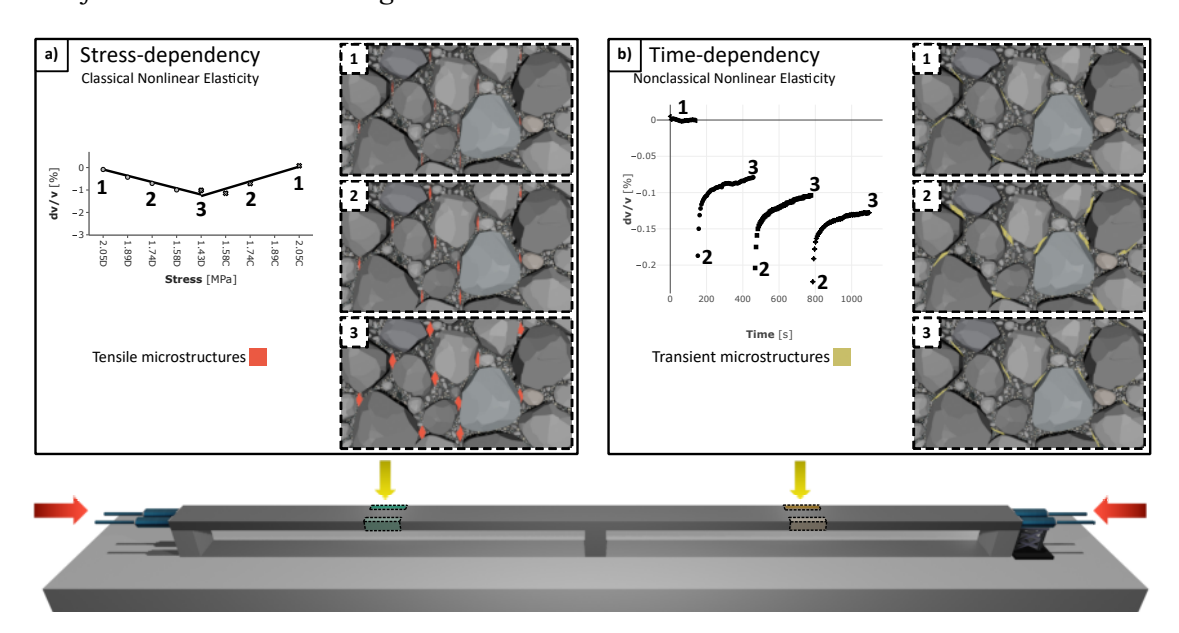


Figure 2.7: The conceptual model of the bridge: a) The stress-dependent relative velocity changes: 1) Preexisting tensile microstructures, in red, 2) 3)soften the bridge as the compressive force decreases and strengthen it as the compressive force increases. b) The time-dependent relative velocity changes: 1) In yellow, preexisting transient microstructures in a steady state produce no relative velocity changes. 2) transient microstructures are excited by the action of the vertical impulsive sources, and the bridge softens, and 3) the recovery process when the transient microstructures tend to return to 1) on logarithmic time scales.

Wave interferometry is a steady and sensitive monitoring tool for static and dynamic mechanical changes as a function of stress and time in field-conditioned concrete structures.

Stress-dependent parameters, such as AEE, provide meaningful information on concrete composition and can be easily related to high-order elastic constants. However, they require specific setups that control the stress/strain measurements in terms of direction and magnitude on the tested civil structure.

A vertical impulsive source, e.g., a hammer hit or a free-falling weight, is suitable for investigating the time-dependent evolution of elastic properties by means of the Slow Dynamics phenomenon in field conditions and their relationship with the dynamics of microstructures. Slow Dynamics, specifically logarithmic recovery processes, are highly influenced by the integrity level of the material, the confining forces, the direction of deformation, and the preceding loading rates. Despite this, the softening processes behave systematically and provide information on concrete's microstructural elements.

We contribute to expanding the investigations required to formalise the developed knowledge in lab conditions in the context of rock mechanics and rock physics into formal damage assessment practices for concrete structures sensitive to imperfections at the microstructural scale.

# 3

## Stress-dependent Slow Dynamics in concrete structure under field conditions

This chapter is currently in preparation for publication with Christoph Sens-Schönfelder, Ernst Niederleithinger, and Celine Hadziioannou, and presents two main scientific contributions: I) The development of an analytical model to simulate the sequential elastic softening and relaxation processes (a sequence of nonclassical nonlinear elastic effects) observed in the experiment, where a concrete structure was subjected to varying levels of compressive force. The model successfully reproduces the relative velocity changes reported in Chapter 2, independent of both the concrete's integrity level and the applied compressive force, using four key variables related to the nonlinear elastic effects. II) The estimation of energy content associated with the softening and relaxation processes in concrete, for both high- and low-integrity conditions. These estimations contribute to better characterising the nature of the soft microstructures present in the concrete structure discussed in Chapter 2.

## **Contents**

3.1	Introduction		
3.2	Time-dependent dv/v observations		
	3.2.1	dv/v Measurements - The components	30
	3.2.2	Models for Slow Dynamics in complex solids	32
	3.2.3	The analytical model	35
3.3	Data Inversion		37
	3.3.1	Prior information in data space	37
	3.3.2	Prior information in model space	37
	3.3.3	Solving the inverse problem	38
3.4	Results		
	3.4.1	The relationship between the analytical model parameters	
		and the observed data	39
	3.4.2	The analysis of $\alpha$ , the linear effect	42
	3.4.3	The analysis of $\beta$ , the velocity drops	44

3 5		Time-dependent elastic and energy dissipation changes ssion	
3.3			
	3.5.1	Possible physical mechanisms for slow dynamics in concrete	4
	3.5.2	Relationship between $\alpha$ and $\beta$ with structural effects	4
3.6	Concl	usions	4

## 3.1 Introduction

Understanding every elastic process that occurs in concrete before it fails must be salient to structural health monitoring. Material failure is thought to be a process resulting from stress transfer through internal deformation (Asnar et al., 2025). Heterogeneous materials project this transfer via the time-dependency of elastic properties, i.e., hysteresis and Slow dynamics. Slow dynamics may well prove to be an indicator and precursor to brittle deformation and fracture, and may also helps us learn about processes that happen well before fracture, a regime that has not yet been fully studied (TenCate, 2011).

Although this time-dependent process has been arguably widely studied in concrete, lab experiments report the presence of slow dynamics in concrete and how this process performs differently when the heterogeneity level of the sample is increased by the action of micro imperfections.

To translate damage-sensitive phenomena like Slow Dynamics into a set of practices for damage assessment, it needs to be studied at the data analysis and experimental levels under non-highly controlled environments (close to daily applicability conditions)

In the previous chapter, the stress-dependent dv/v was characterised by using an analytical linear model that represents the Acoustoelastic Effect. On the other hand, the time-dependent dv/v effect was quantified observationally. This was done by directly measuring velocity drops within 15  $\pm$  5 seconds after the action of a Vertical Impulsive Source (VIS), which triggered relaxation processes recorded over a 5-minute period

This chapter deals with the study time-dependent dv/v measurements from the analytical point of view. To this end, an analytical expression that models the evolution of dv/v (or any other proxy to elastic properties) in concrete under the action of more than one external perturbation of different kinematic natures is required. The model must describe elastic changes in solids due to the effect of dynamic transient sources superposed to static changes in the body. To the present time, there is no analytical expression that satisfies the needs of this study.

The first part of this chapter is dedicated to describing the building process of this model. First, the elements of this analytical expression are identified on the dv/v observations. Then, assuming a linear combination of all such elements, an analytical expression that reproduces the evolution of dv/v over time is derived. This expression captures the effect of the three VISs hitting the structure at different times while being compressed at different force levels by using three variables related to the qualitative changes of the dv/v recordings. This expression allows a quantitative description of the measurements while considering the whole extent of the dataset and not only information recorded at specific times during the process.

The second part of this chapter is dedicated to the inversion process. It details the data inversion process employed, the steps, considerations, and hyperparametrisation used to marry the model developed in the previous section with the recorded data.

In the third part, the results are reported and discussed. Here, the performance of the model is evaluated in two different forms: I) the harmonicity model-data, which discusses the dependency of the measurements on the model variables, and II) the nonuniqueness. Aside from evaluating the model, this section discusses the results obtained in the data inversion process for the recordings of the four different places. This section establishes connections between the integrity level of concrete and the action of the external solicitations with the data inversion results, finding plausible physical processes that explain such a connection.

Finally, a subsection is dedicated to commenting on the techniques and methods, details to be considered for future experiments in field-conditioned concrete structures, and the similarities of the results obtained in this section with the observational results estimated in the previous chapter.

## 3.2 Time-dependent dv/v observations

The time-dependent dv/v measurements shown in Chapter 2 are considered. Figure 3.1 plots the dv/v recordings (recorded every five seconds but resampled to have one dv/v measurement per second) of the four locations of the bridge; they all have different relative integrity levels under eight compressive forces, which means 32 datasets. In this figure, the cross-correlation coefficients that result from the stretching process are translated into dv/v variance using Wever's mathematical expression (Weaver et al., 2011):

$$rms(\epsilon) = \frac{\sqrt{1 - CC^2}}{2CC} \sqrt{\frac{6\sqrt{\frac{\pi}{2}}T}{\omega_C^2(t_2^3 - t_1^3)}}$$
(3.1)

Here, CC is the maximal correlation coefficient from the stretching method, T represents the inverse of the frequency bandwidth,  $\omega_C$  is the centre frequency and  $t_1$  and  $t_2$  are the lower and upper limits for the time window of the coda wave which was used for stretching. This expression allows the estimation of the error bars of each dv/v point. Broadly speaking, this error tends to be higher on dv/v estimations close to the instant of the action of each VIS. It is possible to note that the magnitude of the relative velocity changes tends to vary depending on the integrity level of concrete and the compressive force levels, not to mention the shape of the relaxation processes. Still, they all share similar components that promote using a standard model to numerically evaluate each of the 32 datasets. The aim is to find a mathematical expression that can reproduce the whole extent of the data.

## 3.2.1 dv/v Measurements - The components

To dive deep into the analysis of the standard components in all datasets, figure 3.2 is presented. Figure 3.2 a) plots the dataset recorded at a compressive force level of 280 kN. The vertical axis represents the relative dv/v, and the horizontal axis represents the time in seconds. This representative dataset can be broken apart into the following features:

1. Steady-state (from time t=0 sec. to t=150 sec.): This corresponds to the information recorded after the change in the compressive force and before the action of the first VIS. This part of the dataset is characterised by almost no changes in dv/v, yet subtle dv/v changes are observed with dv/v errors close to

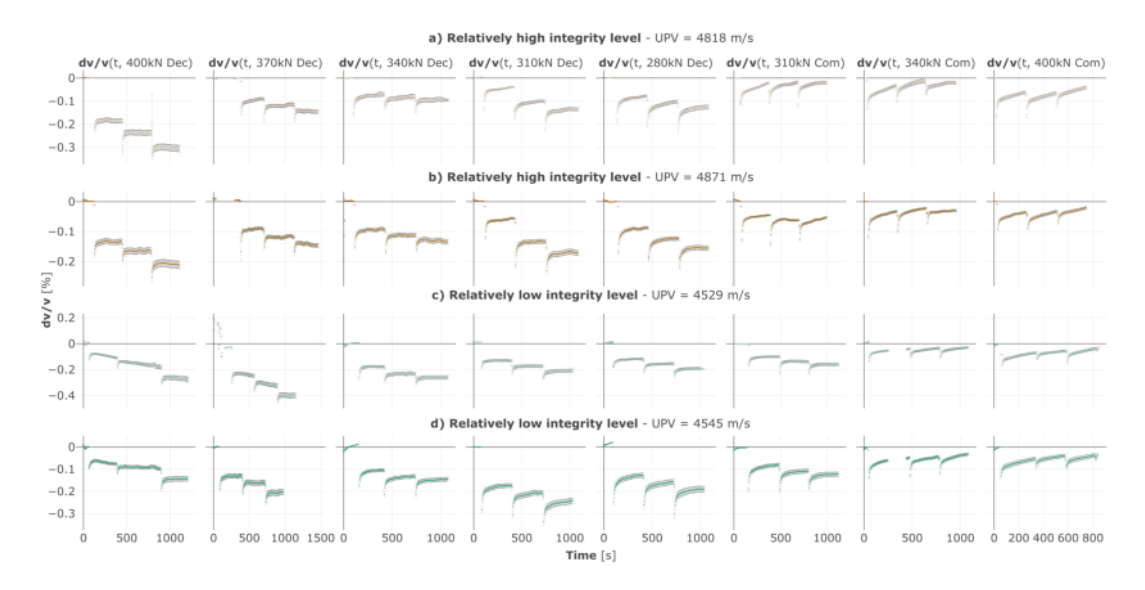


Figure 3.1: Datasets recorded at the four locations of the bridge at eight different compressive force levels. a) Plots of the eight datasets recorded on the south-left side. This side is categorised as concrete with a relatively high integrity level due to the high ultrasound pulse velocity values. b) Plots of the eight datasets recorded on the south-right side (a side with a relatively high integrity level). c) Plots of the eight datasets recorded on the north-left side. This side is categorised as concrete with a relatively low integrity level due to the low ultrasound pulse velocity values. d) Plots of the eight datasets recorded on the north-right side (a side with a relatively low integrity level).

zero. Considering that first-order thermal effects were removed from the data, those subtle changes might be dominantly related to time-dependent mechanical stress induced by the change in the compressive force.

- 2. The first velocity drop (at time t=151 sec.): This is the almost instantaneous reaction of the structure to the first VIS. This reaction is characterised by a decrement in the wave propagation velocity (negative dv/v). The dv/v error tends to increase.
- 3. The upward time-dependent curve (from time t = 151 sec. to t = 466 sec.): the aftereffect of the first velocity drop that develops a recovery over the long term in a seemingly self-stiffening process.

Features 2 and 3 are processes reminiscent of the two components of Slow dynamics defined in Chapter 2: the softening and the recovery process. This set of features is observed two more times along the dv/v recordings due to the remaining two VISs.

Qualitatively, it is possible to decompose the time-dependent dv/v observations into the elements shown in Figure 3.2b I) Linear effect, II) three relaxation processes, III) the remaining effects of the first and second VISs. The analytical representation of each component and their linear combination leads to the sought analytical expression.

The components listed in the previous section have intuitive mathematical representations. However, the SD phenomenon can be modelled in several ways. Before developing the analytical expression to model the observed dv/v, it is opportune to draw a general landscape of the existing models that reproduce SD and the physical meaning they pursue.

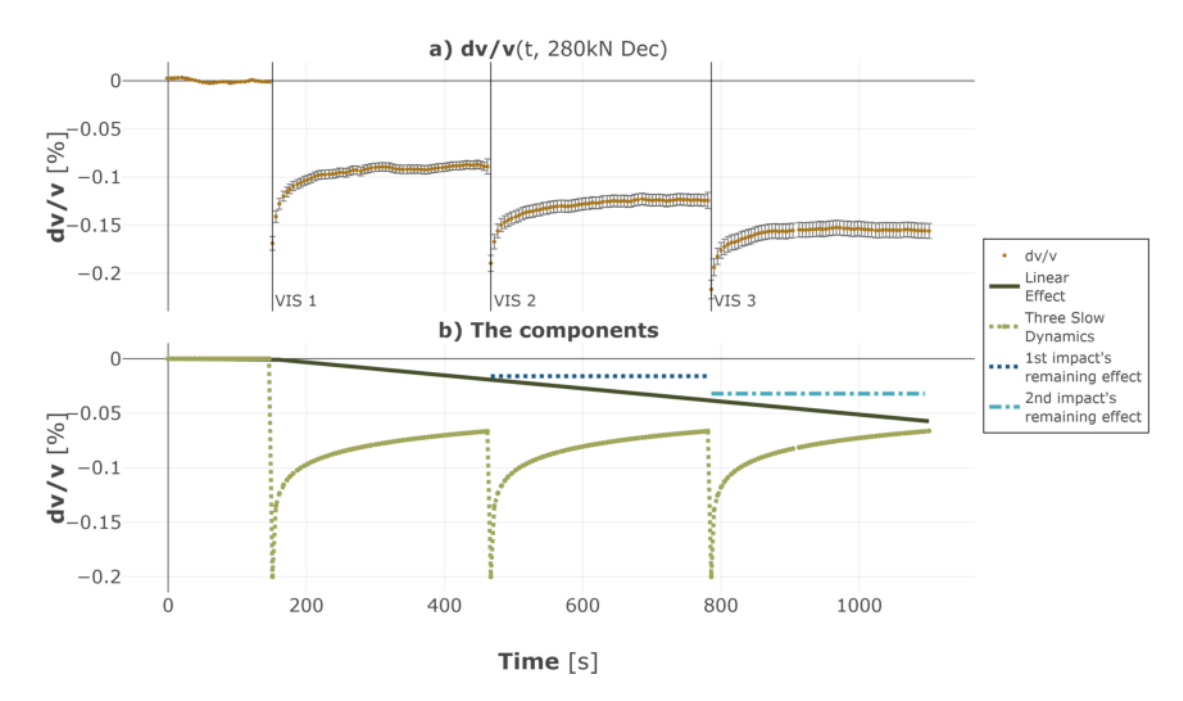


**Figure 3.2:** Representation of the components present on each of the time-dependent dv/v datasets. a) the dv/v dataset recorded at a compressive force level of 280kN, with the times when the VISs were activated (VIS 1, VIS 2, and VIS 3) b) the elements that compose the dataset. The linear component, the three relaxation processes, and the remaining effects of the first and second VISs.

This overview of the models is divided into two sections. First, those models strongly rooted in principles of solid mechanics and physics that seek to add different damage kinematics and healing mechanisms to the stress-strain relationship to reproduce the time-dependent evolution of elastic moduli (as SD is). Second, practical models that reproduce the SD process using phenomenological variables instead of elastic properties intrinsic to the material.

## 3.2.2 Models for Slow Dynamics in complex solids

The softening and recovery processes have been observed in different materials at different scales. This makes it complicated to come up with a universal theory that unifies and explains such material degradation (that can be interpreted as damage, referring to the degradation of the elastic properties of the material) and long-term recovery in terms of intrinsic material's DEP.

There are a handful of theoretical models in the physics and rock mechanics literature with the potential for modelling slow dynamics. Some theories and models describe time-dependent processes as a function of the material's physical properties or phenomenological variables (i.e., strain rate, damage variables, contact numbers, etc.). Some models are categorised depending on the attributed nature of the nonlinear elastic behaviour:

• Internal variable models: the functionality of these models depends on using state variables that describe the macroscopic scale via microstructural elements (such as dislocations, voids or microcracks), whose state can change over time.

- The use of the Preisach–Mayergoyz (PM) spaces: The fundamental premise of this approach is that the macroscopic elastic behaviour of geomaterials (e.g. rocks) is due primarily to a large number of mesoscopic structural features. Those features are elastic elements defined within the PM space framework. This is a density space that contains mesoscopic structural features. Those features describe the elastic state of the system at any given time (the so-called state variables)
  - \* The model of Hysteretic Mesoscopic Units (HMU) (Guyer et al., 1995): The density of HMU in the PM space serves to describe stress-strain relationships observed in complex pressure protocols. However, there are open questions about the nature of the structural elements of the PM space.
  - \* Thermally activated Random Transitions (Scalerandi et al., 2003): This model combines the usefulness of HMU with a two-value state variable r to include thermally activated random transitions between the HMU units. This model simulated nonclassical nonlinear effects in quasi-static and resonant bar experiments. Such predictions are merely qualitative since the value of certain parameters is not known.
- The dependence of softening on a scalar variable g
  - \* Soft-Ratchet Model (Vakhnenko et al., 2005): The functionality of this phenomenological model is based on two subsystems: I) Subsystem of Longitudinal displacements and II) Subsystem of ruptured cohesive bonds, where *g* parametrises defect concentrations. While insightful, it is one-dimensional and lacks thermodynamic admissibility, limiting its applicability.
  - \* Distributed damage, faulting, and friction (Lyakhovsky, Vladimir and Ben-Zion, Yehuda and Agnon, Amotz, 1997): This rheological model accounts for elastic deformation, viscous relaxation, and evolution of damage (softening and recovery processes). This thermally consistent model defines the *free energy* of the solid as a function of the macroscopic temperature, the strain tensor, and a nondimensional damage state variable  $\alpha$  that is conceptually comparable with g. They provide a practical version of the general formulation to model the evolution of damage as a function of the critical deformation and the rate of damage evolution. Such variables are hard to constrain for practical applications.
  - \* Internal-Variable Model for Slow Dynamics (Berjamin et al., 2017): This model introduces a scalar internal variable g to describe material softening and recovery. It incorporates a relaxation time to capture slow dynamics and is thermodynamically admissible. The model reproduces key features like softening, hysteresis, and recovery in uniaxial and finite-strain contexts. There is no clarity on the physical functionality of the internal variable g in this model (Niu et al., 2024).
  - \* Murnaghan Hyperelasticity with Slow Dynamics (Harold Berjamin et al., 2019): This model combines Murnaghan hyperelasticity (which does not account for the log-time relaxation of the material) with a scalar internal variable to account for softening. It uses a nonlinear hyperbolic

system of balance laws to describe wave propagation and softening in damaged media.

- Interactions in bonds and grain contact systems: A component that differentiates these types of models from the scalar-variable type is the use of friction laws on processes between the contact surfaces that evolve as they interact over time.
  - Friction and contact aging in rocks (Sens-Schönfelder et al., 2019): This model qualitatively describes dynamic softening, hysteresis, complex elastic behaviours observed in acoustic tests, and slow dynamics. In this model, frictional interfaces contribute to the macroscopic modulus as the number of broken connections across an interface normalised for the total number of potential connections. The nature of these connections ranges from capillary bridges and chemical bonds to van der Waals forces and adhesive contacts.
  - Friction in unconforming grain contacts as a mechanism for tensorial stress-strain hysteresis (Aleshin and Van Den Abeele, 2007): Here, the authors attribute the slow relaxation to the mechanics and statistics of internal microcontacts, noting that the slow increase of the number of contacts during relaxation results in time-dependent modulus recovery.
- Unconsolidated granular materials
  - Granular materials with shear-transformation-zone theory (Lieou et al., 2017): It is based on the idea that plasticity is attributed to the change of local contacts and rearrangement of grains at loose spots known as shear-transformation-zone, and that one can describe the density of these sites using a structural, effective temperature termed the compactivity.
- Adsorption of fluid at the contacts between grains.
  - Mechanistic diffusion model for slow dynamic behaviour in materials (Bittner and Popovics, 2021): The authors suggest a model based on coupled mechanical and diffusional processes. The physical foundation of the model lies in diffusion-driven moisture migration nearby the minuscule regions surrounding granular contact points within a cracked solid.

Although the models above are highly loaded with physical constraints and reproduce nonlinear wave propagation features like the production of copious harmonics, and complex time-dependent behaviours like elastic memory, softening and slow recovery, they require many additional parameters to represent such elastic behaviour.

In contrast, few consider the quantitative properties of the relaxation function itself (the magnitude of the velocity drop and time span of the relaxation process).

1. Constant Q model (Kjartansson, 1979): Although this model was suggested to account for attenuation, the model uses a relaxation function that is shaped depending on Q values. Such relaxation function is fully parametrised by two parameters: I) the quality factor of the material Q that is independent of frequency, and II) the reference modulus  $M_0$  at an arbitrary reference time  $t_0$ .

$$\Psi(t) = \frac{M_0}{\Gamma(1 - 2\gamma)} \left(\frac{t}{t_0}\right)^{-2\gamma} t > 0$$

$$\Psi(t) = 0$$
(3.2)

where  $\gamma = \frac{1}{\pi} \tan^{-1} \frac{1}{Q} \approx \frac{1}{\pi Q}$ , and  $\Gamma$  is the gamma function which in all cases of elasticity in solids has a value close to unity.

2. Relaxation time spectrum (Shokouhi, Rivière, Guyer, et al., 2017): Here, the relaxation function is assumed to be able to be represented as a sum of discrete exponential decays, each having an amplitude  $A_n$  and time constant  $\tau_n$ .

$$\zeta(t) = \sum_{n=0}^{mxN} A_n e^{\frac{-t}{\tau_n}}, \ A_n \ge 0$$
 (3.3)

The result of this model is a set of amplitudes of each exponential decay component that conform to the relaxation process.

3. The superposition of relaxation processes (Snieder et al., 2017): This approach suggests describing the relaxation process as a superposition of decaying exponentials (each with their own relaxation time  $\tau$ ) that has log-time behaviour but converges to zero for long times and is finite for t = 0. The relaxation function depends on two parameters: the minimum and maximum relaxation time,  $\tau_{min}$  and  $\tau_{max}$ , respectively.

$$R(t) = \int_{\tau_{min}}^{\tau_{max}} \frac{1}{\tau} e^{-\frac{t}{\tau}} d\tau \text{ for } t > 0$$
(3.4)

This function, in essence, is easily parameterisable since it requires no previous knowledge of the elastic properties of the media. Although it is dimensionless, it can be used to describe time-dependent velocity changes using the following expression:

$$v(t) = v_0 + \delta v \frac{R(t)}{R(0)} \tag{3.5}$$

with v(t) the relaxation of velocity changes over time,  $v_0$  the initial velocity changes (steady state),  $\delta v$  the maximum velocity drop observed in the data, and R(0) a normalisation factor (the relaxation function at time t=0). The practicality of this model makes it the perfect candidate to test its performance with measurements recorded in out-of-lab condition experiments.

## 3.2.3 The analytical model

Building upon the early discussion on the elements of the measurements and having found the model suitable for reproducing SD, it is opportune to proceed with assembling them into a unified mathematical expression. Such elements are I) Linear effect, II) three relaxation processes, III) the remaining effects of the first and second VISs, Figure 3.2c, and can be represented mathematically as follows:

I The linear effect: The nature of this effect is complicated to depict by only using temporal dv/v changes. However, it can be speculated that this effect is related to the non-instantaneous component of the compressive force change. This phenomenon can be represented with a linear function, whose intersection is fixed to the instant of the action of the first VIS, and the slope  $\alpha$  is to be sought:

$$v_1(t,\sigma) = \alpha \Delta v(t) \tag{3.6}$$

II The three softening and relaxation processes (VIS 1, VIS 2, and VIS 3 in Figure 3.2a): As discussed, the model of superposition of relaxation processes (Snieder et al., 2017) is used for this investigation to reproduce each of these three elements numerically in our measurements. This model is used due to efficiency matters since it describes such a complex process as a function of three parameters, that is, the velocity drop (or softening)  $\beta$ , the point in time where the relaxation starts (the minimum time scale)  $\tau_{min}$ , and the point in time where the relaxation is considered to approach to its end (the maximum time scale)  $\tau_{max}$ .

$$v_2(t,\sigma) = v_0 + \beta \frac{R(t)}{R(0)}, R(t) = \int_{\tau_{min}}^{\tau_{max}} \frac{1}{\tau} \exp^{-t/\tau} d\tau.$$
 (3.7)

Recording information on field conditions has inherent limitations. This includes the low accuracy of measuring the minimum relaxation time scale  $\tau_{min}$ , which is limited by the sampling period of the measurements, and the limited execution time to record the maximum relaxation time scale  $\tau_{max}$ . The value used for the minimum time scales is t = 0.01 seconds on the know that there is no sensitivity to time scales significantly shorter than the sampling interval (Asnar et al., 2025), and the maximum timescale as t = 30000 s. This value resulted from performing individual inversion on each relaxation curve at different  $\tau_{max}$  magnitudes, observing no fitting improvement after 30000 s on all of them. This investigation seeks the velocity drop  $\beta$  that best fits the dv/v measurements of each relaxation process, considering the previous time scale values. One crucial remark in this step is the hypothesis that the three SD processes share similarities and can be modelled by the same model and parameters as observed in Figure 3.2b. Physically, that means each of the three VIS excites the identical microstructures that react at the same timescales with similar magnitudes.

III The remaining effects of the previous VIS: Each relaxation process is recorded over five minutes, but this period is insufficient for the structure to be fully recovered from the preceding VIS. A step function compensates for this effect on the second and third recovery processes (dark blue and light blue functions in Figure 3.2c, respectively). These effects are parametrised by the amplitude of the step functions  $\gamma$  and  $\delta$ , referred to as the 1st and 2nd impact's remaining effects.

$$v_{3}(t,\sigma) = \begin{cases} 0 & t < VIS_{2} \\ \gamma \Delta v(t) & VIS_{2} \ge t < VIS_{3} \\ 0 & t \ge VIS_{3}, \end{cases}$$

and,

$$v_4(t,\sigma) = \begin{cases} 0 & t < VIS_3 \\ \delta \Delta v(t) & t \ge VIS_3 \end{cases}$$

The analytical expression that models the softening and relaxation processes in concrete at different compressive forces results from the linear combination of the four elements described above as follows:

$$dv/v(t,\sigma) = v_1(t,\sigma) + v_2(t,\sigma) + v_3(t,\sigma) + v_4(t,\sigma)$$
(3.8)

## 3.3 Data Inversion

The primary focus of data inversion is to combine observations and models to get quantitative inferences about properties and processes related to the observed phenomenon. To achieve this, three ingredients are needed: I) observed data  $\mathbf{d}^{\text{obs}}$ , II) the unknown properties to be inferred from the data  $\mathbf{m}$  (model parameters), and III) the physics or theories that relate the model to the observations via a *forward modelling operator*  $\mathbf{G}(\mathbf{m})$ .

There are two approaches to relating observations and data: I) a deterministic approach that seeks to minimise the distance data model and II) a probabilistic approach that looks for the model parameters that are most likely to reproduce the observations. This second approach provides a solution in the form of probability densities, which contain useful information about the relationship between the estimated parameters and the observed data, while also assessing the non-uniqueness of the estimated model. Due to the laid reasons, the probabilistic approach is adopted in this data inversion process.

Solving a probabilistic inverse problem is equivalent to finding a posterior probability density in model space that describes all available information on the model parameters. This posterior information in model space is the result of combining prior information on observed data (data space), model parameters (model space), and the forward modelling theory (Fichtner, 2021).

## 3.3.1 Prior information in data space

Under favourable conditions, the data prior may be derived from careful statistical analyses that allow us to cast the random occurrence of observational errors in the form of the probability density. The prior in data space encodes our probabilistic prior knowledge about the likelihood of observing a specific realisation  $\mathbf{d}^{\text{obs}}$ , given the hypothesis  $\mathbf{m}$  evaluated in the forward modelling operator  $\mathbf{G}$ .

$$\rho\left(\mathbf{d}^{\text{obs}}|\mathbf{m}\right) = \frac{1}{(2\pi)^{\frac{n}{2}}} \frac{1}{\det C_{\mathbf{D}}} e^{-\frac{1}{2}(\mathbf{d} - \mathbf{G}(\mathbf{m}))^{T} C_{\mathbf{D}}^{-1}(\mathbf{d} - \mathbf{G}(\mathbf{m}))},\tag{3.9}$$

with n as the number of model parameters (the dimensions of the model space). The covariance matrix  $C_D$  captures the measurement variances encoding our knowledge about measurement accuracy. With the additional assumption that the measurements of data points are independent of each other and all have the same variance  $\sigma_m^2$ ,  $C_D = diag(\sigma_m^2, ..., \sigma_m^2)$ .

## 3.3.2 Prior information in model space

The prior information in model space exists independently of any observed data and before performing any experiment. It may result from previous experiments or fundamental constraints of physics. Since this is the first time this model has been tested with several datasets, there are no prior constraints. Therefore, his inversion process ascribes equal plausibility to all the proposals (tested values) in the model space M. This assumes a homogeneous distribution that suggests relative ignorance of model parameters. One more constraint on the model parameters for this inversion process is:

$$\int_{M} \rho\left(\mathbf{m}\right) dm = 1 \tag{3.10}$$

With the above two constraints and based on the maximum entropy principle of designing the prior (Good, 1963), the data is assumed to be uniformly distributed in the model space M

## 3.3.3 Solving the inverse problem

Once the prior information in data and model space are cleared, it remains to combine this information to obtain the posterior in model space. This combination can be achieved using Bayes' theorem for probability densities as follows:

$$\rho\left(\mathbf{m}|\mathbf{d}^{\mathbf{obs}}\right) = \frac{\rho\left(\mathbf{d}^{\mathbf{obs}}|\mathbf{m}\right)\rho(\mathbf{m})}{\rho(\mathbf{d}^{\mathbf{obs}})} \tag{3.11}$$

It yields the posterior probability density of the model parameters  $\mathbf{m}$  given some observed data  $\mathbf{d}^{\text{obs}}$ , in terms of the prior in data space,  $\rho\left(\mathbf{d}^{\text{obs}}|\mathbf{m}\right)$ , also named the *likelihood function*, the prior in model space  $\rho(\mathbf{m})$ , and a normalisation factor  $\rho(\mathbf{d}^{\text{obs}})$  named the *evidence*. This parameter scales the posterior, and its numerical value does not affect the relative likelihoods of different models  $\mathbf{m}$ :

$$\rho\left(\mathbf{m}|\mathbf{d}^{\text{obs}}\right) = \frac{\rho\left(\mathbf{d}^{\text{obs}}|\mathbf{m}\right)\rho(\mathbf{m})}{\rho(\mathbf{d}^{\text{obs}})} \propto \rho\left(\mathbf{d}^{\text{obs}}|\mathbf{m}\right)\rho(\mathbf{m}) \tag{3.12}$$

Equations 3.9, 3.10, and 3.11 clearly show that the posterior density can be computed point-wise up to an unknown constant factor.

Bayes' theorem comes with a significant drawback, namely that the posterior cannot usually be computed analytically. That means it is not possible to write down a simple explicit equation that takes some  $\mathbf{m}$  and returns the posterior without significant computations. Instead, for each proposal  $\mathbf{m}$ , the forward problem must be solved: evaluate the likelihood function and then multiply with the prior in model space. This process, which needs to be repeated for all candidate models  $\mathbf{m}$ , is referred to as sampling. Sampling can be a computationally expensive exercise, especially when the forward problem solution is already computationally expensive, and when the model space has a large number of dimensions.

## Sampling method - Metropolis-Hastinings algorithm

MCMC provides a practical way to compute Bayesian inference when exact solutions are intractable or computationally expensive by exploring randomly the model space. MCMC methods like Metropolis-Hastings sampling allow the generation of samples from the posterior distribution without having to calculate the normalising factor  $\rho(\mathbf{d}^{\text{obs}})$  (which is usually difficult to compute since it requires the solution of an integral over the complete model space M, which may have a high dimension). One more advantage of the MCMC sampling methods is:

- The possibility of computing the posterior's means or variances
- The possibility of computing the probabilities of the hypothesis or candidates
- The possibility of making predictions

Once the target distribution is established 3.12, its computation via a random exploration of the model space M is possible by the following transition rule:

$$\mathbf{m}^{\mathbf{i}} = \mathbf{m}^{\mathbf{j}} + \sigma \Delta \mathbf{m}^{\mathbf{j}} \tag{3.13}$$

where  $\sigma$  represents the step length in the model space, and  $\Delta m^j$  the proposed move in the model space with the step length from the current proposal  $m^j$  to the new proposal  $m^i$ . The move to the new proposal is accepted if the metropolis rule is met:

$$A^{i \leftarrow j} = min\left(1, \frac{L^i}{L^j}\right) \tag{3.14}$$

The metropolis rule establishes that the transition from  $\mathbf{m}^{\mathbf{j}}$  to  $\mathbf{m}^{\mathbf{i}}$  is always accepted when the likelihood of the new model  $L^{i}$ , is higher than the likelihood of the current model  $L^{j}$ , then the equation becomes

The parameters used to perform this statistical inversion process are listed in the table 3.1:

Variable	Initial proposals	Step length
α	0.333	0.1
β	-0.00020	0.00005
γ	0.02	0.000005
delta	0.04	0.000005

Table 3.1: Initial proposals and step lengths used in the MCMC Metropolis-Hastings algorithm

## 3.4 Results

In this section, the performance of the model and the results of the data inversion process are discussed. First, the distributions of the individual parameters (1-D Marginals) are analysed in order to assess the reliability and uncertainty of the parameters estimated with the data inversion process.

An analysis of the results is then presented, focusing on the behaviour of the parameters under different compressive forces and their connection to concrete with both low and high integrity levels.

## 3.4.1 The relationship between the analytical model parameters and the observed data

As mentioned at the beginning of this section, probabilistic inversion provides information about the uncertainty of the suggested model and the way each model variable  $\mathbf{m}$  relates to the measured data  $\mathbf{d}^{\text{obs}}$  via the 1-D marginals. The analysis of such marginals results in insights into the harmonicity between the analytical model and the

observed data. The acceptance rate is also estimated to comment on the performance of the algorithm in exploring the model space M.

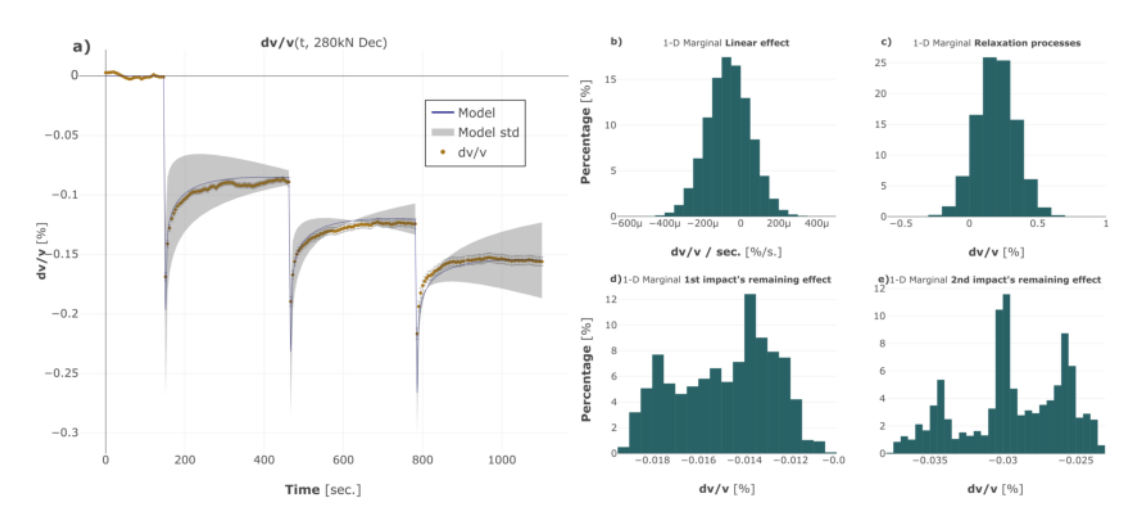


**Figure 3.3:** An example of the data inversion process. a) Results of the data inversion for the dataset recorded at 280 kN in the south-right side. b) The histogram of the accepted proposals for the linear effect, c) the amplitude of the three relaxation processes, c) the 1st impact's remaining effect that acts on the second relaxation process, and d) the 2nd impact's remaining effect that acts on the third relaxation process.

• Histogram: Figure 3.3 plots the histograms of the accepted proposals in the inversion process as a representative case for the 32 data inversion processes (more examples can be found in A.2). The linear effect and the velocity drop exhibit histograms with clear Gaussian distributions with proposals with a high acceptance percentage, meaning two things: I) the most likely values of the parameters are the mean of such distributions, and II) the uncertainty of such estimations is symmetric around the means and can be quantified by the standard deviations of each distribution. On the other hand, the histograms of the remaining effects show different features. Instead, multimodal distributions characterise their histograms. Multimodal distributions complicate finding a unique and clear value for the parameters since such distributions show more than one representative peak. The uncertainty is non-symmetric and cannot be quantified with precision. Here, three possible circumstances that led to multimodal distributions are debated: I) The Metropolis-Hastings method is not able to sample the model space properly enough. Metropolis-Hastings is an algorithm that explores the model space dependent on a constant step size, meaning the successive proposal is not independent of the previous one, which in turn limits the sampled space. The acceptance rate is a criterion that can be used to evaluate if the model space was, to some extent, appropriately sampled. Figure 3.4 shows acceptance rates around 0.5-0.6 in most cases, which indicates good model space sampling (Fichtner, 2021). II) The model itself is complex or nonlinear (Łatuszyński et al., 2025) and assuming the prior in data and model spaces are normally distributed does not work anymore. As stated, the model is assumed to be a linear combination of linear parameters. Therefore, no explicit non-linearities are embedded in the analytical model. III) The data are complex enough that more than one parameter setting

makes sense. This point questions the relationship between the observations and the model that tries to explain them. While building the analytical model, the remaining effect of the previous relaxation process was modelled using a step function; this function applies a constant effect through time over the current relaxation process, meaning that this remaining effect is static and does not evolve through time. This constraint might not be enough to model such remaining effects mathematically while capturing their physical implications on the data, and it might require more complex mathematical representations to model them. In this case, it is opportune to highlight that the observations depend only weakly on the way the remaining effects are modelled or even observed by the data (a poor relationship of the data with these two model parameters).

• Acceptance rate: The ratio of the total number of proposed samples  $N_S$  to the number of accepted moves  $N_{acc}$  is called *acceptance rate*. A low acceptance rate means that many proposals are tested without actually making the random walker move to a new position, resulting in a model space poorly explored. On the other hand, a high acceptance rate is neither ideal nor desired, and this problem is intimately related to the step size. In this case, when the radii size is small, the new proposal ends up in a position close to the current one, this makes it unlikely that an implausible model is proposed, and therefore, the acceptance rate is high. The price to pay is also a poorly explored model space. A balance between low and high acceptance rates is sought, as observed in Figure 3.4. The inversion processes result in acceptance rates of around 0.5 and 0.7 units except at 340kN D for measurements recorded in the concrete of low integrity. This leads to the conclusion that the model is mostly stable regardless of the integrity level of the concrete and the confining forces.

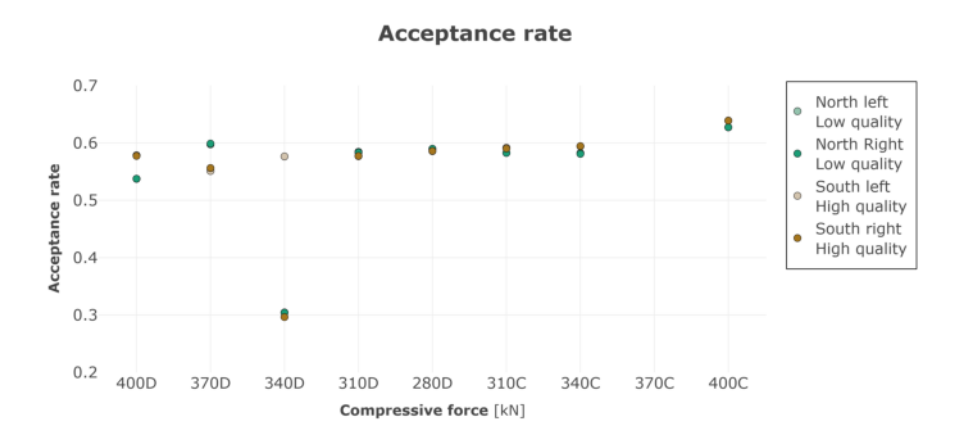


**Figure 3.4**: The acceptance rate estimated on the data inversion processes for north-left, north-right, south-left, and south-right datasets.

The probability inversion process was carried out following standard guidelines, resulting in estimating the model parameters for consecutive Slow Dynamics processes at different compressive force levels occurring in concrete of different integrity levels, and their uncertainty estimations. Considering the acceptance rate and the distributions of the accepted proposals as well-constrained variable indicators, it is concluded that

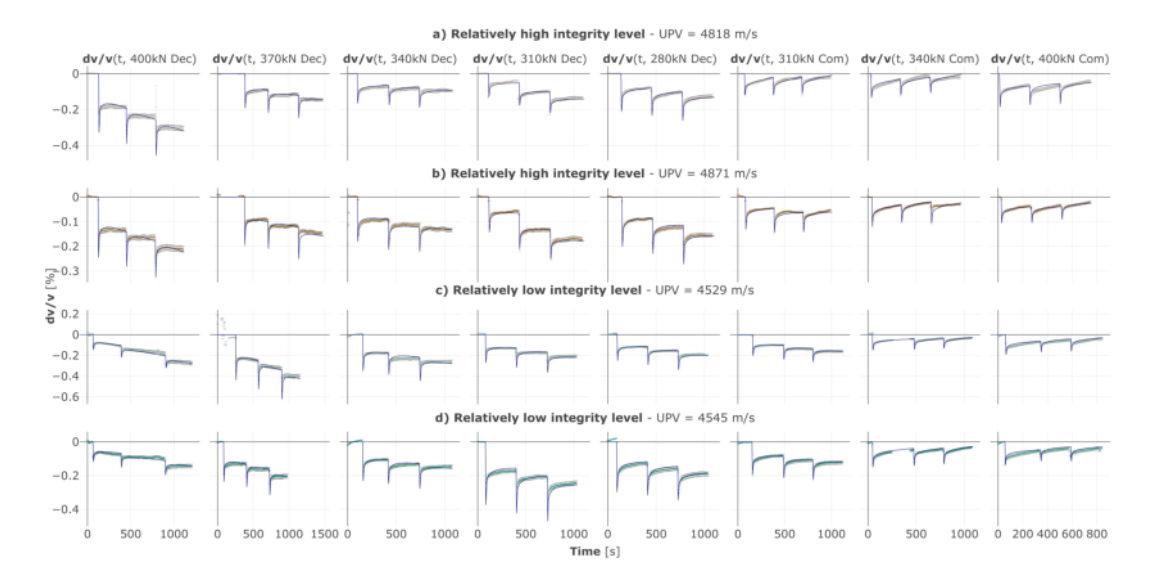


**Figure 3.5:** The performance of the analytical model on reproducing consecutive slow dynamics effects at different compressive force levels,  $dv/v(t,\sigma)$ , on concrete of different integrity levels. a) The observed dvv/v on the south-left side plotted in light brown, and the model is in a continuous dark blue line. b) The observed dvv/v on the south-right side plotted in dark brown, and the model is in a continuous dark blue line. c) The observed dvv/v on the north-left side plotted in light green, and the model is in a continuous dark blue line. d) The observed dvv/v on the north-right side is plotted in dark green, and the model is in a continuous dark blue line.

the linear effect  $\alpha$  and the velocity drop  $\beta$  are variables accurately estimated, whereas the remaining effects  $\gamma$  and  $\delta$  are not. Nonetheless, the general features of the dv/v observations in the 32 datasets are captured by the model as observed in Figure 3.5, which suggests the dv/v observations depend strongly on  $\alpha$  and  $\beta$ . In contrast, the observations depend only weakly on  $\gamma$  and  $\delta$ , emphasising the poor relationship between the measurements and those variables, which is attributed to the nature of the phenomenon those variables intend to describe.

## 3.4.2 The analysis of $\alpha$ , the linear effect

This effect represents a linear change of dv/v measurements as a function of time (a dv/v rate with units of  $\frac{dv/v}{sec}$ ). Figure 3.6b shows the estimated linear effects at different compressive force levels on concrete of low and high integrity. The behaviour of this phenomenon is rather complex throughout the experiment, but some remarks can be deduced:

• Concrete of low integrity level: Locations of the bridge with relatively low ultrasound pulse velocities tend to show high magnitudes of this linear non-stationary elastic effect. At constant force rates (Figure 3.6a), this effect is up to three times higher on the North left side. This effect has a negative slope (decreasing dv/v through time) while decompressing the structure and tends to be positive after 310kN while compressing (meaning a time-dependent increment on the velocity of wave propagation). At high compressive force rates, the magnitude of this effect is decreased in the concrete of low integrity (slow time-dependent changes at quick compressive force level changes). Considering the standard

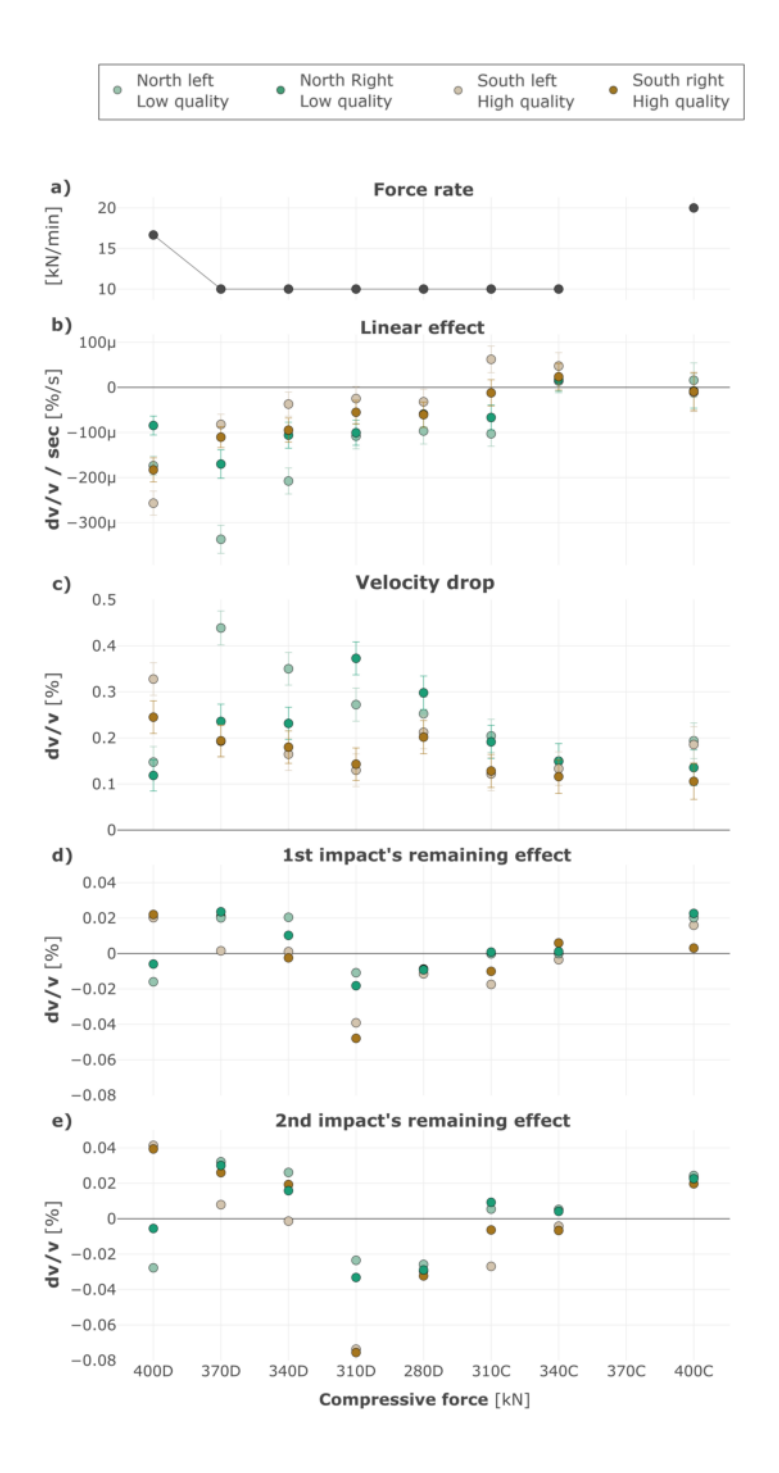


**Figure 3.6**: The force rate and the estimated model parameters result from the data inversion process. a) The estimated compressive force rate (static changes) during the experiment. b) The linear effects,  $\alpha$  values. c) The maximum amplitude of transients (velocity drop),  $\beta$  values. d) the 1st impact's remaining effect,  $\gamma$  values, acting on the second relaxation process. e) the 2nd impact's remaining effect,  $\delta$  values, acting on the third relaxation process.

deviations of such estimations, there is still a significant difference between the linear effect observed in the North left and right sides, leading to the conclusion that the dv/v rate affects the locations with concrete of relatively low integrity levels at different magnitudes, mostly while decompression.

• Concrete of low integrity level: Locations with high ultrasound pulse velocity values exhibit lower magnitudes of this linear dv/v rate when the compressive force rate (Figure 3.6a) was constant. This effect has a negative dv/v rate while decompressing and a positive dv/v rate while compressing after 280kN. Considering the standard deviations of such estimations, there is no significant difference between the linear effect observed in the South left and right sides. It can be concluded that the dv/v rate affects the locations with concrete of relatively high integrity levels at similar magnitudes.

## 3.4.3 The analysis of $\beta$ , the velocity drops

This section analyses the stress-dependent evolution of consecutive Slow dynamics effects for concrete with relatively different integrity levels. As stated before, Slow dynamics is composed of an almost instantaneous softening (or Velocity drop) and a slow recovery process. This investigation analyses the velocity drop effect  $\beta$ , the sought parameter in the inversion process.

Figure 3.6c plots the velocity drops estimated at different compressive force levels on concrete of varying integrity. The following behaviour can be noted in velocity drops with respect to the varying compressive force levels and the compressive force rates

- The relationship of velocity drops with the compressive force levels.
  - Figure 3.6c shows a complex behaviour for concrete of relatively low integrity level (dark and light green dots):
    - \* The concrete of low integrity generally softens twice compared to the concrete of high integrity.
    - \* The concrete of low integrity softens more while decompressing than compressing (different damage kinematics on decompression and compression).
  - Figure 3.6c shows a systematic behaviour for concrete of relatively high integrity level (dark and light brown dots):
    - \* The concrete of high integrity generally softens the half compared to concrete of low integrity.
    - \* The concrete of high integrity softens symmetrically at decompression and compression (similar damage kinematics on decompression and compression).
    - \* The concrete of high integrity softens the more when the structure is less compressed (at 280kN, the lowest compressive force level in the experiment).
    - \* The concrete of high integrity softens less at high compressive force levels.

- \* Considering the standard deviations of such estimations, it can be concluded that places with concrete of high integrity level (South left and right) soften at comparable magnitudes along the experiment.
- The relationship of velocity drops with the compressive force rates (Figure 3.6a).
  - At constant and low compressive force rates, these locations soften twice compared to the concrete of high integrity. This behaviour changes at compressive force rates higher than 15 kN/min, where places with concrete of high integrity level tend to soften more than places with concrete of low integrity

## 3.4.4 Time-dependent elastic and energy dissipation changes.

So far, instantaneous velocity drops and relaxation processes are observed with relative velocity changes dv/v measurements and remaining decorrelation (explained in Chapter 2). In this section, the energy content of the waveform used to calculate relative velocity changes dv/v is estimated and analysed. This analysis is carried out to gain insights into the physical mechanism responsible for the observed velocity variation in the concrete structure at the material scale.

Energy content analysis is meaningful as variations in the wavefield's amplitude evidence the presence of microstructures like pores and microcracks, since the transmitted energy dissipates (Suaris and Fernando, 1987; Pahlavan et al., 2018; Pal Kaur et al., 2019). To test the possible influence of microcracks during velocity drops and relaxation processes in this experiment, a qualitative analysis of the energy content of the ultrasound waveforms is performed. During the experiment, each pair of embedded ultrasound transducers used a constant 10-volt source to send mechanical waves from the transducer to the receiver at the four locations on the bridge. An important remark is the difference in the sensitivity used for each pair of transducers. The sensitivity was not the same for the four pairs, but once it was set, it remained constant throughout the experiment. While dv/v changes represent differences in the velocity at which such mechanical waves travel through the media, the energy of the signal can be used as a proxy for wave attenuation and serve as an indicator of energy dissipation. Analysing this phenomenon is important because it provides more information about the nature of the physical mechanisms that distort the wave propagation process as a consequence of the static and dynamic changes. It is important to note that energy estimations or attenuation measurements are highly affected by sensor-structure coupling effects (Tinard et al., 2025), and such effect is considerably decreased in this experiment since the ultrasound sensors are embedded inside the structure.

The mathematical definition of the energy of a continuous signal is (Oppenheim, 1999):

$$E = \int_{-\infty}^{\infty} |x(t)|^2 dt, \qquad (3.15)$$

where the signal energy E is defined as the sum of the instantaneous power  $|x(t)|^2$  of the time series x(t) from  $-\infty$  to  $\infty$ . For a Discrete-time signal, the equation 3.15 takes the following form:

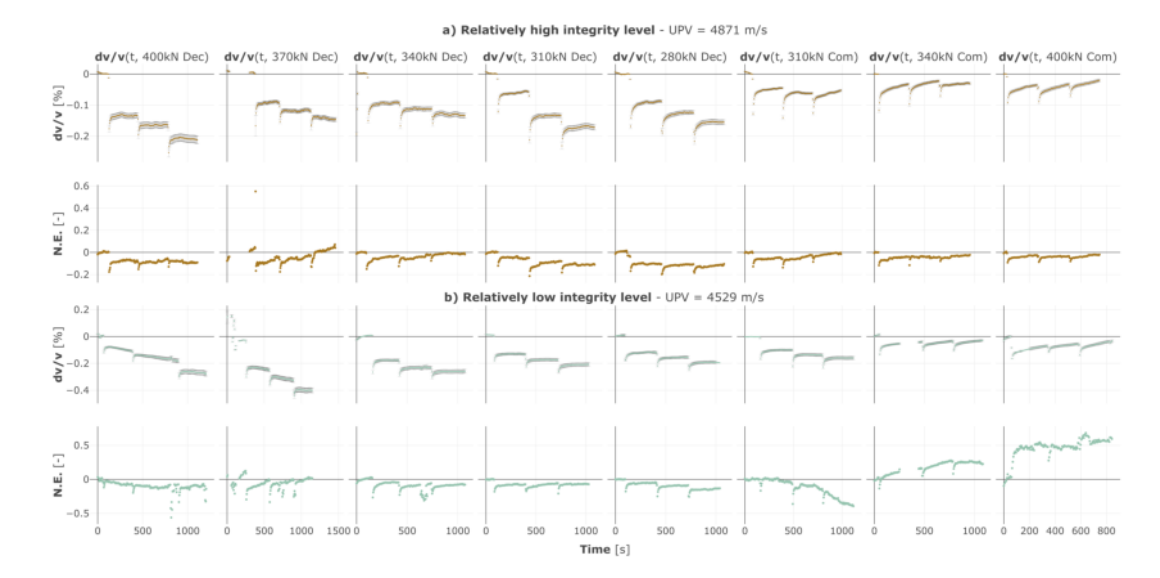


**Figure 3.7:** Dv/v and Normalised Energy (N.E.) content datasets for concrete with the a) highest and b) lowest integrity levels.

$$E = \sum_{n = -\infty}^{\infty} |x[n]|^2.$$
 (3.16)

Equation 3.16 is used to estimate the energy content of the time window used to estimate time-dependent dv/v changes, where n goes from 600 (the sample corresponding to the beginning of the time window) to 2000 (the sample corresponding to the end of the time window) as shown in Chapter 2, Figure 2.2e

Figure 3.7 compares time-dependent relative velocity changes and time-dependent energy content for concrete with high and low integrity levels at eight different compressive force levels. The high integrity level case is shown in dark brown colour (Figure 3.7a). Dv/v measurements are the same as in FIGURE, whereas the Normalised Energy (N.E.) is the energy content normalised by the maximum dv/v value. This normalisation process was carried out to take the Energy content estimation (equation 3.16) to the same order of magnitudes in estimations of both integrity levels and perform this qualitative description. In the upper panel of Figure 3.7, it is observed that the softening and recovery processes induced by the three VISs recorded in the dv/v estimations are also captured by the time-dependent evolution of the energy content estimations. The set of three softening and recovery processes is observed in the concrete with relatively high integrity at the eight different compressive force levels. This suggests that the material softening projected in the temporal changes of dv/v induced by the VISs are accompanied by energy dissipative processes. The opposite is the case for concrete with a low integrity level (Figure 3.7b), where the set of three softening and recovery processes is well-defined by energy content estimations only when concrete is undergoing decompression (From 400kN Dec to 280kN Dec). Even at high compressive force levels under decompression (400kN Dec and 370kN Dec), the energy content measurements are scattered but still reveal the baseline phase and the decrement in energy and subsequent recovery processes. During compression, energy content measurements capture an effect reminiscent of the recovery process, a log-time curve, that goes to energy content levels beyond the baseline phase almost instantaneously after

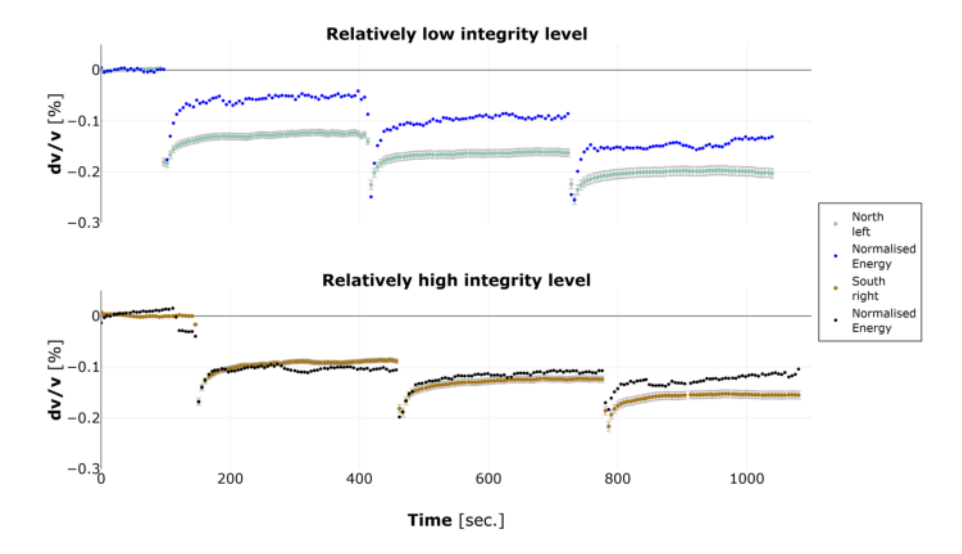


Figure 3.8: Comparison of the three consecutive relaxation processes recorded with dv/v and normalised energy content on concrete of different integrity levels at a compressive force of 280 kN.

the velocity and energy content drops. This suggests that the energy is not dissipated during slow dynamics processes while compressing the concrete with low integrity levels. Instead, the energy seems to be conserved and even increased as time progresses when the structure is compressed (340kN and 400kN).

The different stress-dependent energy content behaviour in concrete with low and high integrity levels can be explained by the following reasons: I) There are different structure-sensor coupling effects at the four locations on the bridge as a result of variations in the concrete's internal composition (spatial differences in the concrete's heterogeneity), and II) As the level of compressive force changes, a higher density of dissipative microstructures is activated in concrete with low integrity compared to concrete with high integrity.

## 3.5 Discussion

## 3.5.1 Possible physical mechanisms for slow dynamics in concrete

Figure 3.8 plots a zoom-in view of the dataset recorded at 280 kN for both integrity levels. Here, the normalised energy measurements are superimposed on the dv/v estimations to observe the presence of time-dependent elastic effects (dv/v(t)) and time-dependent dissipative effects (NE(t)). In this plot, the normalised energy measurements also capture the baseline phase and the set of three softening and recovery processes. For concrete with a high integrity level, there is a similarity in the shape and magnitude of the relaxation processes, suggesting similarities in the relaxation time scales for elastic and dissipative processes. For concrete with a Low integrity level, there are differences in terms of magnitude and shape of relaxation processes observed with dv/v and N.E. These differences suggest different relaxation time scales between elastic and dissipative processes in the concrete of low integrity level.

The exhibited changes in the energetic content of the waveform through time shape the softening and relaxation process in a similar way as relative dv/v measurements do, suggesting that the changes in the scattering properties in the concrete as a consequence of the VIS: I) are temporal from the perspective or dv/v, remanent decorrelation, and energy content, since they tend to go back to its reference values in the long term, and II) those temporal scatters also dissipate energy as micro imperfections in materials do. The energy content analysis gives support to the hypothesis of preexisting micro imperfections at many scales —ranging from the length scale of dislocations up to the crack and fracture scale (Lieou et al., 2017) — opening and closing as the structure is perturbed (compressive force levels and VISs) and different magnitudes of nonlinear elastic effects related to different number densities of such micro imperfections on concrete of low and high integrity, as stated in Chapter 2, in the Discussion section.

## 3.5.2 Relationship between $\alpha$ and $\beta$ with structural effects

In the previous section, the behaviour of the stress-dependent velocity drops was discussed for concrete of different integrity levels, and a plausible physical interpretation that explains time-dependent elastic and dissipative effects was laid out in terms of micro imperfections. This section analyses the stress-dependency of the linear effect  $\alpha$ . This qualitative interpretation suggests a possible explanation for the linear effect observed in the dv/v measurements and how its evolution throughout the experiment can be interpreted in terms of structural changes. It is crucial to highlight that this interpretation is based solely on relative velocity changes estimated using signals at ultrasound frequencies. To validate this interpretation, additional information is needed. (i.e. static deformation

The stress protocol exposed in Chapter 2 indicates eight static changes in the structure (changes in the compressive force levels) every 35 minutes approximately, inducing a static deformation on the horizontal beam. The natural reaction of solids to constantly hold mechanical stress (static changes) is a slow, time-dependent deformation known as Creep. This time-dependent deformation is observed as a slow flow of the material, which behaves as if it were viscous (Meyers and Chawla, 2009). Although Creep as a result of applied stress often results in permanent plastic deformation, much of it is often recoverable; subsequently, creep recovery returns the material to its initial state in a characteristic log (recovery time) behaviour (For this reason, Slow dynamics, by definition is a behaviour reminiscent to Creep (TenCate, 2011)). The Creep timedependent curves are usually divided into three stages: I) primary or transient Creep, II) Secondary, constant Creep rate, or quasi-viscous stage, and III) Tertiary Creep, where the acceleration of the deformation occurs and leads to failure. The shape of the stages of Creep curves vary depending on the temperature, the variability of stress levels (Ross, 1958), and the direction of deformation (tension or compression) (Ranaivomanana et al., 2013). Figure 3.9 shows the dv/v estimation obtained in the North span of the structure (left and right) after changing the compressive force levels on the structure from 340 kN to 310 kN, exhibiting a Creep-like effect. These two Creep-like curves behave differently depending on the time window selected to estimate dv/v, one reminiscent of Creep concrete under compression and the other reminiscent of Creep concrete under tension (Ranaivomanana et al., 2013). This observation leads to the conclusion that stress distribution volumes in the horizontal beam 3.10 vary when the concrete specimen undergoes static changes, as observed by Saqan (Saqan and Rasheed, 2011),

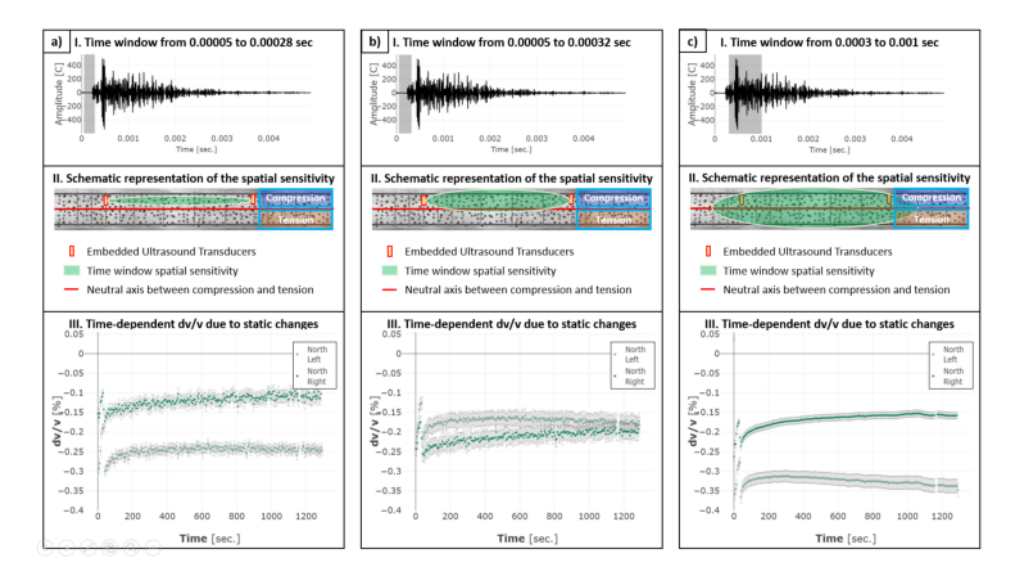


Figure 3.9: The time-window-dependent behavior of the creep-like effect recorded after the change in the compressive force levels. A) I. Short time window, II. The sensitivity of the waves dominantly on the beam's compression volume, and III. The compressive-creep-like effect observed with the dv/v estimations for the North-Left and Right sides. B) I. A widened time window, II. The sensitivity of the waves mostly on the beam's compression volume and slightly on the beams' tension volume, and III. The creep-like effect observed with the dv/v estimations for the North-Left and Right sides. C) I. The early coda time window, II. The sensitivity of the waves all around the vicinity of the ultrasound transducers, and III. The creep-like effect observed with the dv/v estimations for the North-Left and Right sides.

Mohammadhassani (Mohammadhassani et al., 2011), and Lou (Lou et al., 2015). This change in the stress distribution volumes leads to variations of tensile and compressive volumes on the beam as the compressive force level changes (ilustrated in Figure 3.10). Tension and compression in concrete result in relative velocity changes dv/v with opposite signs (Diewald et al., 2022), implying a softening and strengthening of concrete, respectively, or vice versa, depending on the data processing setup and heterogeneity of concrete. This linear behaviour can be related to the second phase of Creep, when the Creep rate is constant and dominantly linear, as observed in Figure 3.9 aIII, bIII, and cIII from 200 seconds onwards. The direction (the slope's sign) of this linear behaviour might be connected to deflection processes on the beam that cause variations in volumes under tension and compression in the structure.

The magnitudes dv/v rate estimated by the model are in the order of magnitudes of  $3x10^{-4}$  to  $9x10^{-6} \frac{dv/v}{sec.}$ , which is four orders of magnitude higher than reported in lab experiments for long-term monitoring of creep in concrete via static measurements of elastic properties (Hong et al., 2023).

## 3.6 Conclusions

The conclusions are laid out in the following three main concerns.

About Physical implications of Nonlinear elastic effects

• Energy content estimations add insights into the physical mechanism that causes Slow Dynamics effects in concrete. In this experiment, time-dependent elastic

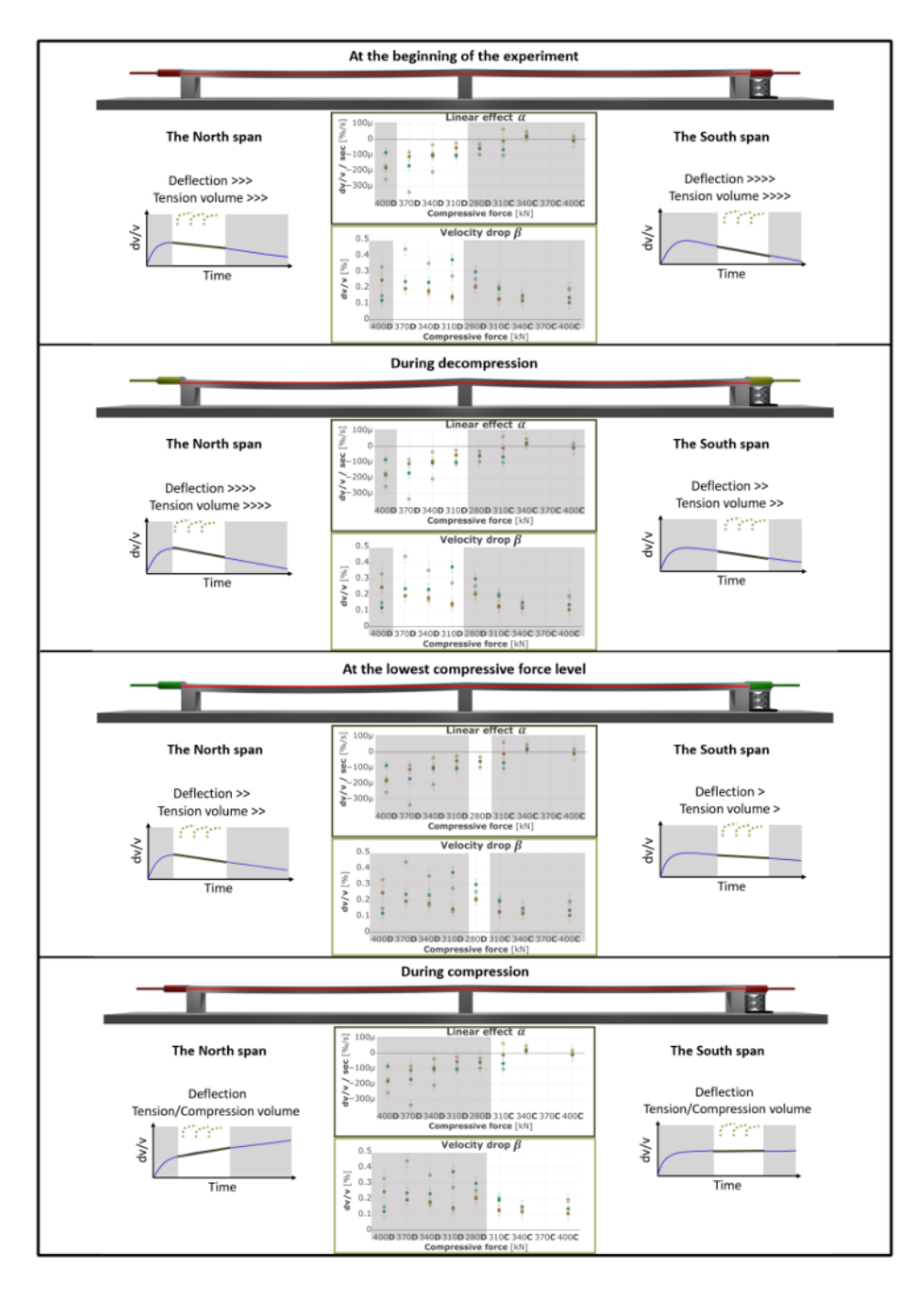


Figure 3.10: Schematic representation of deflection changes on the bridge during the experiment and their effect on the Slow dynamic processes. Deflections tend to change the tension and compression volumes on the horizontal beam (see the red line neutral axis along the beam as a reference), causing different creep-like behaviour at every compressive force change, where the three slow dynamics processes are superimposed. This figure shows different deflection scenarios for the north and south spans and their possible effect on the second phase of creep related to the linear effect: I) at the beginning of the experiment, II) when the structure is undergoing decompression, III) at the lowest compressive force level and IV) when the structure is undergoing compression.

- and dissipative changes are observed, and those features are intrinsic to micro imperfections like microcracks;
- From an analytical perspective, there is a relationship between the quality of concrete and phenomena related to nonlinear elasticity, such as Slow dynamics. The magnitude of velocity drops is higher in concrete of relatively low quality than in concrete of relatively high quality, no matter the compressive force level, as long as the compressive force rate is constant;
- Structural effects affect the velocity drops: The compressive force causes structural alterations, and the rate of this compressive force was observed to change considerably the magnitude of velocity drops in concrete of low and high integrity;
- The structural disposition of the member matters: Deflections in the horizontal slender concrete beam could trigger viscoelastic features of concrete, e.g., Ceep, in various forms. This viscoelastic effect might reshape the Slow Dynamic curves as observed in this experiment. This opens the discussion on Slow dynamics processes superimposed on viscoelastic effects like Creep and their time-dependent interaction.

## About the techniques and methods

- Recording Slow dynamic processes along five minutes with 5-second dv/v estimations seems to provide information correlatable with ultrasound pulse velocities. Still, information is missing (e.g., the minimum and maximum time scales of the Slow dynamics processes). For practical estimations, this setup works and Slow dynamics remain meaningful;
- The Coda Wave Interferometry stretching method works as a stable monitoring tool in field condition experiments. Energy content estimations are highly sensitive to material changes and are recommended when a proper coupling sensor-structure is guaranteed;
- Interestingly, To estimate time-dependent energy content changes, there is no need for a reference measurement as in the Coda Wave Interferometry Stretching technique, but it requires a constant energy pulse, namely the source, and a continuous structure-sensor coupling through the experiment;
- Vertical Impulsive Sources (VIS) such as Vertical drop weights and Hammer Hits
  are practical approaches to induce low-level reversible damage in field-conditioned
  concrete structures. The effect of each of the three VIS in the structure is coherent
  and repeatable (each VIS has the same effect on the structure at a given compressive
  force level);
- In structures where the confining forces or the external solicitations vary, taking different estimations at different confining force levels would also bring insights into the microstructural composition. Places with high variability of nonlinear elastic effects tend to have low UPVs and, therefore, lower integrity levels.

## About the analytical model

- Practical analytical models like Snieder et al., (Snieder et al., 2017) for Slow Dynamics are helpful in modelling field-condition observations recorded in complex situations;
- The analytical model developed in this chapter reproduces the effect of consecutive Slow Dynamics processes at varying compressive force levels;
- This analytical model is parameterisable by four variables and reproduces observations recorded under non-highly controlled conditions;
- The results obtained analytically in this chapter are qualitatively comparable to the results obtained observationally in Chapter 2.

## 4

## Observations of Nonlinear Elasticity in a Concrete Structure using Standing Waves

This chapter analyses the performance of conventional low-frequency seismic equipment in measuring stress-dependent elastic effects (Classical Nonlinear Elastic effects) in a concrete structure. This analysis focuses on two key parameters: I) Relative velocity changes and II) Coda wave decay, both evaluated as functions of the applied compressive force levels. The results demonstrate the potential of conventional seismic equipment to detect spatial variations in the oscillation velocity of standing waves, which may be associated with local changes in the mass and stiffness of the concrete structure.

## **Contents**

4.1	Introd	uction	54
4.2	Eigenfrequencies of the bridge		
4.3	Analysis of stress-dependent dv/v changes of standing waves		
	4.3.1	Calculation of ACF	56
	4.3.2	Stress-dependent dv/v calculation	58
	4.3.3	The stress-dependent elastic behaviour of standing waves	60
	4.3.4	Discussion on the velocity changes of the fundamental vibra-	
		tion mode	61
4.4	Analysis of stress-dependent coda wave decay		
	4.4.1	The Coda Q model and estimation for a concrete structure	64
	4.4.2	Discussion on the Coda Q analysis	65
4.5	Conclusions		67

## 4.1 Introduction

This section outlines a description and analysis of the data recorded with conventional seismology equipment during the experiment in the BLEIB structure described in Chapter 2. This conventional seismology equipment records information at frequency bands four orders of magnitude below the equipment used to monitor material changes in the concrete. It consists of a 24-channel Geode seismograph datalogger with a 1.75 Hz to 20 kHz operational bandwidth equipped with a GPS synchronisation system and a Raspberry Pi auto-triggering system that allows continuous vibration recordings with 24 channels. For this experiment, 14 channels were activated with 14 geophones of a single vertical component and a 4.5 Hz Natural frequency to record vibrations at a 500 Hz sampling frequency. Traditionally, this type of equipment is used for shallow seismic exploration by means of wave dispersion (SPAC, MASW), wave refraction, and wave reflection surveys.

In this experiment, a linear array of twelve geophones spaced 1.3 meters apart was placed and attached with plaster on the top surface of the test bridge, one more sensor on the foundation of the structure, and one more on the natural subsoil 3 meters away from the structure to record vibrations at a frequency band between 4.5 and 250 Hz. Those vibrations are composed of a cascade of mechanical waves of different natures, such as travelling waves that originate from external sources, impinge on the structure omnidirectionally, and propagate within the concrete (body waves) and/or its surface (surface waves). Those, in turn, originate standing waves in the bridge (the superposition of waves with similar or equal frequencies in a bounded media (Kneubühl, 1997)) whose physical properties are dictated by the structural dynamic response of the bridge.

Measuring the velocity of travelling waves or their relative velocity change on the bridge at the abovementioned frequency band is limited: I) body waves like compressive and shear waves travel at velocities ranging from 3500 to 4800 m/s (Lee and Oh, 2016) and form 1790 to 2100 m/s (Lee et al., 2017), respectively. II) surface waves, although more energetic, travel at lower velocities; Rayleigh waves have a propagation velocity from 1800 to 2500 m/s (Lee and Oh, 2016) in the concrete, and Lamb waves, which need specific conditions to be generated and propagated, have a propagation velocity of 1850 m/s at frequencies of the order of  $x10^3$  (Stähler et al., 2011) and varies with the thickness of the concrete beam (Royer and Valier-Brasier, 2022). Sensing travelling waves along a 24-meter-long concrete bridge to quantify their velocity or amplitude variations on detail requires sensors with a higher operational frequency band or significantly larger concrete samples.

Nonetheless, conventional seismic equipment can well capture certain types of lowfrequency vibrations that do not propagate but stay ringing on the structure; those, by definition, are called Standing waves. This section investigates the stress dependency of those low-frequency vibrations in two components. First, the relative velocity changes (dv/v) of the fundamental standing wave of the bridge are estimated and analysed using autocorrelation functions and coda wave interferometry. Such velocity changes are studied as a function of the space and the different compressive force levels.

Second, the attenuation of energy induced by the Vertical Impulsive Sources (VIS) at the standing wave frequency band is analysed. To this end, the coda wave decay concept is used. This section investigates the spatial variations of such coda wave decay along the bridge and their changes as a function of the different compressive force levels.

## Eigenfrequencies of the bridge 4.2

Standing waves are triggered in civil structures due to the surrounding vibration conditions (e.g., wind, pedestrians, and traffic), and they are used to determine the modal parameters of the structure such as the fundamental way the structure vibrates and the set of all possible standing waves (the first and superior harmonics named as eigenfrequencies or natural frequencies), as well as damping rations and mode shapes, this by performing Modal analysis on the structure (Bertero et al., 2022).

Modal analysis is part of the vibration-based methodologies for structural health monitoring (Introduction Table 1), and there is a well-established range of algorithms and methodologies to perform such analysis in civil structures using vibration recordings (Pioldi et al., 2022). Modal analysis was carried out in the BLEIB structure numerically via the Finite Element Method (Liao et al., 2021), and experimentally using a set of six-degreeof-freedom sensors (Dhabu et al., 2024). These analyses estimated the fundamental and higher-order frequencies of such standing waves on the bridge as indicated in Figure 4.1 with the four vertical lines in both graphs.

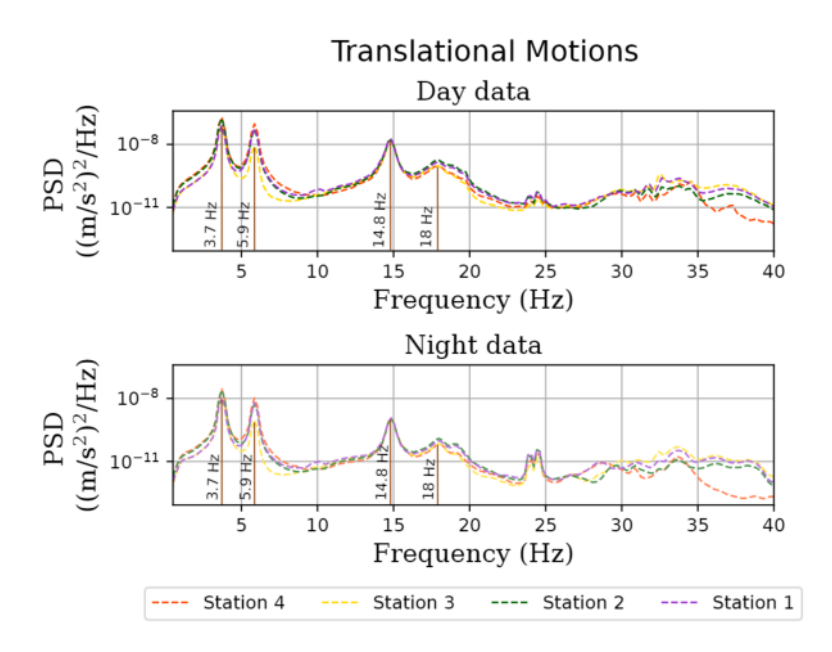


Figure 4.1: Eigenfrequency analysis of the bridge with data recorded during the day (upper panel) and night (lower panel) with four translational sensors distributed along the bridge. Both analyses show the fundamental frequency of the bridge at 3.76 Hz, and three higher harmonics. Results were obtained in the frame of the GIOTTO project [Submitted by Dhabu et al., 2024].

There are slight differences in the fundamental frequency estimated numerically (3.9 Hz) and experimentally (3.76 Hz) on the bridge, nonetheless, they are still within the operational bandwidth of the linear array deployed for this experiment.

In this chapter, the relative velocity change on the oscillation of the fundamental standing wave (with a frequency of 3.7 Hz) is analysed as a function of the stress, using the recordings obtained with the twelve one-component geophones deployed on the bridge. To investigate the attenuation phenomenon at low frequencies and its stress-dependency, the coda wave decay is estimated for the Vertical Impulsive Sources recorded at the twelve different positions along the bridge.

## Analysis of stress-dependent dv/v changes of standing 4.3 waves

To carry out this analysis, a signal processing technique is required to enhance coherent waves recorded by a single station, in this case, the fundamental stationary wave. Autocorrelation is a signal processing technique that transforms any pair of coherent waves into a single pulse, while incoherent waves cancel out (Claerbout, 1968). Inspired by this technique and the handful of studies that support the functionality of this methodology in the context of seismology (Gorbatov et al., 2013; Phám and Tkalčić, 2017; Bonilla et al., 2019; De Plaen et al., 2019; Lu and Ben-Zion, 2021), the autocorrelation functions are estimated to calculate stress-dependent dv/v on the bridge.

## Calculation of ACF 4.3.1

The autocorrelation function (ACF) is the convolution of source and zero offset impulse response functions at the analysed station (Qin et al., 2023). Here, the ACFs of lowfrequency recordings are computed to infer the changes in the velocity of standing waves at the fundamental frequency of the structure sensed at 12 different points. In this work, autocorrelations of data are computed in fixed time windows of continuous waveforms as follows:

- A pre-processing stage was performed on the vibration recordings obtained for each compressive force level: the linear trend was removed from the raw data, and the beginnings and ends of the signals were smoothed. Since this investigation focuses on tracking stress-dependent changes in the fundamental mode of the structure, the continuous recordings were filtered in the frequency band of  $F_{min}$  =  $0.8 \times F_c$  and  $F_{min} = 1.2 \times F_c$ , where  $F_c$  equals the fundamental frequency of the beam Fc = 3.76 to suppress the influence of superior modes of vibration. The one-bit temporal normalisation method was used to attenuate the effect of the transient signals (H Zhang et al., 2021) induced by the VIS, whose amplitude is considerably larger than the average noise level.
- The pre-processed vibration recordings were divided into one-minute time windows; no time window overlapping was considered in this process. Broadly speaking, 30 one-minute time windows are obtained in this process.
- The autocorrelation process is carried out for each time window to obtain different autocorrelation functions.
- To increase the signal-to-noise ratio, the autocorrelation functions are stacked to obtain one autocorrelation function for each compressive force level.

Figures 4.2a and 4.2b plot vibration recordings obtained in station G01 at a compressive force of 400kN and 370, respectively. The shadowed areas correspond to the non-overlapped time windows used to get the stacked one-minute autocorrelation functions representative of each compressive force level. The causal part of the ACF calculated with the vibration recordings corresponding to the compressive force of 400 kN is plotted in Figure 4.2c, and the ACF corresponding to the compressive force level of 370 kN is plotted in Figure 4.2d.

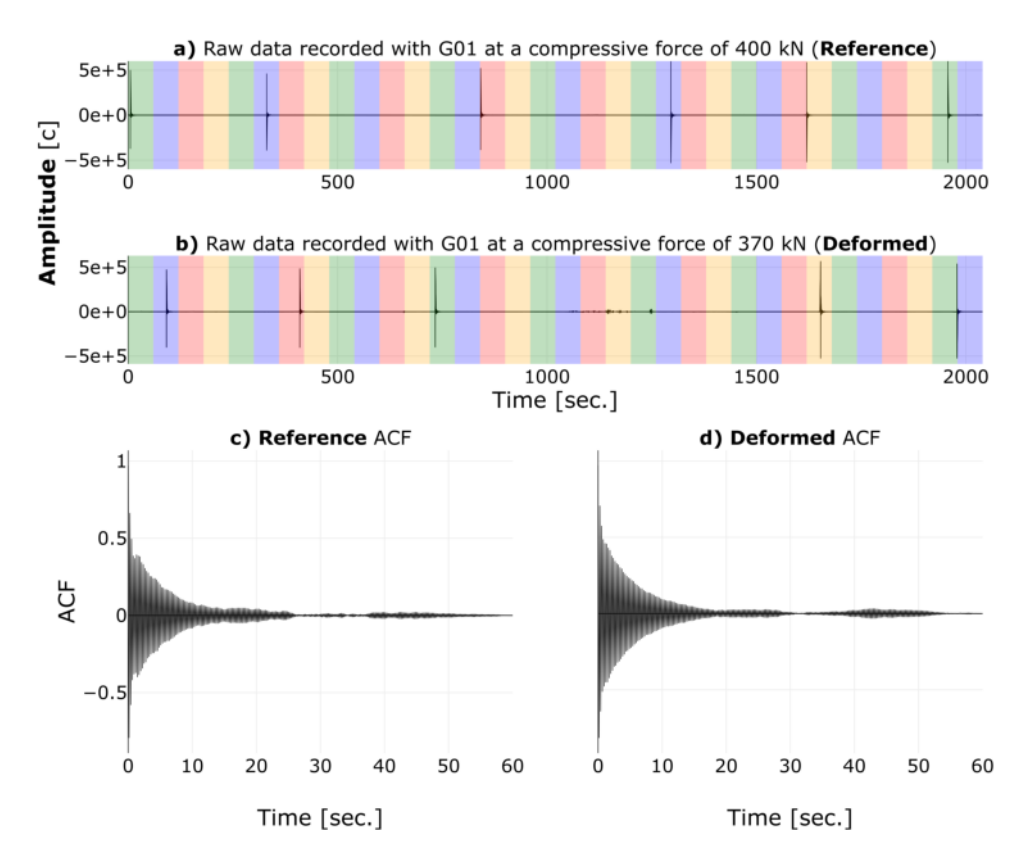


Figure 4.2: The data employed to calculate the autocorrelation functions. a) plots the raw data recorded at the Geophone 1 (G01) when the structure was compressed at the initial compressive force level for this experiment (400 kN), which is the reference state. b) plots the raw data recorded with the same sensor when the structure was compressed at the second compressive force level for this experiment (370 kN), which is the first deformed state. The vertical colour bands represent the one-minute time windows used to calculate the autocorrelation function for the c) reference state, and the d) first deformed state.

These two ACFs served to estimate the relative velocity changes of the standing waves at the fundamental frequency of the structure. To do so, the Coda Wave Interferometry stretching technique was used. The theoretical foundations and functionality of this technique are described in Chapter 2 of this document. Broadly speaking, the stretching technique estimates relative velocity changes by calculating the stretching factor  $\epsilon$  between two waveforms: a reference waveform, which is the ACF estimated at 400 kN, and the deformed version of it, which is the ACF estimated at 370 kN (or any of the subsequent compressive force levels in this experiment).

In this investigation, the stretching factor  $\epsilon$  was estimated using different time window lengths of the ACFs, going from 0.4 sec to 30 sec, with increments of 0.4 sec. The results are observed in Figure 2. The cross-correlation coefficients (CCC) as a function of the time window length are plotted in Figure 4.3a. Overall, CCC above 0.99 are obtained. This implies a high similarity between the reference and deformed ACF after the stretching process and, therefore, a good reliability level on the estimated stretching factors  $\epsilon$ .

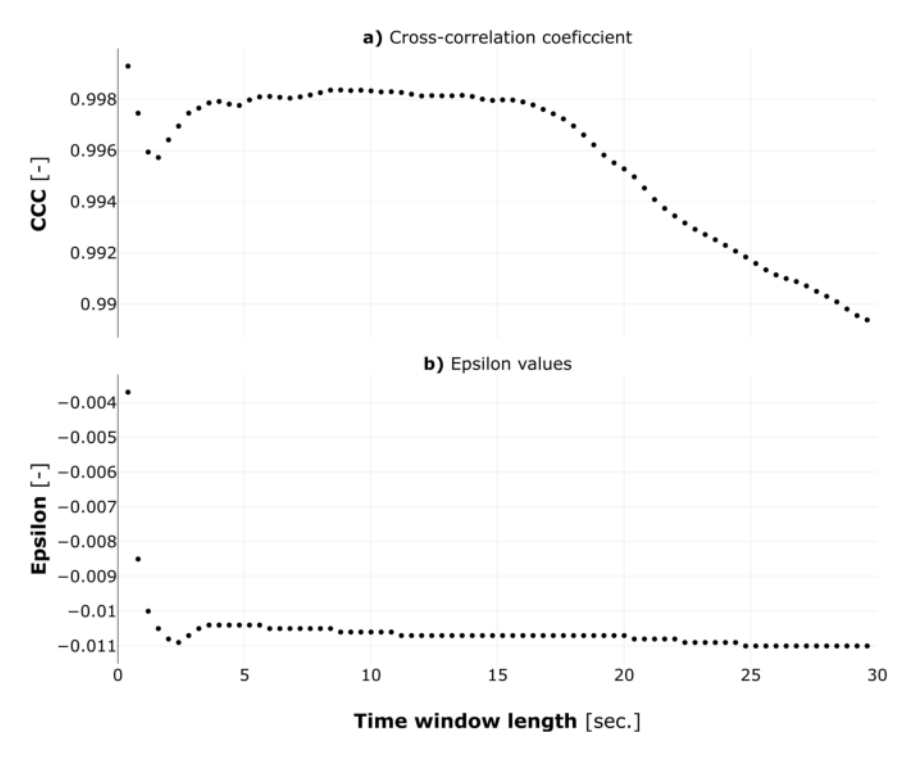


Figure 4.3: Cross-correlation functions and epsilon values as a function of the time window length. a) plots the cross-correlation values obtained after the stretching process of the reference and deformed autocorrelation functions, and b) the  $\epsilon$  values that maximise the cross-correlation between the reference and deformed states, as a function of the time window length.

Figure 4.3b plots the  $\epsilon$  values as a function of the time window length. A substantial decrement between 0.4 and 3 seconds is observed in  $\epsilon$  values, those with high CCC. After 3 seconds, the estimations become mostly stable, with an almost negligible decrement rate as a function of the time window length. To obtain a single representative  $\epsilon$ , the average of all the values for time window lengths between 5 and 30 seconds was estimated, and the maximum and minimum values were used to define the variability of this representative  $\epsilon$ .

#### Stress-dependent dv/v calculation 4.3.2

Figure 4.4 plots the average  $\epsilon$  value transformed to dv/v and its variability for sensor number G 01. The same process was carried out for the eleven additional sensors placed on top of the bridge, and the results are included in the same graph. Figure 4.4 plots the spatial variability of the relative velocity changes associated with the fundamental standing wave of frequency 3.76 Hz along the bridge.

As long as the compressive force is decreased, the velocity of the fundamental standing wave also decreases. This decrement is not homogeneous along the bridge. Geophones placed close to the vertical supports, that is, sensors G 01, G 06, and G 12, tend to observe lower dv/v decrements.

The dv/v decrement becomes more significant as the sensor position approaches both mid-spans of the beam. At the South span, covered from the sensor G 02 to G 05, the wave velocity decrement ranges from −1.0874 to −1.1296%, which means a

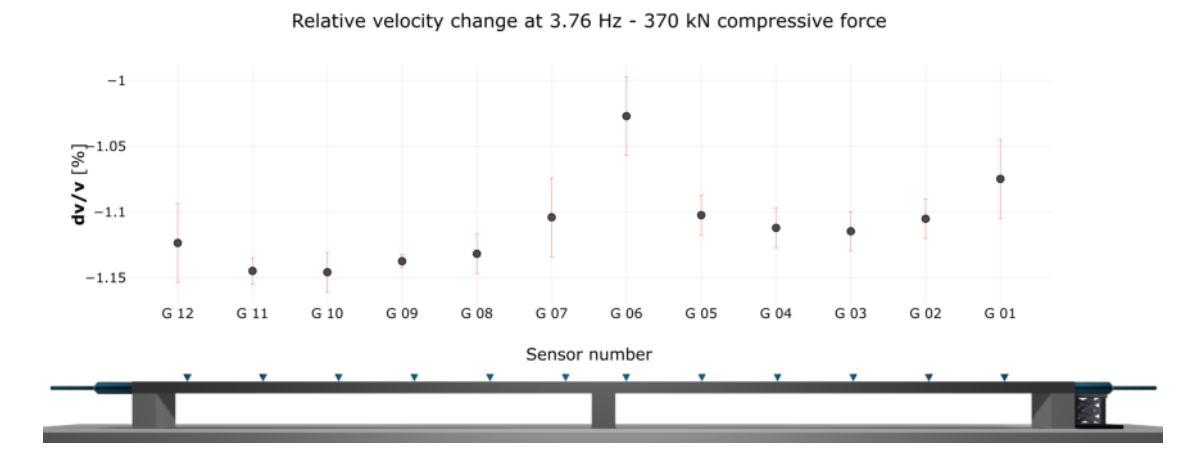


Figure 4.4: The relative velocity changes estimated with all the sensors along the beam at a central frequency of 3.76 Hz. The vertical axis plots the relative velocity changes obtained as a result of the first change in the compressive force on the bridge (from 400 kN to 370 kN). The lower part of the figure shows the beam and the location of each sensor (the twelve inverted blue cones placed on the surface of the bridge) to visualise the spatial distribution of the estimated relative velocity changes.

velocity decrement variability of around 0.0422%. On the other hand, at the North span covered by sensors G07 to G11, the wave velocity decrement range goes from −1.1167 to -1.1608%, with a variability of 0.0441%. Magnitude-wise, notable differences can be observed between both spans of the bridge, whereas the variability tends to be the same. It was observed that a 30 kN decrement in the compressive force is significant enough to induce changes in the structural dynamic behaviour of the beam, and such changes seem to affect both spans of the bridge differently.

Relative velocity changes can be estimated for all the six subsequent compressive force levels. Figure 4.5 plots the stress-dependent relative velocity changes estimated in sensor G 01 for decompressing and compressing. The vertical axis plots dv/v and horizontal the compressive force level. The error bars of each measurement are not visible since they are two orders of magnitude smaller than the total dv/v variability during the experiment.

The initial compressive force 400 kN R exhibits zero dv/v since this is the reference state. The structure exhibits dv/v decrements as the compressive force level is reduced (the dots for decompression) and vice versa (the crosses for compression). The stressdependent behaviour at low frequencies at this location on the bridge showed a maximum relative velocity decrement of 6.66% during the experiment. Although the compressive force was reduced in steps of 30 kN-generally at a constant rate of 10 kN/min-the corresponding dv/v decrements were not constants for each reduction step. Nonetheless, such stress-dependent change exhibits a seemingly linear trend, as observed in the high-frequency data (observations at the material scale), but with different magnitudes. This suggests that the effect of confining forces affects in a similar linear way the propagation velocity of body waves (as widely observed in lab and field experiments) and the oscillation velocity of the fundamental standing wave of the bridge when such confining forces change within concrete's elastic regime.

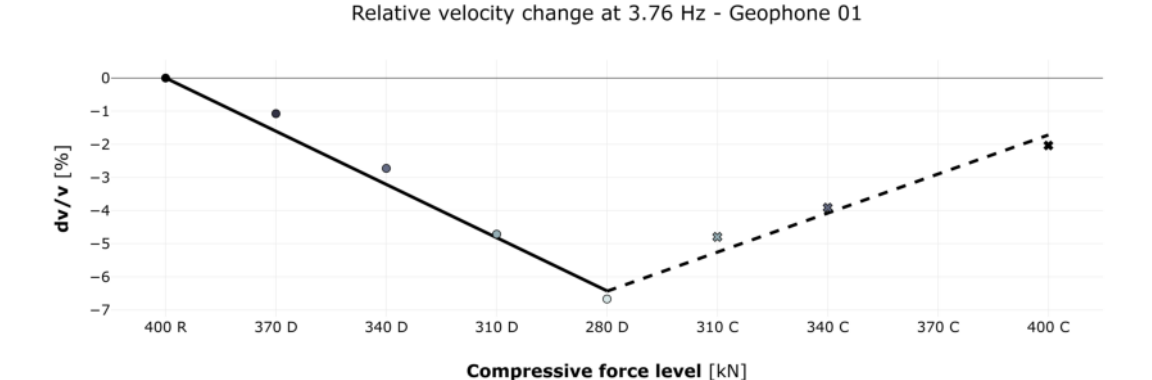


Figure 4.5: The relative velocity changes at a central frequency of 3.76 Hz as a function of stress (the compressive force level), obtained with the Geophone 01. The dots indicate dv/v values estimated while the structure was decompressed, and crosses indicate dv/v values while the structure was compressed. The continuous line represents the linear model that fits the dv/v measurements at decompression, and the dashed line is the linear model that fits the dv/v measurements at compression.

#### The stress-dependent elastic behaviour of standing waves 4.3.3

To quantify the dv/v as a function of stress, a weighted linear regression was carried out to estimate the analogous acoustoelastic effect (the slope of such linear behaviour) described in Chapter 2, but for standing waves. Figure 4.5 shows the linear model for decompression (continuous black line) and compression (dashed black line). In this plot, it is evident that both models are different since the initial elastic state of the bridge differs from the final elastic state. This difference in the acoustoelastic effect for decompression and compression was observed in body waves with the ultrasound data and reported in Chapter 2.

Stress-dependent dv/v was estimated for the whole geophone linear array for a central frequency of 3.76 Hz. Figure 4.6 shows how dv/v (Z-axis) changes linearly as a function of stress (X-axis) on all the twelve sensors along the bridge (Y-axis). Dots represent dv/v measurements for decompression, and crosses represent dv/v measurements for compression. The red lines along the Z-axis represent the variability of each dv/v measurement, which is negligible considering the overall dv/v variability along the experiment. This plot shows a consistent stress-dependent linear change along the bridge from the south span (Geophone number 1 to 6) to the north (Geophone number 7 to 12). This allows the estimation of the acoustoelastic effect on all 12 sensors for decompression and compression.

Spatial changes in the acoustoelastic effect are observed along the bridge. Figure 4.7 plots the estimated acoustoelastic effects for all twelve sensors on the bridge for both decompression (dots) and compression (crosses). The first feature observed in this graph is the difference in the acoustoelastic effect for decompression and compression. This behaviour is consistent with the acoustoelastic effect estimated at high frequencies with travelling waves. Magnitude-wise, this effect is higher during decompressing than compressing. While decompressing, this effect seems not to be affected by the vertical supports (as observed in the first compressive force change in Figure 4.4) since the magnitudes of the estimations at sensors G 01, G 06, and G 12 are relatable with the other sensors. The acoustoelastic effect exhibits a behaviour with low variability

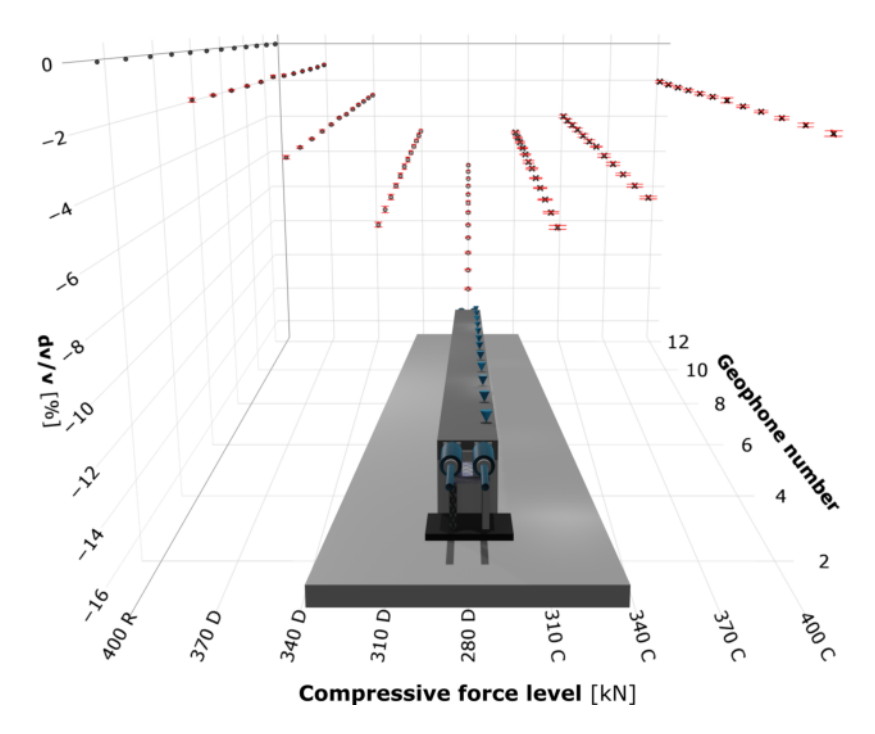


Figure 4.6: Stress-dependent relative velocity changes estimated at a central frequency of 3.76 Hz at all twelve geophones placed along the bridge. The Z-axis represents the relative velocity changes (dv/v), the X-axis represents the compressive force level (400 kN as a Reference state, and the subsequent seven deformed states at Decompression and Compression), and the Y-axis represents the geophone number (from G 01 to G 12 corresponding to the twelve inverted blue cones placed on the surface of the bridge). Dots correspond to dv/v estimations during decompression, and crosses correspond to estimations during compression. Vertical red bars indicate the error on the dv/v measurements.

at the south span of the bridge (from sensors G 02 to G 05). In contrast, this effect fluctuates more on the north span of the bridge (from sensors G 07 to G 11). While decompressing, higher acoustoelastic effects are obtained at G 10, and the lower value is observed at G 09, a location 1.3 meters apart.

The effect of the vertical supports of the bridge is observed on the acoustoelastic effect values measured while the bridge is under compression at sensors G 01, G 06, and G 12. Higher values are observed at G 01 and G 06 than in the other sensors. The fluctuation of the acoustoelastic effects is lower in the south span of the beam than in the north. However, while compressing, this acoustoelastic effect is higher on average in the south than in the north.

### Discussion on the velocity changes of the fundamental vibration 4.3.4 mode

The stress-dependent relative velocity changes observed in this investigation correspond to not travelling but the fundamental standing wave of the bridge. The fundamental standing wave (also known as the fundamental model of vibration of the structure) is characterized by I) a natural vibration frequency, which is 3.76 Hz for this structure, and II) The specific way the structure is deformed while vibrating, called mode shape. As

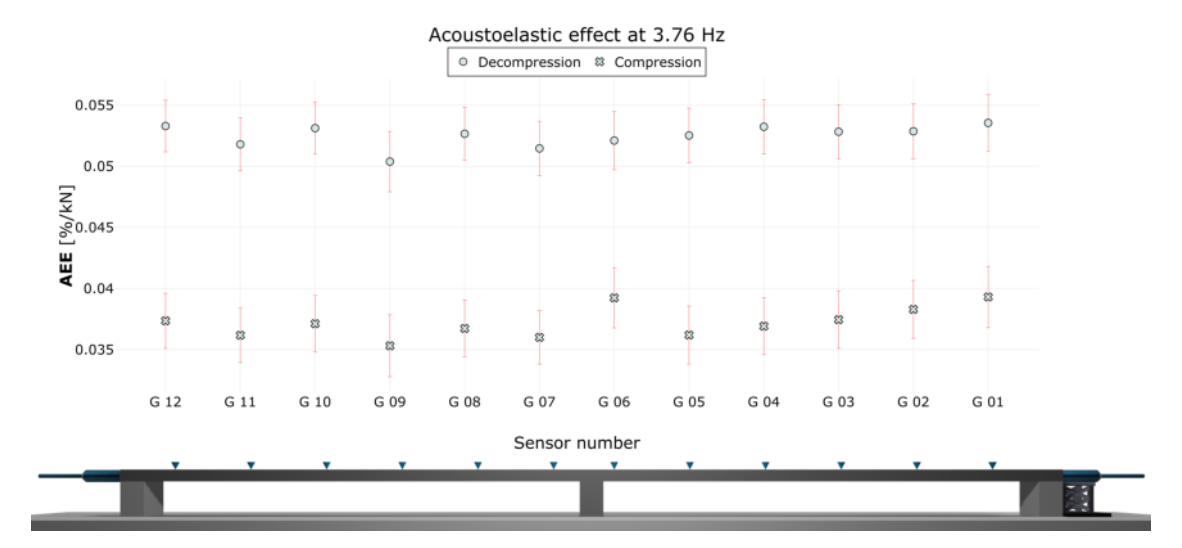


Figure 4.7: The acoustoelastic effect during decompression and compression of the fundamental standing wave of the bridge at a central frequency of 3.76 Hz, measured at all twelve geophones placed along the bridge. The vertical axis shows the slope of the linear relationship, dv/v, and stress level, also referred to as the acoustoelastic effect (AEE). Values for decompression are plotted with dots, and values for compression with crosses. The lower part of the figure shows the bridge and sensor locations (the twelve inverted blue cones placed on the surface of the bridge), illustrating the spatial distribution of the estimated AEE.

such, the mode shape brings information about the amplitude of such vibration in the form of displacements, and those displacements are not the same along the structure, since the natural frequencies and mode shapes of a structure depend entirely on its mass, stiffness distributions, and geometry (which defines the stiffness paths) (Chopra, 2007), therefore, different points in the structure move with different displacements, velocities, and accelerations.

In the modal analysis of a structure (typically modelled as a Multi-degree of freedom system), the displacement u(x, t) at a point x and time t is expressed as:

$$u(x,t) = \phi(x) \cdot q(t), \tag{4.1}$$

where the  $\phi(x)$  is the mode shape which represents the normalised spatial distribution of displacement, and q(t) is the modal coordinate that describes the time evolution of the movement and is usually a harmonic function. This analysis is carried out considering a single mode, which is the first mode of vibration. Then, q(t) is usually modelled as a simple harmonic motion as follows:

$$q(t) = X\cos(\omega t + \phi), \tag{4.2}$$

where q(t) dictates how all the points in the structure oscillate over time, X is the amplitude of the motion,  $\omega = 2\pi f$  is the angular frequency with f as the frequency in Hz, and  $\phi$  the phase angle (Chopra, 2007). In this investigation, velocity changes of the fundamental oscillation mode are estimated. Those velocity changes are relative to a reference state. The velocity of oscillation is then the time derivative of the displacement q(t):

$$v(t) = \frac{dq(t)}{dt} = -\omega X \sin(\omega t + \phi), \qquad (4.3)$$

so, at any time t, the velocity of the position x is given by the equation 4.3. The maximum velocity  $V_{max}$  is:

$$V_{max} = \omega X = 2\pi f \cdot X. \tag{4.4}$$

Equation 4.4 suggests that the velocity of oscillation of the points in the structure increases linearly with the frequency f and/or the amplitude X. This equation helps to determine the nature of the estimated relative velocity changes as a function of the stress conditions.

Changes in the displacement *X* (the amplitude of the vibration) are possible when the geometry of the structure changes, in this case, by the action of the different compressive force levels, possibly due to deflection effects. Effects of this type might cause changes at the material scale, as suggested in Chapter 3 Figure 3.10.

On the other hand, changes in the frequency of vibration of the fundamental mode can also provoke changes in the velocity of oscillation. The natural frequency of the system can be determined as a function of the intrinsic properties of the material as follows (Chopra, 2007):

$$f_n = \frac{1}{2\pi} \sqrt{\frac{k}{m}},\tag{4.5}$$

where k is the stiffness and m is the mass of the material. The equation 4.5 suggests that the natural frequency of the structure increases with the stiffness k (a stiffer material vibrates faster), and the natural frequency decreases with the mass m (a heavier material vibrates more slowly). Changes in the elastic properties of concrete led to changes in its frequency of vibration (equation 4.5) and, consequently, to changes in the velocity of oscillation of the mode shape of the bridge (equation 4.4).

Dhabu et al. (Dhabu et al., 2024) estimated changes in the natural frequency of the same bridge as a function of the compressive force level with a different stress protocol. Figure 4.8 shows variations in the frequency of the fundamental and higher modes on the beam, measured with six-component sensors (three translational components and three rotational components). The upper panel shows frequency shifts while decompressing, and the lower panel shows frequency shifts while compressing. Qualitatively, in both analyses, the eigenfrequencies tend to decrease as the compressive force level is reduced. This suggests that the mass or stiffness of the bridge changes as a function of the compressive force levels and induces variations in the velocity of oscillation of the fundamental standing wave. Those velocity changes are not the same along the bridge (as observed in figure 4.4), which indicates possible spatial variations in mass and stiffness distributions as a function of the stress conditions. However, a quantitative analysis is required to relate relative velocity changes and frequency shifts of standing waves to the intrinsic physical properties of the concrete bridge.

The stress-dependency of elastic properties is regarded as a Classical Nonlinear Elastic effect. As observed in this investigation, this effect might not be intrinsic to the wave propagation phenomena but to the inherent physical properties of the material since both travelling and standing waves can be used to observe the linear dependency at different scales (Chapter 2, Figure 2.4 for the material scale, and Figure for the structural scale). This classical nonlinear effect was demonstrated to be higher in damaged concrete samples under some circumstances. As thoroughly explained in Chapters 2 and 3, this depends on the density of microstructures, their orientation, and

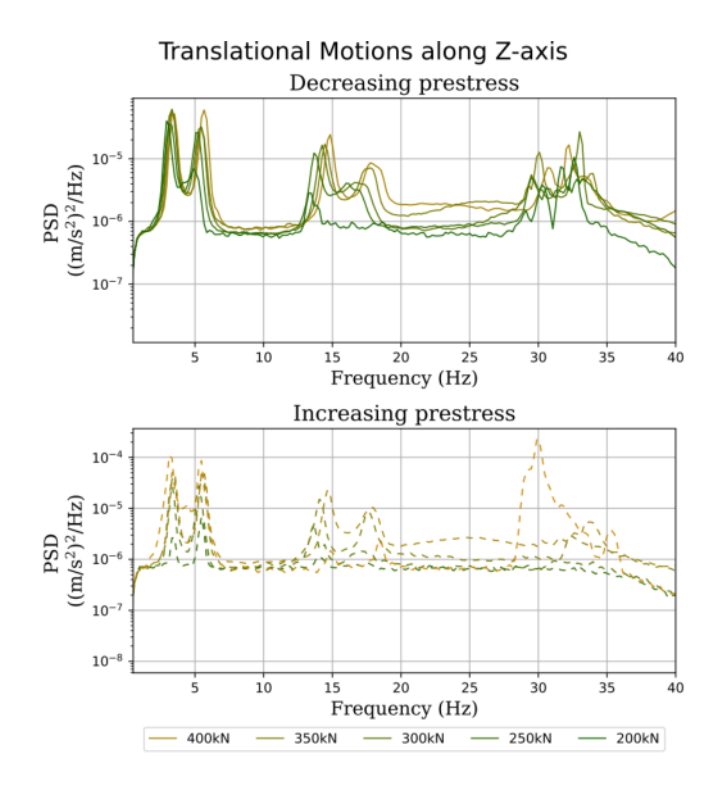


Figure 4.8: Variation of PSD with respect to frequency measured with the vertical component of the IMU50 sensor

the polarisation direction of the travelling wave. Those conditions are challenging to assess for standing waves that embody the dynamics of the bridge at the structural scale. Further investigations are needed to evaluate the integrity level of the structure using the acoustoelastic effect calculated with standing waves.

#### Analysis of stress-dependent coda wave decay 4.4

The second component of this low-frequency data analysis is focused on the capacity of concrete to attenuate or preserve mechanical energy, specifically, the energy of the coda waves originating from the action of the vertical impulsive sources. Analysing the attenuation by means of the amplitude decay of the coda waves requires a methodology that describes such attenuation phenomenon as a function of energy dissipation and geometrical spreading, independently of the source features, the path propagation, and the local amplification effects (Aki, 1969).

#### 4.4.1 The Coda Q model and estimation for a concrete structure

Aki and Chouet 1975 (Aki and Bernard, 1975) proposed two models for back-scattered waves to quantify the amplitude decay of coda by using the coda quality factor Q; the single scattering and multiple scattering (also known as diffusion) models. In this work, the single scattering model is used. This model considers the attenuation of seismic waves as the sum of intrinsic and scattering attenuation, where in the first case the energy is converted to heat through anelastic absorption and in the second case it is redistributed through refraction, reflection and diffraction at random discontinuities

present in a homogeneous medium (Kumar et al., 2005). In the analysis of small local earthquakes, the dimensionless Q factor was observed to be frequency-dependent (Mitchell, 1981), and can be expressed as in equation 4.6. The amplitude of a seismic signal A at a frequency around  $\omega$  over a time t is expressed by a source term c, which is constant for a uniform excitation. The constant a accounts for geometrical spreading, where a = 1 is generally assumed for body waves. For the sake of practicality, this assumption is used in this experiment.

$$A(\omega|t) = ct^{-a}e^{-\omega t/2Q} \tag{4.6}$$

As the geophones were attached to the surface of the concrete structure using plaster, it is assumed no energy loss due to sensor-structure coupling issues. Equation 4.6 can be reformulated by replacing  $\omega$  with the frequency f, around which the signal is filtered.

$$A(f|t) = ct^{-a}e^{-\pi ft/Q}$$
(4.7)

By transforming this equation, the right side of equation 4 can be interpreted as a linear function with a negative slope of  $\pi f/Q$ . It must be noted that quality factor Q is inversely proportional to attenuation (Diewald et al., 2024).

$$\ln\left[A\left(f|t\right)t\right] = \ln c - \frac{\pi f}{O}t\tag{4.8}$$

The procedure for deriving Q for the concrete structure is illustrated in Figure 4.9. At every compressive force level, six VIS were triggered on the bridge (three at the north span and three at the south, as indicated in Chapter 2). All twelve geophones placed on top of the bridge recorded the effect of such VIS. Figure 4.9a plots the raw data recorded at the G 01 at a compressive force level of 400 kN, and the six VIS highlighted with green segments. The raw time series was filtered at a frequency band of  $F_{min} = 0.8 \times F_c$  and  $F_{min} = 1.2 \times F_c$ , where  $F_c$  equals the fundamental frequency of the beam  $F_c = 3.76$ . The absolute values of the amplitude of each filtered event are the basis for linear regression (the red colour line in figures 4.9b to 4.9g), starting from 1.5 seconds after the maximum amplitude of the filtered signal. Once the linear regression is performed, the Q value can be estimated via equation 4.8 for the given central frequency.

#### 4.4.2 Discussion on the Coda Q analysis

The frequency-dependency of Q for data recorded in reinforced concrete is analysed and plotted in Figure 4.10 for Q(3.76). This figure plots a set of four values for Q at f = 3.76 since the maximum and minimum values were regarded as outliers and, therefore, removed. For analyses of data recorded in the Earth's structure, the Q factor is demonstrated to increase with frequency through the relation:

$$Q = Q(0) \left(\frac{f}{f_0}\right)^n,\tag{4.9}$$

where  $Q_0$  is the quality factor at the frequency  $f_0$  (generally 1 Hz) and n is the frequency parameter, which is close to 1 and varies from region to region on the basis of heterogeneity of the medium (Aki, 1981).

In this investigation, Q values were calculated at eight higher frequency bands dictated by central frequencies in Figure 4.10. Those central frequencies were selected

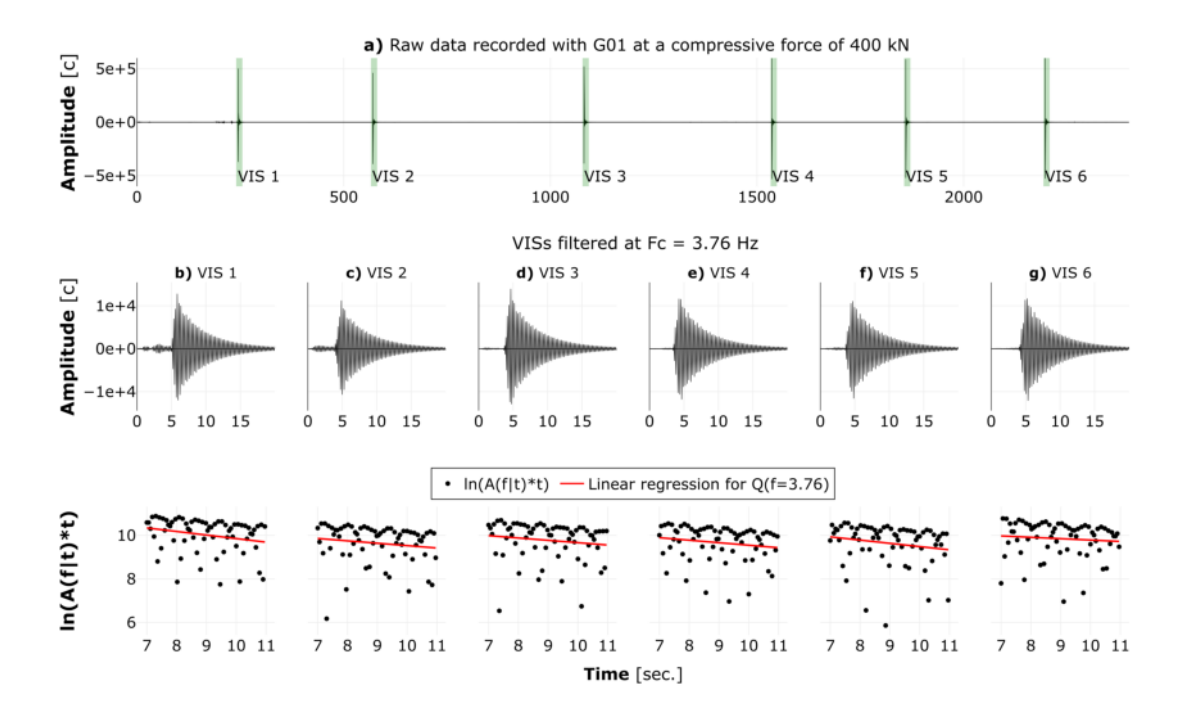


Figure 4.9: Procedure to estimate the quality factor Q using the six vertical impulsive sources (VISs) recorded at the geophone 01 when the structure was compressed with 400 kN. a) plots the raw data and the six VISs highlighted in green. Panels from b) to g) plot the VISs filtered around the central frequency f of 3.76 Hz, and their corresponding approximation for Q according to equation 4.8, which is the slope of the linear regression (in red) using the absolute value of the signal amplitude A for a constant f.

considering the eigenfrequency analysis results in Figure 4.1. The results in Figure 4.10 (and section A.3) show that the Q values tend to increase as the frequency increases. The red line shows that this increment is hardly linear, as expected from the equation for *n* close to 1, since the Q values are highly scattered around the linear model. The Q values estimated at frequencies of 15 Hz and 18 Hz tend to deviate more from the expected linear increment; such frequencies correspond to the second and third higher harmonics of the beam reported in the eigenfrequency analysis.

The estimation of Q(3.76Hz) at each sensor on the bridge at every compressive force was carried out and is observed in Figure 4.11. This figure shows the stress-dependency of the averaged quality factor Q at the fundamental frequency of the beam of 3.76Hz, at all twelve geophones. The quality factor shows no systematic evolution as a function of stress, as observed in the dv/v analysis Figure 4.6. However, the estimations suggest that quality factors tend to be slightly higher when decompressing the structure (from 370 D to 280 D plotted with dots) than when compressing the structure (from 310 C to 400 C plotted with crosses) at most geophone places.

To elaborate on the spatial changes of the quality factor, Figure 4.12 plots the different Q(3.76Hz) values estimated along the bridge at the highest and the lowest compressive force levels. Figure 4.12a plots the average Q(3.76 Hz) value estimated at each sensor for a compressive force of 400 kN. At this compressive force, Q oscillates between 98 and 108 units observed at geophone G 08 and geophone G 05, respectively. According to these results, the vertical supports of the bridge have no influence on the attenuation

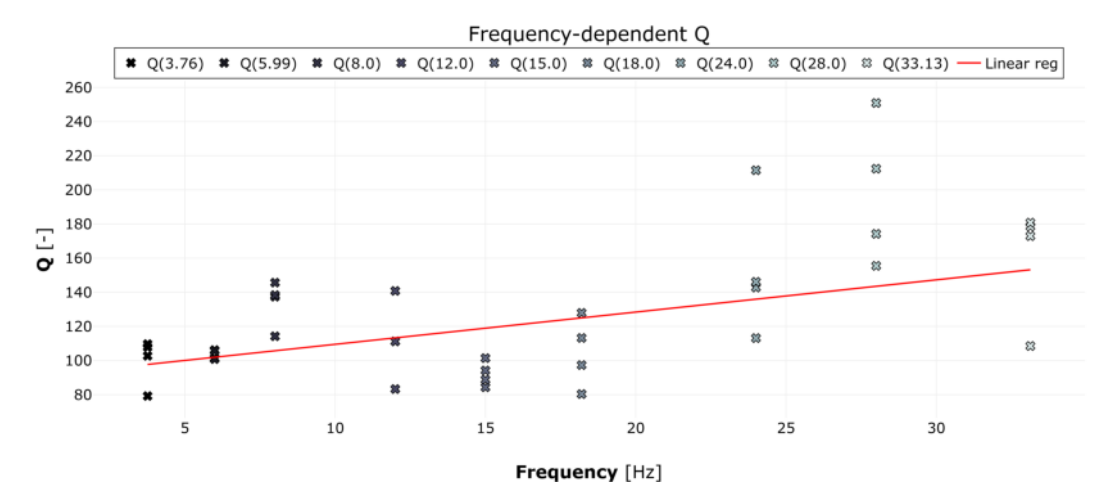


Figure 4.10: The frequency-dependency of coda Q estimated at station G 01 at a compressive force level of 400 kN. On the vertical axis, the estimated Q values are shown for nine different central frequencies indicated on the horizontal axis. Each central frequency plots the set of four values, which correspond to the six VISs, removing the outliers (maximum and minimum Q values)

processes (intrinsic or scattering attenuation) of mechanical waves at this frequency band. Qualitatively, the south span (from G 02 to G 05) shows less variability than in the north (from G 07 to G 11). At the lowest compressive force level (Figure 4.12b), the effect of the vertical supports is still not observed. However, the quality factors on the north span increased with respect to the initial compressive force level. In contrast, the quality factors estimated in the south span at the lowest compressive force level remained, broadly speaking, unchanged.

#### 4.5 Conclusions

This section investigated the performance of low-frequency conventional seismological equipment and data processing techniques to measure and track the evolution of dynamic elastic behaviour of a concrete structure through two analyses: I) relative velocity changes and II) Coda wave decay.

Although the operational range of this type of equipment is limited, and it does not properly sense all wave propagation phenomena occurring within the structure, this operational range is suitable for sensing standing waves on the structure and tracking their evolution as a function of stress. Dense arrays of low-frequency equipment are helpful since they measure the local features of standing oscillations in the concrete structure.

I) Relative velocity changes: The stress-dependent evolution of the bridge's fundamental standing wave was manifested as decreases in the velocity at which this fundamental wave oscillates—the lower the compressive force level, the lower the velocity of oscillation. These decreases varied in magnitude across different positions on the bridge.

The changes in the velocity of oscillations follow a linear function with respect to the compressive force level, exhibiting similarities with the acoustoelastic effect, which explains the evolution of elastic wave speeds as a function of the stress state of the material (Pao and Gamer, 1985). Such an effect has been widely studied using different modes of travelling waves, and now it is observed using standing waves all

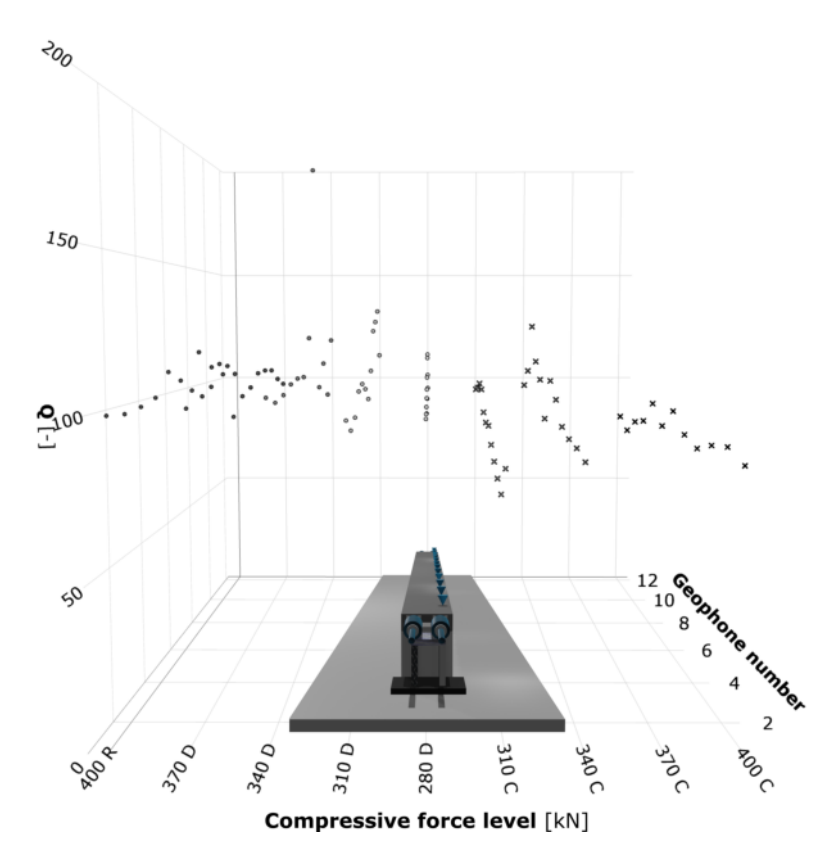


Figure 4.11: Stress-dependent quality factor (Q) estimated at a central frequency of 3.76 Hz at all twelve geophones placed along the bridge. The Z-axis represents the Q (the dimensionless inversely proportional quantity to attenuation), the X-axis represents the compressive force level (400 kN as a Reference state, and the subsequent seven deformed states at Decompression and Compression), and the Y-axis represents the geophone number (from G 01 to G 12 corresponding to the twelve inverted blue cones placed on the surface of the bridge). Dots correspond to Q estimations during decompression, and crosses correspond to estimations during compression.

along the structure using conventional seismic equipment. This observation suggests that the acoustoelastic effect is defined by the change in the properties of the structure (geometrical or material properties) and can be sensed regardless of the nature of the sensing wave (high-frequency travelling waves or low-frequency standing waves). This study opens the door to investigating the relationship between the acoustoelastic effect and the integrity level of the structure via standing waves, leveraging their sensitivity to mass and stiffness changes.

The main pillars of this investigation regarding data processing techniques are the Coda Wave Interferometry Stretching Technique and the Autocorrelation Functions. Both methodologies are borrowed from seismology and have proven to be suitable tools for monitoring changes not only in Earth's subsurface structures but also at the structural scale in civil constructions.

II) Coda wave decay: The coda wave decay of external sources at the fundamental standing wave's frequency band exhibited no systematic behaviour in this experiment. Further experimentations are needed to investigate the suitable parametrisation of the single scattering model (e.g., a, n, and  $f_0$  in equations 4.7 and 4.9) for data recorded in concrete structures at low-frequency bands. Some alternatives can be considered to investigate attenuation processes in concrete structures and their dependence on stress or

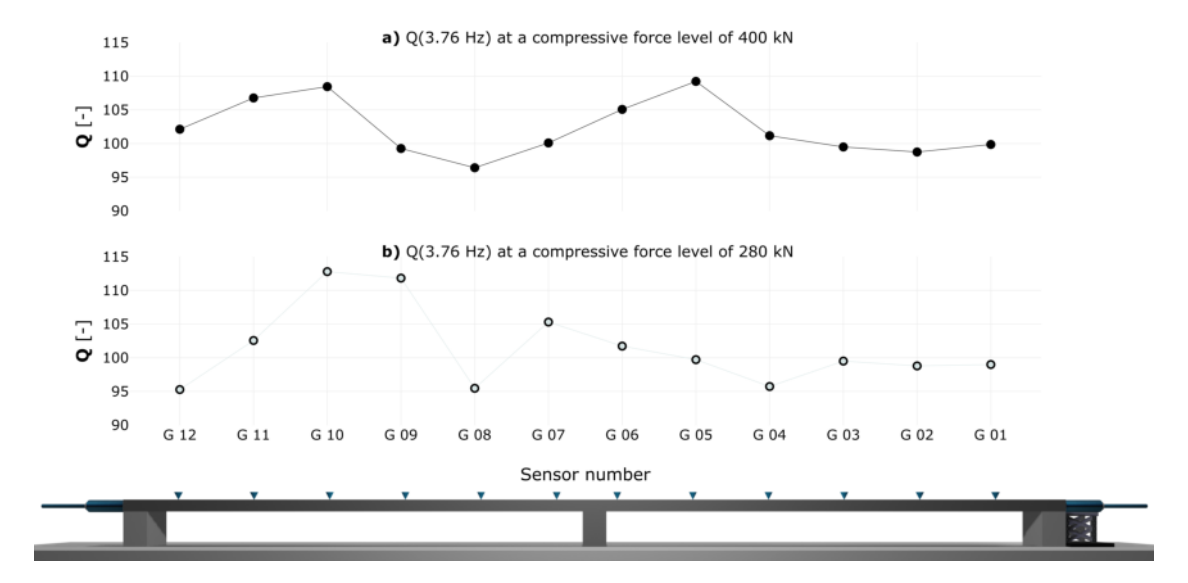


Figure 4.12: The average quality factor (Q) estimated at a central frequency of 3.76 Hz at all twelve geophones placed along the bridge. a) Quality factors estimated at the beginning of the experiment at a compressive force level of 400 kN (the highest level), and b) at a compressive force level of 280 kN (the lowest level).

time. For instance, (1) analysing coda wave decay from vertical impulsive sources using multiple scattering models and (2) estimating attenuation in standing waves through structural damping effects, which would require the calculation of mode shapes.

## Conclusions and outlook

## 5.1 Conclusions

The objective of this thesis is to investigate the presence of nonlinear elastic effects in a concrete structure under outdoor conditions and their seeming relationship with its relative integrity level. This is achieved by leveraging the sensing and data processing techniques developed in the seismology area and rock mechanics. To this end, an experiment was conducted in a field-conditioned concrete structure to analyse the systematic evolution of its elastic properties as a function of stress (the classical nonlinear elastic effects), and time (the nonclassical nonlinear elastic effects). This systematic evolution was monitored across different temporal scales, ranging from the ultrasonic to low-frequency measurements.

Chapter 2 of this thesis presents the experimental setup in detail, including the stress protocol, theoretical background, and applied methods. The findings indicate that both classical and nonclassical nonlinear elastic phenomena—specifically, the acoustoelastic effect and Slow Dynamics—can be induced in a field-conditioned concrete structure using mechanical perturbations such as prestressing systems and vertical impulsive sources. These effects can be effectively monitored and quantified using data processing procedures adapted from seismology, such as wave interferometry. By comparing measurements of acoustoelastic effects and Slow Dynamics with standard Ultrasound Pulse Velocity (UPV) assessments, a relationship between these nonlinear elastic behaviors and the integrity level of the concrete emerges. The results suggest that soft microstructures may be the underlying physical mechanism responsible for the observed variations in structural integrity.

Previous investigations into the complex phenomenon of Slow Dynamics have led to the development of models that describe its nature in terms of various physical processes and phenomenological variables. These models are presented in Chapter 3. Building on one of them, an analytical expression was developed to model the stress-dependent behaviour of Slow Dynamics in concrete with varying integrity levels. The results confirm the findings of Chapter 2 through a probabilistic data inversion process, establishing a relationship between elastic softening (a component of Slow

Dynamics) and a time-dependent, non-stationary linear effect, both of which correlate with the integrity level of the concrete. In addition, this chapter analyses the temporal evolution of the energy content of the ultrasound signal to explore the physical processes underlying Slow Dynamics. The analysis reveals dissipative processes occurring in concrete with both high and low integrity levels during the Slow Dynamics phases. This observation supports the hypothesis that the opening and closing of microcracks is a plausible physical mechanism responsible for the observed behaviour.

The final chapter shifts focus to low-frequency analysis and investigates the stress dependence of attenuation and velocity variations at the structural scale, using the fundamental standing wave mode of the bridge. The attenuation, assessed through coda wave decay, showed no systematic relationship with the level of compressive force applied to the bridge. In contrast, the acoustoelastic effect, estimated using autocorrelation functions of the fundamental standing wave of the bridge, suggests a potential theoretical relationship between this classical nonlinear elastic effect and the spatial distribution of mass and stiffness within the bridge structure.

Overall, the findings reveal that:

- Nonlinear elastic effects can be induced in field-conditioned concrete structures at both the material and structural scales;
- These effects can be measured using standard data processing techniques and instruments developed in the field of seismology;
- Such measurements are physically meaningful and can be correlated with assessments conducted using standardised nondestructive testing techniques, such as Ultrasound Pulse Velocity (UPV).

The outcomes of this experimentation, performed in *outdoor conditions*, are in qualitative agreement with extensive studies conducted under *laboratory conditions*. Additionally, they provide valuable insights that could serve as guidelines for future investigations into nonlinear elastic effects in field-conditioned concrete structures, particularly for early-stage damage assessment.

## 5.2 Outlook

To point towards future research directions, it is important to acknowledge the limitations of the present study. Nonlinear elastic phenomena in concrete become evident when the evolution of its elastic properties is monitored with high precision over time and under varying stress conditions. As shown in this work, the progression of these properties differs between damaged and undamaged samples. When monitoring concrete structures in outdoor environments, numerous external factors can influence the internal stress distribution. These uncontrolled variables may obscure the effects of deliberate mechanical stress inputs, such as prestressing or vertical impulsive sources. As a result, the relationship between nonlinear elastic responses and the structural integrity of concrete can become difficult to interpret. Studying those variables is essential for advancing the practical implementation of this monitoring approach.

It is therefore recommended that future investigations be conducted in situ to monitor effects such as:

- Temperature: It was observed that temperature generally has a linear relationship with changes in wave propagation velocity. However, the behaviour of this relationship remains unexplored when different portions of the waveform are used to estimate relative velocity changes. Therefore, exploring thermal effects in in-situ concrete structures across varying time windows may help calibrate the recordings for damage assessment, enabling more precise removal of temperature-related influences. Additional research topics related to thermal effects must include the impact of sunlight and air temperature on in-situ concrete structures, as well as the changes in their elastic properties induced by these environmental factors.
- Humidity and water content: Water is an active and fundamental constituent of concrete. It plays a crucial role during the hardening process, and its content in in-situ concrete structures tends to vary, primarily due to seasonal factors such as rainfall. Investigating relative velocity changes as a function of water content in aged concrete structures is, therefore, of considerable importance.

Since the long-term goal is to incorporate measurements of such nonlinear elastic effects into wavefield-based techniques for damage assessment—and to develop these into standardised methods—extensive experimental work is still required under field conditions in concrete structures. A starting point could involve variations from the current experimental setups, such as the following:

- Studying the time dependence of compressive force changes and vertical impulsive sources separately: This means separating the concrete's response to static and dynamic mechanical perturbations. Doing so will improve the identification and characterisation of creep and slow dynamics effects in concrete structures under field conditions.
- Anisotropy measurements in situ: Anisotropic elastic effects are generally difficult
  to study under in-situ conditions, as they require complex experimental setups.
  However, analysing anisotropy measurements of nonlinear elastic effects could
  represent significant progress in revealing the underlying physical microstructures
  responsible for nonlinearity in concrete. Such analyses may also provide insights
  into the dynamics, spatial distribution, and preferred orientation of microstructures within the concrete structure.
- Stress measurements (static measurements with strain gauges or DSS measurements): Measuring stress during the experiment is essential not only to detect structural effects such as deflections or bending occurring in the structure, but also to explore their impact on measurements at the material scale. As discussed in Chapter 3, slow dynamics may be influenced by a varying, non-stationary linear effect, the variability of which is speculated to originate from structural factors.
- Better definition of relaxation time scales: Increasing the sampling frequency of the ultrasound acquisition system in future experiments with similar stress protocols leads to more precise measurements of the minimum relaxation time scales in concrete (see Chapter 3, Section 3.2.2 for clarification on this topic). Additionally, extending the duration of measurements during relaxation processes

would help better define the maximum relaxation time scales in in-situ concrete structures.

• Testing the energy dependence of slow dynamics: It would be valuable to induce slow dynamics effects using different types of impulsive sources with varying energy levels. This helps to investigate a relationship between the integrity level of the concrete and the amount of energy introduced into the structure.

Linking nonlinear elastic effects to structural integrity: To investigate the relationship between nonlinear elastic effects estimated at the structural scale and the integrity level of the structure, it is essential to establish a quantitative correlation between changes in the oscillation velocity of standing waves, frequency shifts, and their connection to damping effects, as well as mass and stiffness distributions. In this context, joint studies combining modal analysis with relative velocity changes under varying stress conditions are necessary. The use of six-degree-of-freedom sensors (rotational sensors and accelerometers) is suitable for validating and enhancing these joint analyses.

Validation is essential for advancing the integration of nonlinear elastic effects into Nondestructive Testing (NDT) methodologies. In this context, assessing the repeatability of results is a fundamental step. It is recommended to perform tests with similar setups to validate the relationship between nonlinear elastic effects and the intrinsic physical state of concrete. Additionally, comparing these results with those obtained from standard NDT methods, which assess different physical properties of concrete, is crucial for identifying the presence of damage or imperfections with less uncertainty.

Appendices



# Additional Material

## A.1 Pictures of the experiment



Figure A.1: The BLEIB structure



Figure A.2: The placement of the seismic equipment



(a) Six-degree-of-freedom sensors covered with grey boxes and one-component geophones attached to the bridge's surface with plaster.



(b) The prestressing system of the BLEIB structure that compresses the structure in its longitudinal direction.

Figure A.3: The equipment used in the experiment

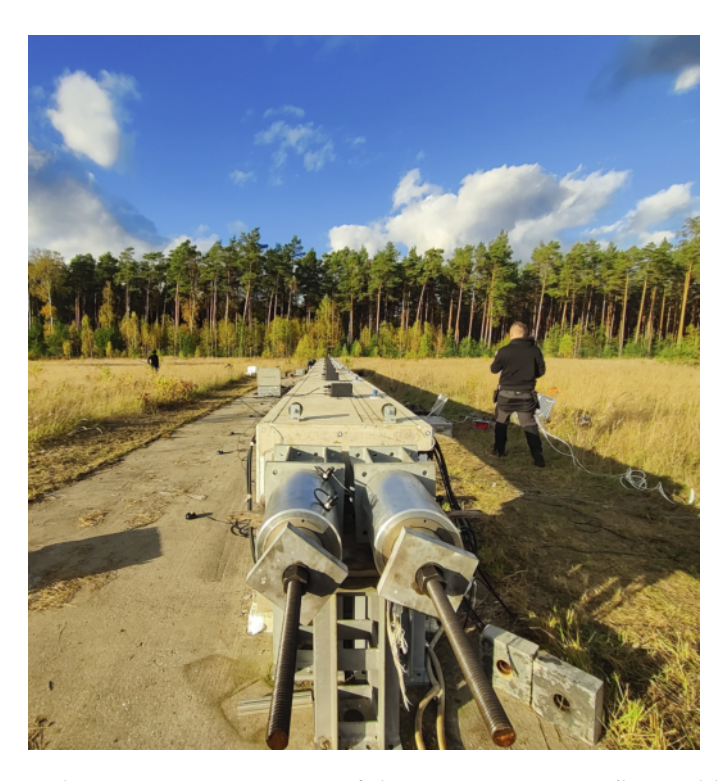
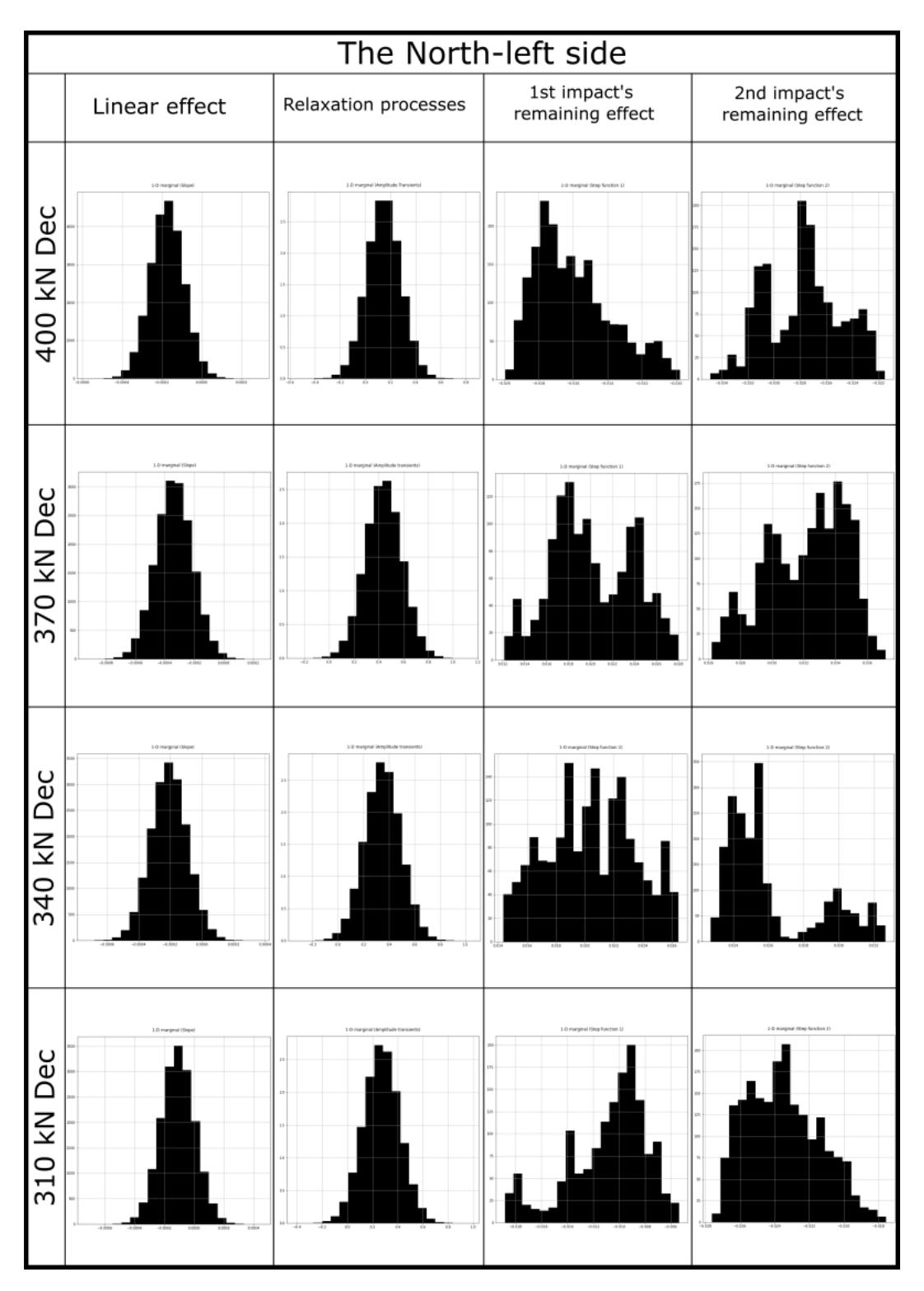


Figure A.4: The prestressing system of the BLEIB structure (by Nicklas Epple)

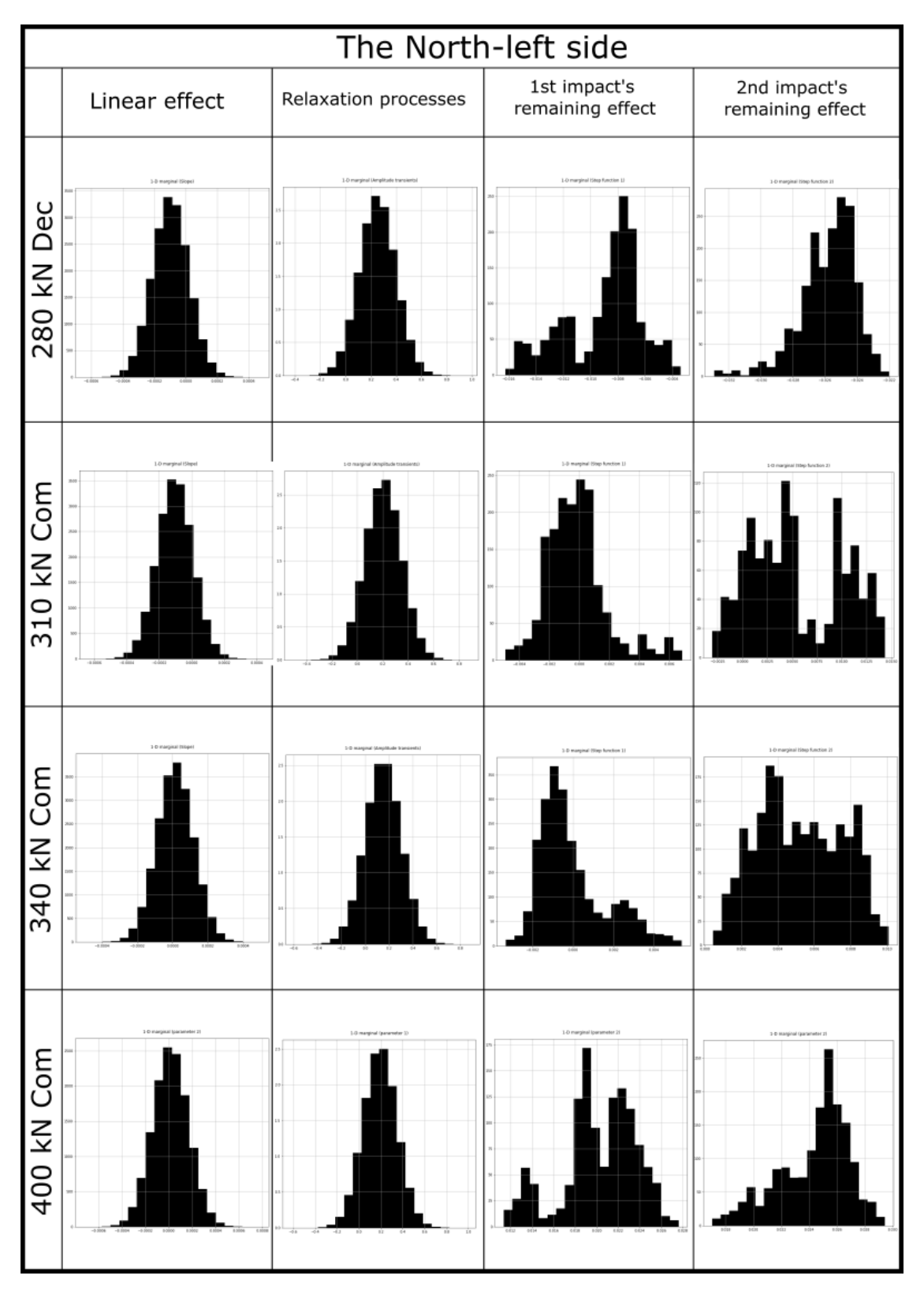


Figure A.5: The triggering of the Vertical Impulsive Source on the North span bridge (by BAM)

## A.2 Probabilistic inversion processes



**Figure A.6:** Histograms of the data inversion process for the North left side (from 400 kN Decompression to 310 kN Compression)



**Figure A.7:** Histograms of the data inversion process for the North left side (from 280 kN Decompression to 400 kN Compression)

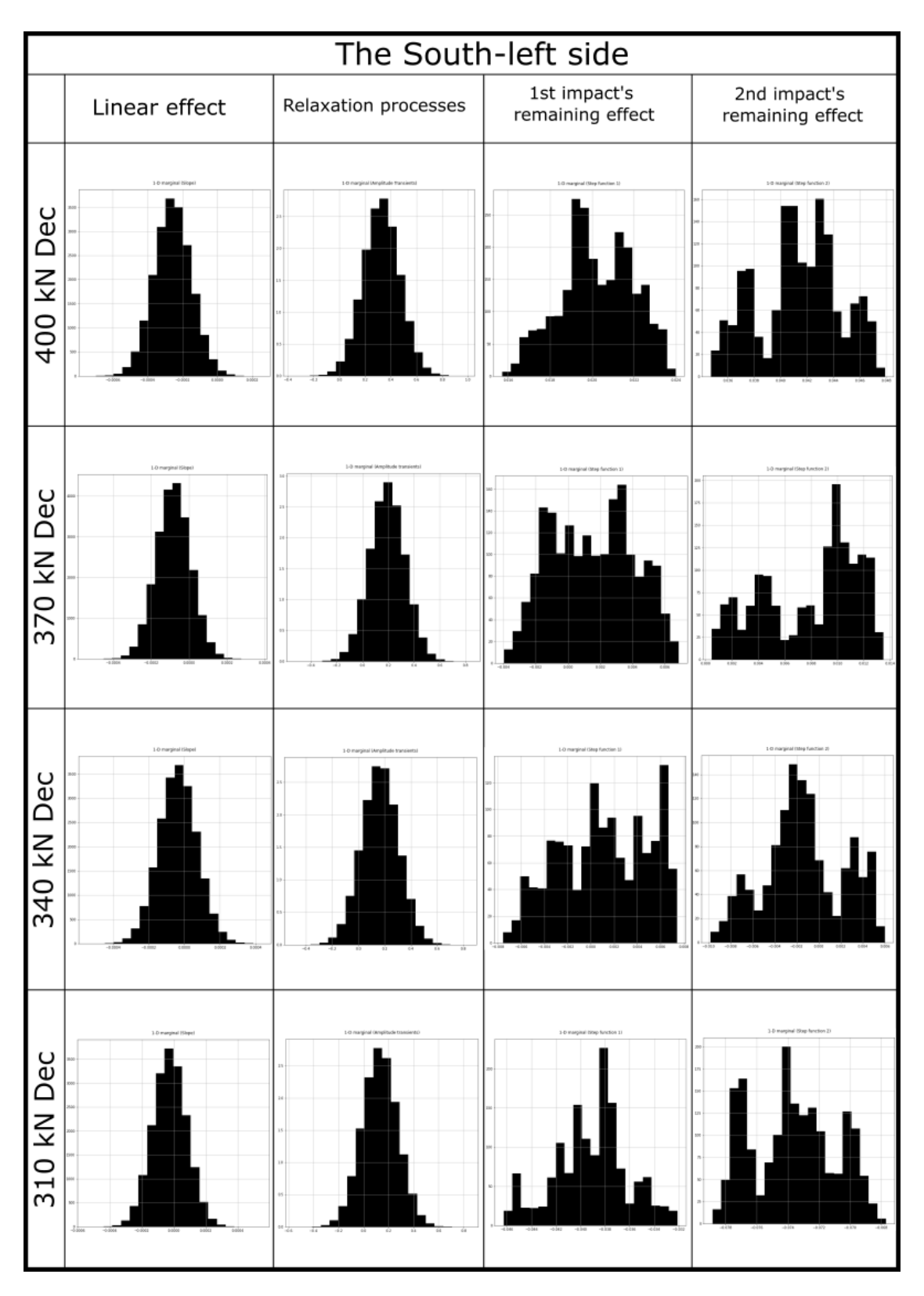


**Figure A.8**: Histograms of the data inversion process for the South left side (from 400 kN Decompression to 310 kN Compression)

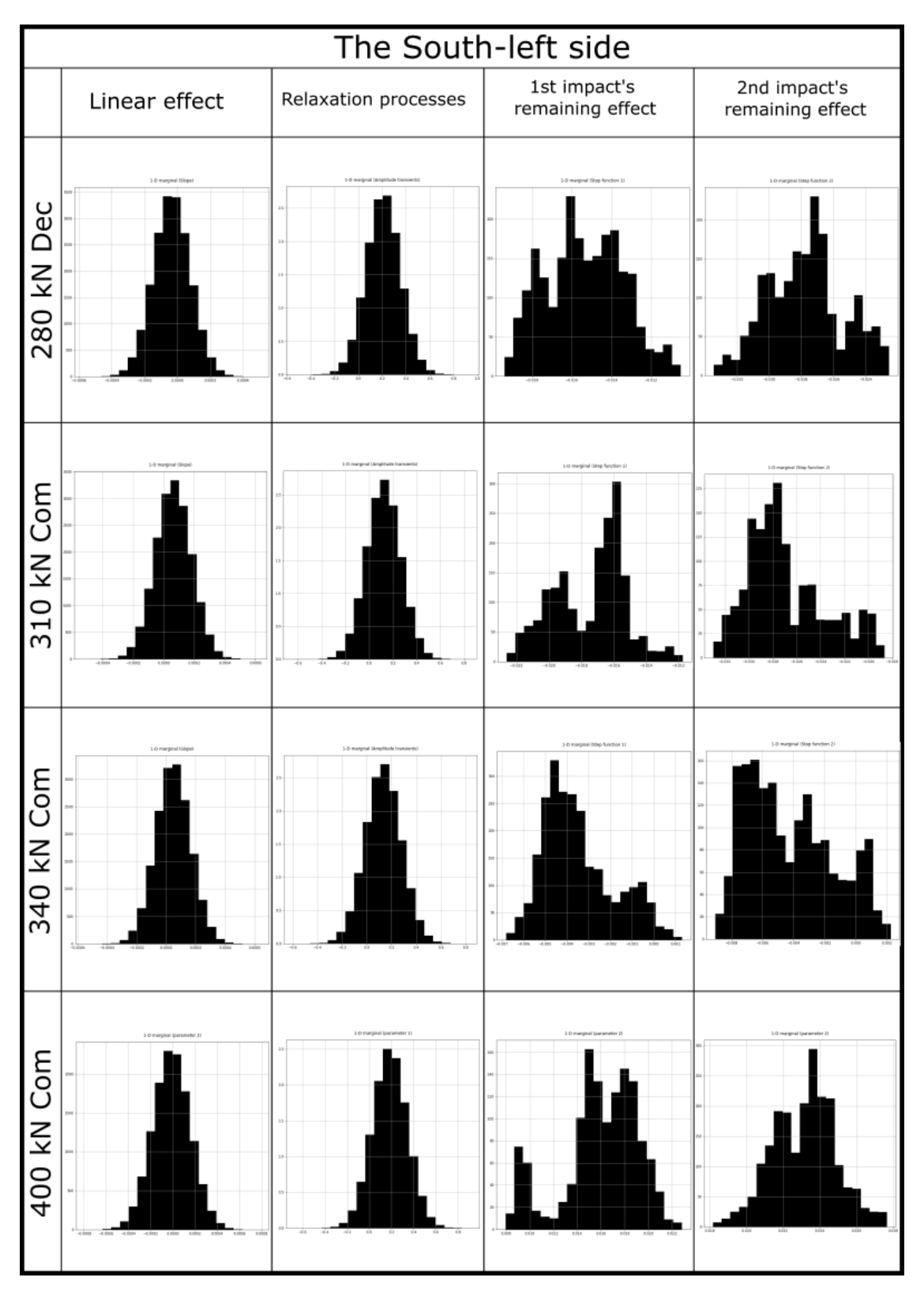


Figure A.9: Histograms of the data inversion process for the South left side (from 280 kN Decompression to 400 kN Compression)

## A.3 Coda Q as a function of frequency

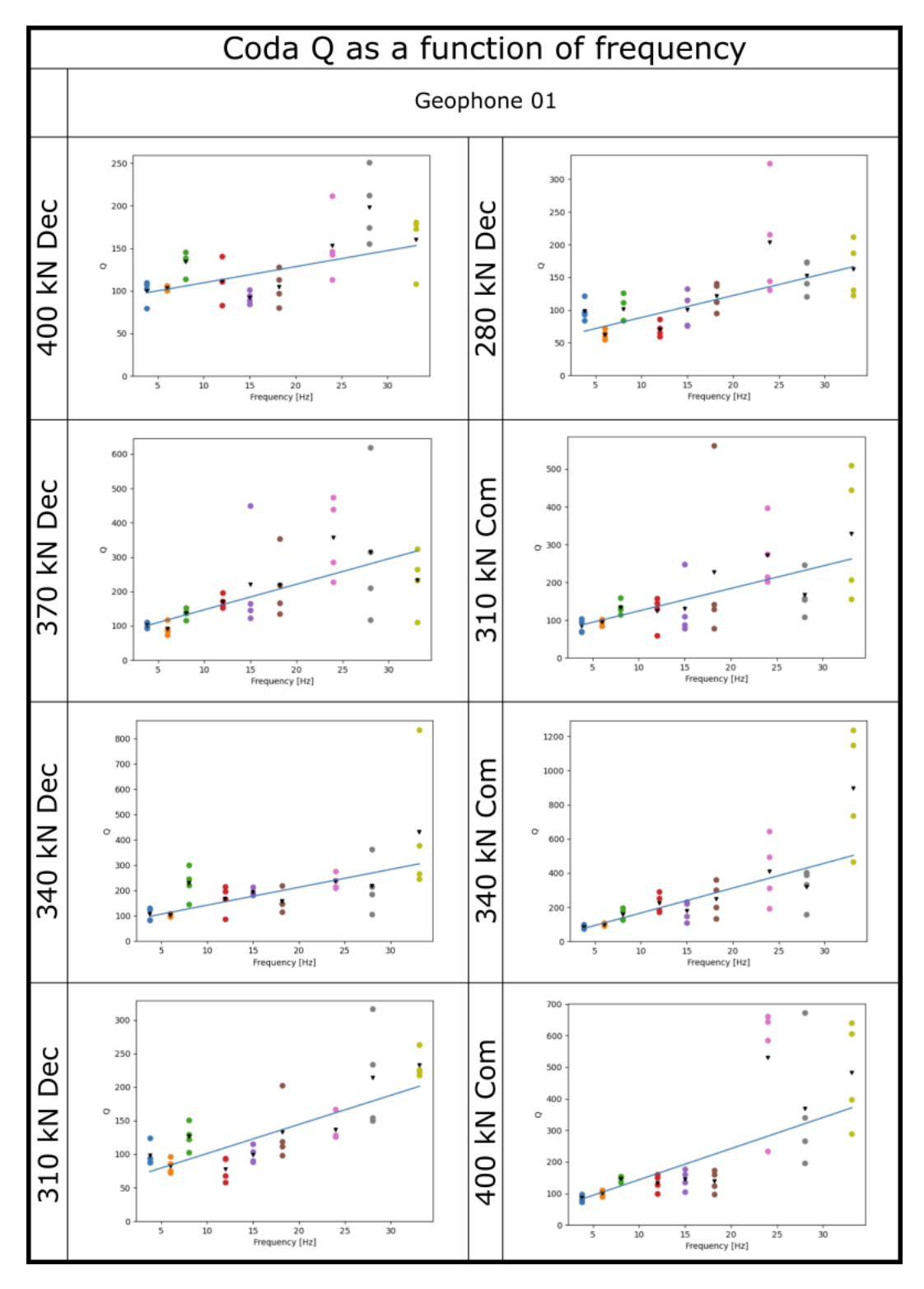


Figure A.10: Coda Q analysis at Geophone 01

- Keiiti Aki. 1969. Analysis of the seismic coda of local earthquakes as scattered waves. *Journal of geophysical research* 74 (2): 615–631. (Cited on page 64).
- ——. 1981. Source and scattering effects on the spectra of small local earthquakes. *Bulletin of the Seismological Society of America* 71 (6): 1687–1700. (Cited on page 65).
- Keiiti Aki and Chouet Bernard. 1975. Origin of coda waves: source, attenuation, and scattering effects. *J. Geophys. Res.* 80 (23). (Cited on page 64).
- V Aleshin and K Van Den Abeele. 2007. Friction in unconforming grain contacts as a mechanism for tensorial stress-strain hysteresis [in en]. *J. Mech. Phys. Solids* 55, no. 4 (April): 765–787. (Cited on page 34).
- Benjamin Ankay and Chuanzeng Zhang. 2019. Acoustoelastic evaluation of ultra-high performance concretes. 45th Annual Review of Progress in Quantitative Nondestructive Evaluation, Volume 38 2102 (1): 110002. (Cited on pages 5, 11).
- Manuel Asnar, Christoph Sens-Schönfelder, Audrey Bonnelye, Andrew Curtis, Georg Dresen, and Marco Bohnhoff. 2025. Anisotropy reveals contact sliding and aging as a cause of post-seismic velocity changes, (cited on pages 3, 7, 11, 17, 22, 29, 36).
- ASTM Test Designation C 597-02, Standard Test Method Pulse Velocity through Concrete. n.d. Annual Book ASTM Standards. (Cited on page 15).
- Ariana Astorga and Philippe Guéguen. 2020. Structural health building response induced by earthquakes: Material softening and recovery [in en]. *Engineering Reports* 2, no. 9 (September). (Cited on page 7).
- Ariana Astorga, Philippe Guéguen, and Toshihide Kashima. 2018. Nonlinear elasticity observed in buildings during a long sequence of earthquakes. *Bulletin of the Seismological Society of America* 108 (3A): 1185–1198. (Cited on page 11).
- Mourad Bentahar, Angelo Di Bella, Charfeddine Mechri, Silvio Montresor, Marco Scalerandi, and Xiaoyang Yu. 2020. Exploiting slow dynamics effects for damage detection in concrete. *Frontiers in Built Environment* 6:64. (Cited on pages 7, 11, 22 sq.).
- H Berjamin, N Favrie, B Lombard, and G Chiavassa. 2017. Nonlinear waves in solids with slow dynamics: an internal-variable model [in en]. *Proc. Math. Phys. Eng. Sci.* 473, no. 2201 (May): 20170024. (Cited on pages 7, 33).
- Harold Berjamin, Bruno Lombard, Guillaume Chiavassa, and Nicolas Favrie. 2019. Plane-strain waves in nonlinear elastic solids with softening [in en]. *Wave Motion* 89 (June): 65–78. (Cited on page 33).
- Santiago Bertero, Pablo A Tarazaga, and Rodrigo Sarlo. 2022. In situ seismic testing for experimental modal analysis of civil structures [in en]. *Eng. Struct.* 270, no. 114773 (November): 114773. (Cited on page 55).

Moritz Beyreuther, Robert Barsch, Lion Krischer, Tobias Megies, Yannik Behr, and Joachim Wassermann. 2010. ObsPy: A Python toolbox for seismology. *Seismological Research Letters* 81 (3): 530–533. (Cited on page 15).

- Francis Birch and Dennison Bancroft. 1938. The effect of pressure on the rigidity of rocks. II. *J. Geol.* 46, no. 2 (February): 113–141. (Cited on page 3).
- J A Bittner and J S Popovics. 2021. Mechanistic diffusion model for slow dynamic behavior in materials [in en]. J. Mech. Phys. Solids 150, no. 104355 (May): 104355. (Cited on pages 7, 34).
- Luis Fabian Bonilla, Philippe Guéguen, and Yehuda Ben-Zion. 2019. Monitoring coseismic temporal changes of shallow material during strong ground motion with interferometry and autocorrelation. *Bulletin of the Seismological Society of America* 109 (1): 187–198. (Cited on page 56).
- Nicolas Brantut and Léo Petit. 2022. Micromechanics of rock damage and its recovery in cyclic loading conditions [in en]. *Geophys. J. Int.* 233 (1): 145–161. (Cited on page 7).
- Alexis Cartwright-Taylor, Maria-Daphne Mangriotis, Ian G Main, Ian B Butler, Florian Fusseis, Martin Ling, Edward Andò, Andrew Curtis, Andrew F Bell, Alyssa Crippen, Roberto E Rizzo, Sina Marti, Derek D V Leung, and Oxana V Magdysyuk. 2022. Seismic events miss important kinematically governed grain scale mechanisms during shear failure of porous rock [in en]. *Nat. Commun.* 13, no. 1 (October): 6169. (Cited on page 3).
- Jean-Francois Chaix, Ivan Lillamand, Marie-Aude Ploix, Vincent Garnier, and Gilles Corneloup. 2008. Study of acoustoelasticity behavior of concrete material under uniaxial compression. In *Proceedings of Meetings on Acoustics*, vol. 4. 1. AIP Publishing. (Cited on page 10).
- Jean-François Chaix, Ivan Lillamand, Marie-Aude Ploix, Vincent Garnier, and Gilles Corneloup. 2008. Study of acoustoelasticity behavior of concrete material under uniaxial compression [in en]. J. Acoust. Soc. Am. 123, no. 5\_Supplement (May): 3847–3847. (Cited on page 4).
- In-Chul Choi, Byung-Gil Yoo, Yong-Jae Kim, and Jae-il Jang. 2012. Indentation creep revisited. *Journal of Materials Research* 27 (1): 3–11. (Cited on page 24).
- A.K. Chopra. 2007. Dynamics of Structures: Theory and Applications to Earthquake Engineering. Prentice Hall International Series in Civil Engineering And. Pearson/Prentice Hall. (Cited on pages 62 sq.).
- Jon F Claerbout. 1968. Synthesis of a layered medium from its acoustic transmission response. *Geophysics* 33 (2): 264–269. (Cited on page 56).
- Felix Clauß, Niklas Epple, Mark Alexander Ahrens, Ernst Niederleithinger, and Peter Mark. 2022. Correlation of load-bearing behavior of reinforced concrete members and velocity changes of coda waves. *Materials* 15 (3): 738. (Cited on pages 6, 11, 14).
- Raphael S M De Plaen, Andrea Cannata, Flavio Cannavo', Corentin Caudron, Thomas Lecocq, and Olivier Francis. 2019. Temporal changes of seismic velocity caused by volcanic activity at mt. Etna revealed by the autocorrelation of ambient seismic noise. *Front. Earth Sci.* 6. (Cited on page 56).
- Anjali C. Dhabu, Felix Bernauer, Chun-Man Liao, Ernst Niederleithinger, Heiner Igel, and Celine Hadziioannou. 2024. Characterizing Rotational Ground Motions: Implications for Earthquake-Resistant Design of Bridge Structures. arXiv: 2411.02203 [physics.geo-ph]. (Cited on pages 55, 63).

Fabian Diewald, Marine Denolle, Jithender J Timothy, and Christoph Gehlen. 2024. Impact of temperature and relative humidity variations on coda waves in concrete [in en]. *Sci. Rep.* 14 (1): 18861. (Cited on page 65).

- Fabian Diewald, Niklas Epple, Thomas Kraenkel, Christoph Gehlen, and Ernst Niederleithinger. 2022. Impact of External Mechanical Loads on Coda Waves in Concrete [in en]. *Materials* 15, no. 16 (August). (Cited on pages 5, 11, 49).
- Larose Eric and Hall Stephen. 2009. Monitoring stress related velocity variation in concrete with a 2×10-5 relative resolution using diffuse ultrasound [in en]. *J. Acoust. Soc. Am.* 125, no. 4\_Supplement (April): 2641–2641. (Cited on page 4).
- Liberato Ferrara, Tim Van Mullem, Maria Cruz Alonso, Paola Antonaci, Ruben Paul Borg, Estefania Cuenca, Anthony Jefferson, Pui-Lam Ng, Alva Peled, Marta Roig-Flores, et al. 2018. Experimental characterization of the self-healing capacity of cement based materials and its effects on the material performance: A state of the art report by COST Action SARCOS WG2. *Construction and Building Materials* 167:115–142. (Cited on page 24).
- Andreas Fichtner. 2021. Lecture Notes on Inverse Theory (July). (Cited on pages 37, 40).
- M Gassenmeier, C Sens-Schönfelder, T Eulenfeld, M Bartsch, P Victor, F Tilmann, and M Korn. 2016. Field observations of seismic velocity changes caused by shaking-induced damage and healing due to mesoscopic nonlinearity [in en]. *Geophys. J. Int.* 204 (3): 1490–1502. (Cited on page 7).
- Martina Gassenmeier, C Sens-Schönfelder, T Eulenfeld, Mitja Bartsch, Pia Victor, F Tilmann, and M Korn. 2016. Field observations of seismic velocity changes caused by shaking-induced damage and healing due to mesoscopic nonlinearity. *Geophysical Journal International* 204 (3): 1490–1502. (Cited on page 17).
- Farid Ghaffari Moghaddam, Abbas Akbarpour, and Afshin Firouzi. 2022. Dynamic modulus of elasticity and compressive strength evaluations of modified reactive powder concrete (MRPC) by non-destructive ultrasonic pulse velocity method. *Journal of Asian Architecture and Building Engineering* 21 (2): 490–499. (Cited on page 15).
- Samira Gholizadeh. 2016. A review of non-destructive testing methods of composite materials. *Procedia structural integrity* 1:50–57. (Cited on page 10).
- I J Good. 1963. Maximum entropy for hypothesis formulation, especially for multidimensional contingency tables. *Ann. Math. Stat.* 34, no. 3 (September): 911–934. (Cited on page 38).
- Alexei Gorbatov, Erdinc Saygin, and BLN Kennett. 2013. Crustal properties from seismic station autocorrelograms. *Geophysical Journal International* 192 (2): 861–870. (Cited on page 56).
- R A Guyer, K R McCall, and G N Boitnott. 1995. Hysteresis, discrete memory, and nonlinear wave propagation in rock: A new paradigm [in en]. *Phys. Rev. Lett.* 74 (17): 3491–3494. (Cited on page 33).
- Robert A Guyer and Paul A Johnson. 1999. Nonlinear mesoscopic elasticity: Evidence for a new class of materials. *Physics today* 52 (4): 30–36. (Cited on page 10).
- ——. 2009. Nonlinear Mesoscopic Elasticity: The Complex Behaviour of Rocks, Soil, Concrete [in en]. John Wiley & Sons, August. (Cited on pages 3, 10, 22).

Céline Hadziioannou, Eric Larose, Olivier Coutant, Philippe Roux, and Michel Campillo. 2009. Stability of monitoring weak changes in multiply scattering media with ambient noise correlation: Laboratory experiments. *The Journal of the Acoustical Society of America* 125 (6): 3688–3695. (Cited on pages 11, 17).

- Céline Hadziioannou, Éric Larose, Adam Baig, Philippe Roux, and Michel Campillo. 2011. Improving temporal resolution in ambient noise monitoring of seismic wave speed. *Journal of Geophysical Research: Solid Earth* 116 (B7). (Cited on page 11).
- Ali Hafiz and Thomas Schumacher. 2018. Monitoring of stresses in concrete using ultrasonic coda wave comparison technique [in en]. *J. Nondestruct. Eval.* 37, no. 4 (December). (Cited on page 5).
- Se-Hee Hong, Jin-Seok Choi, Tian-Feng Yuan, and Young-Soo Yoon. 2023. A review on concrete creep characteristics and its evaluation on high-strength lightweight concrete [in en]. *J. Mater. Res. Technol.* 22 (January): 230–251. (Cited on page 49).
- D S Hughes and J L Kelly. 1953. Second-Order Elastic Deformation of Solids. *Phys. Rev.* 92, no. 5 (December): 1145–1149. (Cited on page 4).
- Darrell S Hughes and John L Kelly. 1953. Second-order elastic deformation of solids. *Physical review* 92 (5): 1145. (Cited on pages 15 sq.).
- Jiang Jin, Maria Gabriela Moreno, Jacques Riviere, and Parisa Shokouhi. 2017. Impact-based nonlinear acoustic testing for characterizing distributed damage in concrete [in en]. *J. Nondestruct. Eval.* 36, no. 3 (September). (Cited on page 7).
- Elisabeth John and Barbara Lothenbach. 2023. Cement hydration mechanisms through time–a review. *Journal of Materials Science* 58 (24): 9805–9833. (Cited on page 24).
- Paul Johnson and Alexander Sutin. 2005. Slow dynamics and anomalous nonlinear fast dynamics in diverse solids. *The Journal of the Acoustical Society of America* 117 (1): 124–130. (Cited on page 22).
- Robert M Jones. 1977. Stress-strain relations for materials with different moduli in tension and compression. *Aiaa Journal* 15 (1): 16–23. (Cited on page 23).
- Nimrat Pal Kaur, Jay Kumar Shah, Subhra Majhi, and Abhijit Mukherjee. 2019. Healing and simultaneous ultrasonic monitoring of cracks in concrete. *Materials Today Communications* 18:87–99. (Cited on page 24).
- Aakash Khandelwal and Sunil Kishore Chakrapani. 2021. Nonclassical nonlinear elasticity of crystalline structures [in en]. *Phys Rev E* 104, nos. 4-2 (October): 045002. (Cited on pages 6, 11, 22).
- Einar Kjartansson. 1979. ConstantQ-wave propagation and attenuation [in en]. J. Geophys. Res. 84 (B9): 4737. (Cited on page 34).
- Fritz K Kneubühl. 1997. Standing Waves. In *Oscillations and Waves*, 451–478. Berlin, Heidelberg: Springer Berlin Heidelberg. (Cited on page 54).
- Alexander Sergeevich Korolev, Anastasia Kopp, Denis Odnoburcev, Vladislav Loskov, Pavel Shimanovsky, Yulia Koroleva, and Nikolai Ivanovich Vatin. 2021. Compressive and tensile elastic properties of concrete: Empirical factors in span reinforced structures design. *Materials* 14 (24): 7578. (Cited on page 23).

Naresh Kumar, Imtiyaz A Parvez, and H S Virk. 2005. Estimation of coda wave attenuation for NW Himalayan region using local earthquakes [in en]. *Phys. Earth Planet. Inter.* 151, nos. 3-4 (August): 243–258. (Cited on page 65).

- E Larose, N Tremblay, C Payan, V Garnier, and V Rossetto. 2013. Ultrasonic slow dynamics to probe concrete aging and damage. AIP. (Cited on page 7).
- Eric Larose, Julien de Rosny, Ludovic Margerin, Domitille Anache, Pierre Gouedard, Michel Campillo, and Bart van Tiggelen. 2006. Observation of multiple scattering of kHz vibrations in a concrete structure and application to monitoring weak changes [in en]. *Phys. Rev. E Stat. Nonlin. Soft Matter Phys.* 73, no. 1 Pt 2 (January): 016609. (Cited on page 4).
- Eric Larose and Stephen Hall. 2009. Monitoring stress related velocity variation in concrete with a 2× 10- 5 relative resolution using diffuse ultrasound. *The Journal of the Acoustical Society of America* 125 (4): 1853–1856. (Cited on page 11).
- Eric Larose, Anne Obermann, Angela Digulescu, Thomas Planès, Jean-Francois Chaix, Frédéric Mazerolle, and Gautier Moreau. 2015. Locating and characterizing a crack in concrete with diffuse ultrasound: A four-point bending test [in en]. *J. Acoust. Soc. Am.* 138, no. 1 (July): 232–241. (Cited on page 6).
- Eric Larose, Nicolas Tremblay, Cédric Payan, Vincent Garnier, and Vincent Rossetto. 2013. Ultrasonic slow dynamics to probe concrete aging and damage. In *AIP Conference Proceedings*, 1511:1317–1324. 1. American Institute of Physics. (Cited on page 11).
- Krzysztof Łatuszyński, Matthew T Moores, and Timothée Stumpf-Fétizon. 2025. MCMC for multi-modal distributions. *arXiv* [stat.CO], (cited on page 40).
- A Lavrov. 2003. The Kaiser effect in rocks: principles and stress estimation techniques. *International Journal of Rock Mechanics and Mining Sciences* 40 (2): 151171. (Cited on page 5).
- Byung Jae Lee, Seong-Hoon Kee, Taekeun Oh, and Yun-Yong Kim. 2017. Evaluating the dynamic elastic modulus of concrete using shear-wave velocity measurements. *Adv. Mater. Sci. Eng.* 2017:1–13. (Cited on page 54).
- Young Hak Lee and Taekeun Oh. 2016. The measurement of P-, S-, and R-wave velocities to evaluate the condition of reinforced and prestressed concrete slabs [in en]. *Adv. Mater. Sci. Eng.* 2016:1–14. (Cited on page 54).
- Chun-Man Liao and Daniel Fontoura Barroso. 2022. Investigation of temperature effects on ultrasonic velocity in a prestressed concrete bridge model. In *European Workshop on Structural Health Monitoring*, 813–823. Springer. (Cited on page 15).
- Chun-Man Liao, Falk Hille, Daniel Fontoura Barroso, and Ernst Niederleithinger. 2021.

  Monitoring of a prestressed bridge model by ultrasonic measurement and vibration recordings. In 8th International Conference on Computational Methods in Structural Dynamics and Earthquake Engineering Methods in Structural Dynamics and Earthquake Engineering. Athens: Institute of Structural Analysis / Antiseismic Research National Technical University of Athens. (Cited on pages 25, 55).
- Charles K C Lieou, Eric G Daub, Robert E Ecke, and Paul A Johnson. 2017. Slow dynamics and strength recovery in unconsolidated granular earth materials: A mechanistic theory [in en]. *J. Geophys. Res. Solid Earth* 122, no. 10 (October): 7573–7583. (Cited on pages 34, 48).

Ivan Lillamand, Jean-François Chaix, Marie-Aude Ploix, and Vincent Garnier. 2010. Acoustoelastic effect in concrete material under uni-axial compressive loading. *Ndt & E International* 43 (8): 655–660. (Cited on page 10).

- D Linger. 1963. Effect stress dynamic modulus concrete. *Highway Research Record*, no. 3, (cited on page 4).
- Oleg I Lobkis and Richard L Weaver. 2003. Coda-Wave Interferometry in Finite Solids: Recovery of P-to-S Conversion Rates<? format?> in an Elastodynamic Billiard. *Physical review letters* 90 (25): 254302. (Cited on pages 11, 24).
- Tiejiong Lou, Sergio M R Lopes, and Adelino V Lopes. 2015. Neutral axis depth and moment redistribution in FRP and steel reinforced concrete continuous beams. *Compos. B Eng.* 70 (March): 44–52. (Cited on page 49).
- Y Lu and Y Ben-Zion. 2021. Regional seismic velocity changes following the 2019 *M*w 7.1 Ridgecrest, California earthquake from autocorrelations and *P/S* converted waves [in en]. *Geophys. J. Int.* 228 (1): 620–630. (Cited on page 56).
- Vladimir Lyakhovsky, Yehuda Ben-Zion, and Amotz Agnon. 1997. Distributed damage, faulting, and friction. *Journal of Geophysical Research: Solid Earth* 102 (B12): 27635–27649. (Cited on page 23).
- Lyakhovsky, Vladimir and Ben-Zion, Yehuda and Agnon, Amotz. 1997. Distributed damage, faulting, and friction. *J. Geophys. Res. Solid Earth*, (cited on page 33).
- Peter Makus, Marine A Denolle, Christoph Sens-Schönfelder, Manuela Köpfli, and Frederik Tilmann. 2024. Analyzing volcanic, tectonic, and environmental influences on the seismic velocity from 25 years of data at Mount St. Helens. *Seismological Research Letters* 95 (5): 2674–2688. (Cited on page 17).
- Ramón Mata, Rafael O Ruiz, and Eduardo Nuñez. 2023. Correlation between compressive strength of concrete and ultrasonic pulse velocity: A case of study and a new correlation method. *Construction and Building Materials* 369:130569. (Cited on page 15).
- Marc André Meyers and Krishan Kumar Chawla. 2009. Mechanical behavior of materials [in en]. Cambridge, England: Cambridge University Press. (Cited on page 48).
- T Dylan Mikesell, Alison E Malcolm, Di Yang, and Matthew M Haney. 2015. A comparison of methods to estimate seismic phase delays: Numerical examples for coda wave interferometry. *Geophysical Journal International* 202 (1): 347–360. (Cited on page 17).
- Sabbie A Miller, Arpad Horvath, and Paulo J M Monteiro. 2018. Impacts of booming concrete production on water resources worldwide [in en]. *Nat. Sustain.* 1, no. 1 (January): 69–76. (Cited on page 1).
- Brian J Mitchell. 1981. Regional variation and frequency dependence of  $Q\tilde{A}\tilde{Z}\hat{A}^2$  in the crust of the United States [in en]. *Bull. Seismol. Soc. Am.* 71 (5): 1531–1538. (Cited on page 65).
- Mohammad Mohammadhassani, Mohd Zamin Bin Jumaat, Mohamed Chemrouk, Ali Akbar Maghsoudi, Mohammed Jameel, and Shatirah Akib. 2011. An experimental investigation on bending stiffness and neutral axis depth variation of over-reinforced high strength concrete beams [in en]. *Nucl. Eng. Des.* 241, no. 6 (June): 2060–2067. (Cited on page 49).

Jochen Moll, Christian Kexel, Jens Kathol, Claus-Peter Fritzen, Maria Moix-Bonet, Christian Willberg, Marcel Rennoch, Michael Koerdt, and Axel Herrmann. 2020. Guided waves for damage detection in complex composite structures: the influence of omega stringer and different reference damage size. *Applied sciences* 10 (9): 3068. (Cited on page 10).

- Farid Moradi-Marani, Serge Apedovi Kodjo, Patrice Rivard, and Charles-Philippe Lamarche. 2014. Effect of the temperature on the nonlinear acoustic behavior of reinforced concrete using dynamic acoustoelastic method of time shift. *Journal of Nondestructive Evaluation* 33 (2): 288–298. (Cited on page 11).
- F D Murnaghan. 1937. Finite deformations of an elastic solid. *Amer. J. Math.* 59, no. 2 (April): 235. (Cited on pages 3 sq.).
- Francis Dominic Murnaghan. 1937. Finite deformations of an elastic solid. *American Journal of Mathematics* 59 (2): 235–260. (Cited on page 15).
- Tarun R Naik, V Mohan Malhotra, and John S Popovics. 2003. The ultrasonic pulse velocity method. In *Handbook on Nondestructive Testing of Concrete, Second Edition*, 8–1. CRC Press. (Cited on page 15).
- Ernst Niederleithinger, Xin Wang, Martin Herbrand, and Matthias Müller. 2018. Processing ultrasonic data by coda wave interferometry to monitor load tests of concrete beams. *Sensors* 18 (6): 1971. (Cited on page 13).
- Ernst Niederleithinger, Julia Wolf, Frank Mielentz, Herbert Wiggenhauser, and Stephan Pirskawetz. 2015. Embedded ultrasonic transducers for active and passive concrete monitoring. *Sensors* 15 (5): 9756–9772. (Cited on pages 13, 15).
- Zihua Niu, Alice-Agnes Gabriel, Linus Seelinger, and Heiner Igel. 2024. Modeling and quantifying parameter uncertainty of co-seismic non-classical nonlinearity in rocks. *Journal of Geophysical Research: Solid Earth* 129 (1). (Cited on pages 10, 16, 23, 33).
- Carnot L Nogueira and Kevin L Rens. 2019. Acoustoelastic response of concrete under uniaxial compression. *ACI Mater. J.* 116, no. 3 (May). (Cited on page 5).
- Leonard Obert. 1939. Sonic method of determining the modulus of elasticity of building materials under pressure. In *Proc. ASTM*, 39:987. (Cited on page 4).
- Alan V Oppenheim. 1999. Discrete-time signal processing [in en]. Philadelphia, PA: Pearson Education. (Cited on page 45).
- LA Ostrovsky and Paul A Johnson. 2001. Dynamic nonlinear elasticity in geomaterials. *La Rivista del Nuovo Cimento* 24 (7): 1–46. (Cited on page 22).
- Lotfollah Pahlavan, Fengqiao Zhang, Gerrit Blacquière, Yuguang Yang, and Dick Hordijk. 2018. Interaction of ultrasonic waves with partially-closed cracks in concrete structures [in en]. *Constr. Build. Mater.* 167 (April): 899–906. (Cited on page 45).
- Nimrat Pal Kaur, Jay Kumar Shah, Subhra Majhi, and Abhijit Mukherjee. 2019. Healing and simultaneous ultrasonic monitoring of cracks in concrete [in en]. *Mater. Today Commun.* 18 (March): 87–99. (Cited on page 45).
- Yih-Hsing Pao and Udo Gamer. 1985. Acoustoelastic waves in orthotropic media. *The Journal of the Acoustical Society of America* 77 (3): 806–812. (Cited on pages 3, 10, 67).

C Payan, V Garnier, J Moysan, and PA Johnson. 2009. Determination of third order elastic constants in a complex solid applying coda wave interferometry. *Applied Physics Letters* 94 (1). (Cited on pages 4, 11).

- Cedric Payan, Vincent Garnier, Joseph Moysan, and Paul A Johnson. 2008. Determination of nonlinear elastic constants and stress monitoring in concrete by coda waves analysis. In *Proceedings of Meetings on Acoustics*, vol. 3. 1. AIP Publishing. (Cited on pages 4, 11).
- Thanh-Son Phám and Hrvoje Tkalčić. 2017. On the feasibility and use of teleseismic P wave coda autocorrelation for mapping shallow seismic discontinuities. *Journal of Geophysical Research: Solid Earth* 122 (5): 3776–3791. (Cited on page 56).
- Pioldi, Ferrari, and Rizzi. 2022. A refined FDD algorithm for Operational Modal Analysis of buildings under earthquake loading. of the 26th International Conference on  $\tilde{A}\phi\hat{a}$ ,  $\neg\hat{A}_{i}^{l}$ , (cited on page 55).
- Lei Qin, Hongrui Qiu, Nori Nakata, Sizhuang Deng, Alan Levander, and Yehuda Ben-Zion. 2023. Variable daily autocorrelation functions of high-frequency seismic data on Mars [in en]. *Seismol. Res. Lett.* 94 (2A): 746–758. (Cited on page 56).
- NK Raju. 1970. Small concrete specimens under repeated compressive loads by pulse velocity technique. *Journal of Materials*, (cited on pages 4, 10).
- Narintsoa Ranaivomanana, Stéphane Multon, and Anaclet Turatsinze. 2013. Basic creep of concrete under compression, tension and bending. *Construction and Building Materials* 38:173–180. (Cited on page 48).
- A D Ross. 1958. Creep of concrete under variable stress. J. Am. Concr. Inst. 54 (3). (Cited on page 48).
- Daniel Royer and Tony Valier-Brasier. 2022. Elastic waves in solids, volume 1: Propagation [in en]. London, England: ISTE Ltd / John Wiley & Sons. (Cited on page 54).
- Elias Saqan and Hayder Rasheed. 2011. Simplified nonlinear analysis to compute neutral axis depth in prestressed concrete rectangular beams [in en]. *J. Franklin Inst.* 348, no. 7 (September): 1588–1604. (Cited on page 48).
- M Scalerandi, P P Delsanto, and P A Johnson. 2003. Stress induced conditioning and thermal relaxation in the simulation of quasi-static compression experiments. *J. Phys. D Appl. Phys.* 36 (3): 288–293. (Cited on page 33).
- Dennis P Schurr, Jin-Yeon Kim, Karim G Sabra, and Laurence J Jacobs. 2011. Damage detection in concrete using coda wave interferometry. *NDT E Int.* 44, no. 8 (December): 728–735. (Cited on pages 5, 11).
- C Sens-Schönfelder and U Wegler. 2006. Passive image interferometry and seasonal variations of seismic velocities at Merapi Volcano, Indonesia. *Geophysical Research Letters* 33 (21). (Cited on pages 11, 17).
- Christoph Sens-Schönfelder, Roel Snieder, and Xun Li. 2019. A model for nonlinear elasticity in rocks based on friction of internal interfaces and contact aging. *Geophysical Journal International* 216 (1): 319–331. (Cited on pages 7, 16, 34).
- P Shokouhi, A Zoëga, and H Wiggenhauser. 2010. Nondestructive investigation of stress-induced damage in concrete. *Adv. Civ. Eng.*, (cited on pages 5, 10).

Parisa Shokouhi, Jacques Rivière, Robert A Guyer, and Paul A Johnson. 2017. Slow dynamics of consolidated granular systems: Multi-scale relaxation. *Applied Physics Letters* 111 (25). (Cited on pages 16, 35).

- Parisa Shokouhi, Jacques Rivière, Colton R Lake, Pierre-Yves Le Bas, and T J Ulrich. 2017. Dynamic acousto-elastic testing of concrete with a coda-wave probe: comparison with standard linear and nonlinear ultrasonic techniques [in en]. *Ultrasonics* 81 (November): 59–65. (Cited on pages 7, 11).
- Jonathan Singh, Andrew Curtis, Youqian Zhao, Alexis Cartwright-Taylor, and Ian Main. 2019. Coda wave interferometry for accurate simultaneous monitoring of velocity and acoustic source locations in experimental rock physics. *Journal of Geophysical Research: Solid Earth* 124 (6): 5629–5655. (Cited on page 10).
- Roel Snieder, Christoph Sens-Schönfelder, and Renjie Wu. 2017. The time dependence of rock healing as a universal relaxation process, a tutorial. *Geophysical Journal International* 208 (1): 1–9. (Cited on pages 16, 35 sq., 52).
- PS Song and S Hwang. 2004. Mechanical properties of high-strength steel fiber-reinforced concrete. *Construction and Building Materials* 18 (9): 669–673. (Cited on page 14).
- Simon Christian Stähler, Christoph Sens-Schönfelder, and Ernst Niederleithinger. 2011.

  Monitoring stress changes in a concrete bridge with coda wave interferometry. *The Journal of the Acoustical Society of America* 129 (4): 1945–1952. (Cited on pages 6, 11, 54).
- Wimal Suaris and Viraj Fernando. 1987. Detection of crack growth in concrete from ultrasonic intensity measurements. *Mater. Struct.* 20, no. 3 (May): 214–220. (Cited on pages 4, 10, 45).
- Belay Tefera and Abrham Tarekegn. 2025. Non-destructive testing techniques for condition assessment of concrete structures: A review [in en]. *Am. J. Civ. Eng.* 13, no. 1 (January): 10–31. (Cited on page 2).
- James A Ten Cate and Thomas J Shankland. 1996. Slow dynamics in the nonlinear elastic response of Berea sandstone [in en]. *Geophys. Res. Lett.* 23 (21): 3019–3022. (Cited on page 7).
- James A TenCate. 2011. Slow dynamics of earth materials: An experimental overview [in en]. *Pure Appl. Geophys.* 168, no. 12 (December): 2211–2219. (Cited on pages 29, 48).
- V Tinard, C Fond, and P Fran $\tilde{A}f\hat{A}$ §ois. 2025. Eliminating the effect of couplant on ultrasonic characterisation of solids: Experimental and theoretical investigations [in en]. *NDT E Int.* 154, no. 103385 (September): 103385. (Cited on page 45).
- Nicolas Tremblay, Eric Larose, and Vincent Rossetto. 2010. Probing slow dynamics of consolidated granular multicomposite materials by diffuse acoustic wave spectroscopy. *The Journal of the Acoustical Society of America* 127 (3): 1239–1243. (Cited on page 24).
- Oleksiy O Vakhnenko, Vyacheslav O Vakhnenko, and Thomas J Shankland. 2005. Soft-ratchet modeling of end-point memory in the nonlinear resonant response of sedimentary rocks. *Phys. Rev. B Condens. Matter* 71 (17): 174103. (Cited on page 33).
- Xin Wang, Joyraj Chakraborty, Antoine Bassil, and Ernst Niederleithinger. 2020. Detection of multiple cracks in Four-Point bending tests using the Coda Wave Interferometry method [in en]. *Sensors (Basel)* 20, no. 7 (April): 1986. (Cited on pages 6, 11).

Xin Wang, Joyraj Chakraborty, and Ernst Niederleithinger. 2021. Noise reduction for improvement of ultrasonic monitoring using coda wave interferometry on a real bridge. *Journal of Nondestructive Evaluation* 40 (1): 14. (Cited on page 11).

- Richard L Weaver, Céline Hadziioannou, Eric Larose, and Michel Campillo. 2011. On the precision of noise correlation interferometry. *Geophysical Journal International* 185 (3): 1384–1392. (Cited on pages 19, 30).
- Max Wyss, Michel Speiser, and Stavros Tolis. 2023. Earthquake fatalities and potency [in en]. *Nat. Hazards (Dordr.)* 119, no. 2 (November): 1091–1106. (Cited on page 1).
- Qi Xue, Eric Larose, Ludovic Moreau, Romain Thery, Odile Abraham, and Jean-Marie Henault. 2022. Ultrasonic monitoring of stress and cracks of the 1/3 scale mock-up of nuclear reactor concrete containment structure [in en]. *Struct. Health Monit.* 21, no. 4 (July): 1474–1482. (Cited on pages 6, 11).
- John Y Yoritomo and Richard L Weaver. 2020a. Slow dynamic elastic recovery in unconsolidated metal structures [in en]. *Phys. Rev. E.* 102, nos. 1-1 (July): 012901. (Cited on page 7).
- ———. 2020b. Slow dynamic nonlinearity in unconsolidated glass bead packs [in en]. *Phys. Rev. E.* 101, nos. 1-1 (January): 012901. (Cited on page 7).
- Hanyu Zhan, Hanwan Jiang, Chenxu Zhuang, Jinquan Zhang, and Ruinian Jiang. 2020. Estimation of stresses in concrete by using coda wave interferometry to establish an acoustoelastic modulus database [in en]. *Sensors (Basel)* 20, no. 14 (July): 4031. (Cited on page 5).
- Hongyu Zhang, Binbin Mi, Ya Liu, Chaoqiang Xi, and Kouao Laurent Kouadio. 2021. A pitfall of applying one-bit normalization in passive surface-wave imaging from ultra-short roadside noise [in en]. *J. Appl. Geophy.* 187, no. 104285 (April): 104285. (Cited on page 56).
- Y Zhang, O Abraham, E Larose, T Planes, A Le Duff, B Lascoup, V Tournat, R El Guerjouma, L-M Cottineau, O Durand, Donald O Thompson, and Dale E Chimenti. 2011. Following stress level modification of real size concrete structures with coda wave interferometry (Cwi). AIP. (Cited on page 6).
- Yuxiang Zhang, Odile Abraham, Frédéric Grondin, Ahmed Loukili, Vincent Tournat, Alain Le Duff, Bertrand Lascoup, and Olivier Durand. 2012. Study of stress-induced velocity variation in concrete under direct tensile force and monitoring of the damage level by using thermally-compensated Coda Wave Interferometry [in en]. *Ultrasonics* 52, no. 8 (December): 1038–1045. (Cited on pages 5, 11).
- Yuxiang Zhang, Odile Abraham, E Larose, Thomas Planes, Alain Le Duff, Bertrand Lascoup, Vincent Tournat, Rachid El Guerjouma, L-M Cottineau, and Olivier Durand. 2011. Following stress level modification of real size concrete structures with coda wave interferometry (CWI). In *AIP Conference Proceedings*, 1335:1291–1298. 1. American Institute of Physics. (Cited on page 11).
- Yuxiang Zhang, Eric Larose, Ludovic Moreau, and Grégoire d'Ozouville. 2018.

  Three-dimensional in-situ imaging of cracks in concrete using diffuse ultrasound [in en].

  Struct. Health Monit. 17, no. 2 (March): 279–284. (Cited on page 6).
- Yuxiang Zhang, Thomas Planès, Eric Larose, Anne Obermann, Claude Rospars, and Gautier Moreau. 2016. Diffuse ultrasound monitoring of stress and damage development on a 15-ton concrete beam. *The Journal of the Acoustical Society of America* 139 (4): 1691–1701. (Cited on pages 6, 11).

Bibo Zhong, Jinying Zhu, and George Morcous. 2021. Measuring acoustoelastic coefficients for stress evaluation in concrete. *Construction and Building Materials* 309:125127. (Cited on pages 5 sq., 11, 16).